

coatings

Mechanical Properties and Structural Analysis of Coatings and Engineered Surfaces

Edited by

Mattia Merlin and Annalisa Fortini

Printed Edition of the Special Issue Published in *Coatings*

Mechanical Properties and Structural Analysis of Coatings and Engineered Surfaces

Mechanical Properties and Structural Analysis of Coatings and Engineered Surfaces

Editors

Mattia Merlin

Annalisa Fortini

MDPI • Basel • Beijing • Wuhan • Barcelona • Belgrade • Manchester • Tokyo • Cluj • Tianjin



Editors

Mattia Merlin	Annalisa Fortini
Department of Engineering (DE)	Department of Engineering (DE)
University of Ferrara	University of Ferrara
Ferrara	Ferrara
Italy	Italy

Editorial Office

MDPI
St. Alban-Anlage 66
4052 Basel, Switzerland

This is a reprint of articles from the Special Issue published online in the open access journal *Coatings* (ISSN 2079-6412) (available at: www.mdpi.com/journal/coatings/special_issues/mechanical).

For citation purposes, cite each article independently as indicated on the article page online and as indicated below:

LastName, A.A.; LastName, B.B.; LastName, C.C. Article Title. <i>Journal Name</i> Year , <i>Volume Number</i> , Page Range.
--

ISBN 978-3-0365-1804-6 (Hbk)

ISBN 978-3-0365-1803-9 (PDF)

© 2021 by the authors. Articles in this book are Open Access and distributed under the Creative Commons Attribution (CC BY) license, which allows users to download, copy and build upon published articles, as long as the author and publisher are properly credited, which ensures maximum dissemination and a wider impact of our publications.

The book as a whole is distributed by MDPI under the terms and conditions of the Creative Commons license CC BY-NC-ND.

Contents

Mattia Merlin and Annalisa Fortini Mechanical Properties and Structural Analysis of Coatings and Engineered Surfaces Reprinted from: <i>Coatings</i> 2021 , <i>11</i> , 875, doi:10.3390/coatings11080875	1
Giovanni Straffelini and Matteo Federici HVOF Cermet Coatings to Improve Sliding Wear Resistance in Engineering Systems Reprinted from: <i>Coatings</i> 2020 , <i>10</i> , 886, doi:10.3390/coatings10090886	3
Alessandro Morri, Lorella Ceschini, Carla Martini and Alessandro Bernardi Influence of Plasma Electrolytic Oxidation on Fatigue Behaviour of ZK60A-T5 Magnesium Alloy Reprinted from: <i>Coatings</i> 2020 , <i>10</i> , 1180, doi:10.3390/coatings10121180	15
Donya Ahmadkhaniha, Lucia Lattanzi, Fabio Bonora, Annalisa Fortini, Mattia Merlin and Caterina Zanella The Effect of Co-Deposition of SiC Sub-Micron Particles and Heat Treatment on Wear Behaviour of Ni-P Coatings Reprinted from: <i>Coatings</i> 2021 , <i>11</i> , 180, doi:10.3390/coatings11020180	29
Eduardo Hurtado-Delgado, Lizbeth Huerta-Larumbe, Argelia Miranda-Pérez and Álvaro Aguirre-Sánchez Microcracks Reduction in Laser Hardened Layers of Ductile Iron Reprinted from: <i>Coatings</i> 2021 , <i>11</i> , 368, doi:10.3390/coatings11030368	45
Annalisa Fortini, Alessio Suman, Alessandro Vulpio, Mattia Merlin and Michele Pinelli Microstructural and Erosive Wear Characteristics of a High Chromium Cast Iron Reprinted from: <i>Coatings</i> 2021 , <i>11</i> , 490, doi:10.3390/coatings11050490	61

Mechanical Properties and Structural Analysis of Coatings and Engineered Surfaces

Mattia Merlin *  and Annalisa Fortini * 

Department of Engineering (DE), University of Ferrara, Via Saragat 1, 44122 Ferrara, Italy

* Correspondence: mattia.merlin@unife.it (M.M.); annalisa.fortini@unife.it (A.F.)

1. Introduction and Scope

The performance improvement in engineering components during operation is a challenging issue and surface engineering methods have been attracting considerable interest in both research and industrial fields. Surface characteristics have a pivotal role in enhancing the life of products since they control the mechanical, electrical, thermal, and electronic properties. Nevertheless, the surface and near-surface properties are crucial in failure mechanisms since the loss of performance and failures mostly begin from the surface.

In this framework, this Special Issue includes original research papers and a review that covers the latest development in methods for enhancing the life and functionality of engineering components by tuning the physical, chemical, mechanical, and metallurgical properties of their surfaces. Attention is focused on processing and characterizing methods capable of supporting industrial applications and products to both tackle surface degradation and improve the performance and reliability of components.

2. Contributions

The book collects manuscripts from cutting-edge academic researchers and consists of one review paper regarding the characteristics and mechanical properties of high-velocity oxy-fuel (HVOF) cermet coatings [1] and four research papers focused on the effects of different treatments and coatings on the mechanical and microstructural properties of the investigated material [2–4].

The review by Straffellini and Federici [1] deals with the main characteristics and mechanical properties of HVOF cermet coatings, focusing on the dry sliding behavior of several types of coatings, analyzed at both room and high temperature. Besides, it considers the practical relevance of the proposed topic (i.e., the employment of HVOF coatings for discs in brake applications for the automotive industry, an emerging application that reduces the wear of the braking components, and thus the emission of airborne particulate matter). The review provides a comprehensive synopsis of the recent developments of novel HVOF cermet coatings including Fe-based, Ni-based matrix, and/or submicron-sized carbide and oxide particles.

The effect of plasma electrolytic oxidation (PEO), followed by the deposition of a polymeric layer by the powder coating, on the rotating bending fatigue behavior of the wrought magnesium alloy ZK60A-T5 was studied by Morri et al. [2]. The examined samples, directly extracted from cast-forged wheels to test specimens with the same microstructure of the real component, revealed a reduction in fatigue strength for the PEO-treated specimens. This investigation pointed out that PEO induced a fatigue strength reduction in the range of 14–17% at 10^7 cycles in comparison with the literature data of untreated alloys. Such a reduction is probably related to the intrinsic defectiveness of the PEO and the residual tensile stresses generated during the treatment.

Another relevant contribution was proposed by Ahmadkhaniha et al. [3]. To enhance the hardness and wear resistance of electrodeposited Ni–P and Ni–P/SiC composite coat-



Citation: Merlin, M.; Fortini, A. Mechanical Properties and Structural Analysis of Coatings and Engineered Surfaces. *Coatings* **2021**, *11*, 875. <https://doi.org/10.3390/coatings11080875>

Received: 13 July 2021
Accepted: 20 July 2021
Published: 22 July 2021

Publisher's Note: MDPI stays neutral with regard to jurisdictional claims in published maps and institutional affiliations.



Copyright: © 2021 by the authors. Licensee MDPI, Basel, Switzerland. This article is an open access article distributed under the terms and conditions of the Creative Commons Attribution (CC BY) license (<https://creativecommons.org/licenses/by/4.0/>).

ings, the authors studied the effect of SiC particles in combination with different heat treatment conditions on the wear behavior of these coatings. The results demonstrated that SiC particles significantly influenced the coefficient of friction and the wear rate of the coatings, despite the limited influence in increasing hardness. Besides, after heat treatment, the coefficient of friction trends reported a difference in some relevance between the Ni–P and Ni–P/SiC composite coatings only for the treatment performed at the lowest temperature (i.e., 300 °C for 2 h). This study gives a contribution to the role of SiC addition and heat treatment on the wear properties of Ni–P coatings, highlighting the optimum condition that minimizes the wear rate.

The paper by Hurtado-Delgado et al. [4] deals with the analysis of ductile irons, with and without austempering heat treatment, and surface hardened by Nd:YAG laser. The aim of the study was to show that the austempered heat treatment before laser hardening is effective in reducing the number of surface microcracks in a wide range of heat inputs. The results indicate that surface hardening via laser is a suitable method for improving wear resistance in critical areas without compromising the core ductility of ductile iron components. The surface ductility is enhanced when the cast iron is austempered before the laser hardening by the reduction of surface microcracks. Austempered ductile irons are less prone to crack formation than ductile irons because they contain less cementite and more martensite and because ausferrite has a higher heat conductivity than pearlite.

Finally, the paper by Fortini et al. [5] deals with hardfacing, a widely used surface coating technique to enhance the corrosive, abrasive, and heat resistance properties of a metal workpiece's surface, especially for heavy-duty applications (e.g., minerals and mining industries, cement plants, paper and pulp industry, thermal power plants, iron and steel industries, etc.). Specifically, the work investigated the microstructural and erosive wear characteristics of a hypereutectic high-chromium cast iron (HCCI) by considering the erosion resistance, resulting from the impact of micro-sized particles, of both the as-received and heat-treated conditions. The experimental findings showed the efficacy of the adopted destabilization treatment in improving the erosion resistance of the investigated HCCI alloy, which is strongly affected by the matrix/carbides hardness difference.

Author Contributions: Writing—original draft preparation, A.F.; writing—review and editing, M.M. Both authors have read and agreed to the published version of the manuscript.

Funding: This research received no external funding.

Institutional Review Board Statement: Not applicable.

Informed Consent Statement: Not applicable.

Acknowledgments: As Guest Editors, we would like to especially thank Raynor Zhou, Managing Editor, for his valuable support in the publication process. We are grateful to all the contributing authors and reviewers: without their excellent work, it would not have been possible to accomplish this Special Issue.

Conflicts of Interest: The authors declare no conflict of interest.

References

1. Straffelini, G.; Federici, M. HVOF cermet coatings to improve sliding wear resistance in engineering systems. *Coatings* **2020**, *10*, 886. [[CrossRef](#)]
2. Morri, A.; Ceschini, L.; Martini, C.; Bernardi, A. Influence of Plasma electrolytic oxidation on fatigue behaviour of ZK60A-T5 magnesium alloy. *Coatings* **2020**, *10*, 1180. [[CrossRef](#)]
3. Ahmadkhaniha, D.; Lattanzi, L.; Bonora, F.; Fortini, A.; Merlin, M.; Zanella, C. The effect of Co-Deposition of SiC sub-micron particles and heat treatment on wear behaviour of Ni–P coatings. *Coatings* **2021**, *11*, 180. [[CrossRef](#)]
4. Hurtado-Delgado, E.; Huerta-Larumbe, L.; Miranda-Pérez, A.; Aguirre-Sánchez, Á. Microcracks reduction in laser hardened layers of ductile iron. *Coatings* **2021**, *11*, 368. [[CrossRef](#)]
5. Fortini, A.; Suman, A.; Vulpio, A.; Merlin, M.; Pinelli, M. Microstructural and erosive wear characteristics of a high chromium cast iron. *Coatings* **2021**, *11*, 490. [[CrossRef](#)]

Review

HVOF Cermet Coatings to Improve Sliding Wear Resistance in Engineering Systems

Giovanni Straffelini *  and Matteo Federici

Dept. Industrial Engineering, University of Trento, 38122 Trento, Italy; matteo_federici@brembo.it

* Correspondence: giovanni.straffelini@unitn.it

Received: 1 July 2020; Accepted: 9 September 2020; Published: 14 September 2020



Abstract: High-Velocity Oxy-Fuel (HVOF) cermet coatings are widely employed in sliding conditions, due to their optimized microstructure, composed of a carbide phase embedded into a ductile metal matrix. In the present short review, the characteristics and mechanical properties of HVOF cermet coatings are considered, and the dry sliding behaviour of the main types of coatings is analysed at room and high temperature. The role of microstructural parameters, including defects, surface roughness and the nature of the counterface is discussed. The review also considers a specific application, namely HVOF coatings for discs in brake applications. This application is gaining in importance, since it reduces the wear of the braking components and thus the emission of airborne particulate matter.

Keywords: HVOF coatings; sliding wear; brake systems

1. Introduction

High-Velocity Oxy-Fuel (HVOF) cermet coatings are widely employed in tribological applications featuring sliding conditions, such as sliding bearings, valves and forging dies, and as a substitute for hard chrome plating, and emerging industrial needs make these kind of coatings very attractive for new applications, in particular in the automotive industry [1–3]. WC-Co and Cr₃C₂-NiCr cermet coatings are typically used on different materials, such as steels or ceramic materials [4–8]. The particularly high wear resistance of these coatings is due to their composite microstructure, composed of a carbide phase embedded into a ductile metal matrix. The carbides act as the reinforcing component while the metal binder increases the coating toughness and binds the carbide particles together [2].

The HVOF process involves a supersonic jet flame produced by the combustion of a mixture of oxygen and fuel. This technique has been developed to decrease the decarburisation and oxidation that occur during conventional thermal spraying processes. Moreover, the reduced presence of oxides and pores inside the microstructure improves the properties of the sprayed coatings [3,4]. The preparation of the substrate is fundamental to improve its adhesion with the coating. Typically, the surfaces of the components to be coated are first degreased and then sandblasted to increase their surface roughness and promote the mechanical interlocking between the substrate and the coating. In some cases, to improve the adhesion, intermediate bond layers made of Mo or other alloys are deposited.

Depending on the HVOF gun used and the coating to be deposited, several types of fuels can be employed. The most common are hydrogen, propane, kerosene (aviation grade) and liquefied petroleum gas (LPG). Since liquid fuels have several advantages over gaseous fuels, the latest technology is mainly based on the use of liquid fuels. The sprayed particles reach speeds in excess of 500 m/s and temperatures of up to 2300 K [3]. In general, an increase in the oxygen flow rate leads to an increase in both the particle temperature and speed. However, if the oxygen flow rate is too high, a decrease in particle temperature is observed, due to the oxygen excess leading to a combustion with a lower efficiency. Increasing the kerosene flow rate also leads to an increase in both particle

temperature and speed. Additionally, in this case, at a critical flow rate, the particle temperature starts decreasing, because of the non-stoichiometric combustion and the cooling produced by the excess in kerosene [6]. Other relevant process parameters are the powder feed rate and the spraying distance. At a low powder feed rate (typically below 30 g/min) the particles overheat, inducing a loss in hardness and an increase in the residual porosity of the sprayed coating. At high powder feed rates (typically in excess of 60 g/min), the flight time of the particles inside the flame is too low, leading to an improper melting of the powder which, again, reduces the hardness and increases the residual porosity of the sprayed coating [7,9]. The spraying distance influences both the temperature and the speed of the sprayed particles; an increase in the spraying distance leads to a decrease in the particle temperature and speed, due to the cooling effect and to the drag force exerted on the stream of the semi-molten particles by the surrounding air. However, a reduction in the spraying distance below 150–200 mm produces an increase in the porosity and a loss in the hardness due to the kinetic energy variations of the in-flight particles [7,10]. The optimal spraying distance is found to be in the range 200–350 mm [7,9]. A summary of the most common spraying parameters for HVOF cermet coatings is given in Table 1. It is clear that the process parameters have to be properly optimised to obtain the best hardness and microstructural properties and, in the end, the best sliding performances. After deposition, the coatings are characterised by a quite high roughness (typical R_a values between 2–6 μm). For most applications, surface roughness is reduced by polishing to $R_a = 0.1 \mu\text{m}$ or less.

Table 1. Summary of the HVOF process parameters [1,6,7,9,11,12].

Process Parameter	Value
Oxygen flow rate	(1.8–60) m^3/h
Hydrogen flow rate	(3.6–40) m^3/h
Kerosene flow rate	(20–30) L/h
Carrier gas	Nitrogen
Spraying distance	(200–350) mm
Powder feed rate	(25–65) g/min

The process parameters summarised in Table 1 mainly refer to the deposition of conventional powders, with a particle size of 5–60 μm . For the deposition of nano-sized powders, the process parameters should be modified to consider the higher specific surface area, which could cause a more rapid decarburisation and the formation of higher amounts of parasitic phases [2].

In the present short review, the main characteristics and mechanical properties of HVOF cermet coatings are firstly considered. Then, the dry sliding behaviour of the main types of coatings is analysed at room and high temperature, with special emphasis on the role of microstructural parameters, including defects and surface roughness. To our knowledge, no specific reviews on the (dry) sliding wear of these coatings are present in the literature. In addition, the available literature data are obtained using different testing conditions, making very difficult to have a reliable comparison. Finally, the review considers an emerging application, namely HVOF coatings for discs in brake applications for the automotive industry. This application is gaining in importance, since it reduces the wear of the braking components and thus the emission of airborne particulate matter. The example aims to highlight the versatility of this type of coatings, which is able to excel in ever new applications, meeting the most demanding engineering requirements.

2. Microstructure of WC-Co, WC-CoCr and Cr_3C_2 -NiCr HVOF Coatings

The microstructure of cermet coatings is strictly related to the deposition parameters. In particular, the maximum temperature and the time spent by the particles at that temperature strongly affect the final microstructure. This is because, from a thermodynamic viewpoint, in the temperature range between 2000 and 3000 K, the W_2C phase is more stable than the WC phase. Therefore, increasing particle temperature leads to a decarburisation of the WC phase with the consequent precipitation

of W_2C , which is harder and more brittle than WC (3000 kg/mm² with respect to 2400 kg/mm²). Lekatou et al. [2] described the decarburisation mechanism as follows:

- During the spraying process, the periphery of the flying carbide particles reaches high temperature and dissolves into the Co matrix;
- The quenching of the sprayed particles, due to the impact with the cold substrate, produces a rapid decrease in the solubility of W and C in Co, leading to the precipitation of a W_2C layer around a WC core.

Skandan et al. [13] proposed the following decarburisation reactions to describe the evolution of the carbides during spraying: $2WC \rightarrow W_2C + C$; $W_2C \rightarrow 2W + C$; $2C + O_2 \rightarrow 2CO$. The decomposition of W_2C into W and C produces an additional shell of W around the WC particles. Other parasitic phases, whose formation should be avoided with the correct spray parameters, are the embrittling Co-containing-phases, such as Co_3W_3C , CoW_6C and Co_6W_4C (also-called η -phases) [14].

Regarding Cr-carbides, above 2500 K the most stable phase is $Cr_{23}C_6$ followed by Cr_7C_3 and Cr_3C_2 . In HVOF coatings containing Cr_3C_2 , typically used for their excellent high-temperature tribological performance, different decarburisation mechanisms have been proposed: Cr_7C_3 forms following the decarburisation of Cr_3C_2 while $Cr_{23}C_6$ precipitates during the HVOF process [1]. Zimmermann and Kreye [15] stated that the X-ray diffraction peaks of Cr_7C_3 and $Cr_{23}C_6$ overlap with those of NiCr and Cr_3C_2 , making their detection very difficult.

In general, HVOF cermet coatings display a splat-like microstructure due to the impacts of partially melted droplets followed by their rapid solidification. Some residual porosity is found in the interlamellar regions (the typical residual porosities of HVOF coatings are below 2–3%). This splat-like microstructure leads to the anisotropic mechanical properties of sprayed coatings. A further source of anisotropy is related to the WC particles that remain in a solid state during spraying. They may retain their original angular morphology in the microstructure or have a rounded appearance. The rounded morphology is a result of a WC dissolution into the matrix with the formation of an external irregular-shaped W_2C phase and, possibly, a nanocrystalline/amorphous matrix phase [11].

3. Mechanical Properties of HVOF Hard Coatings

The mechanical properties of HVOF cermet coatings depend on various parameters, including process parameters (Table 1), feedstock powder chemistry and particle size, initial phase content and carbide grain size, which influence the final microstructure of the coatings [1].

The process parameters, in particular, determine the particle temperature during spraying, which has been shown to be strongly related to the coating hardness [6]. In general, coating hardness increases with particle temperature. It is suggested that high process temperatures cause decarburisation and the dissolution of W, Cr and C into the metal matrix (CoCr or NiCr). As a consequence, the coating hardness is increased since the reduction in the volume fraction of WC carbides is more than compensated by the hardness increase of the matrix and, possibly, by a higher content of the harder W_2C carbides.

Usmani et al. [16] investigated the properties of WC-17Co coatings obtained with starting powders containing three different carbide size distributions, with median size of 1.2 μm (fine), 3.8 μm (medium) and 7.9 μm (coarse). The coatings contained a significant amount of W_2C and W. Selected microstructural and mechanical properties are listed in Table 2. The microhardness values were found to be slightly increased by decreasing the carbide size, because of the increased mean free path and the decreased W_2C content of the coarser particles. The coating fracture toughness follows the opposite trend, and this was attributed by the authors to the higher W_2C content of the finer carbide particles. In addition, the fracture toughness is lower perpendicularly to the spraying direction, because of the rather low interfacial bonding between the coating splat interfaces.

Table 2. Microstructural and mechanical properties of the HVOF WC-Co coatings investigated by Usmani et al. [16].

	Fine	Medium	Coarse
Median carbide size, μm	1.2	3.8	7.9
Mean free path, μm	0.42	1.01	1.47
W_2C , wt. %	68	48	48
Microhardness, kg/mm^2 (obtained from Knoop tests)	1274	1244	1233
Mean fracture toughness, $\text{MPa m}^{1/2}$	4.4	5.7	6.1

La Vecchia et al. [17] investigated the properties of three different HVOF coatings: WC-12Co, WC-10Co4Cr and Cr_3C_2 -25NiCr. The obtained microhardness values were 1260, 1255 and 1060 kg/mm^2 , respectively. The fact that the Cr_3C_2 -based coating had the lowest hardness was attributed to the higher metallic binder content and, most of all, to the lower hardness of Cr carbide (1400 kg/mm^2).

The prediction and interpretation of the hardness and fracture toughness of HVOF cermet coatings are not always straightforward, because of the large number of microstructural parameters that may play a role. Nahvi et al. [11] investigated different WC-based coatings, measuring their microhardness, porosity and fracture toughness. The investigated cermets were WC-Co (abbreviated to WC-C), WC-FeCrAl (WC-F) and WC-NiMoCrFeCo (WC-N). Table 3 lists the microstructural and mechanical properties. The total volume fraction of carbides in WC-F and WC-N was almost the same, but WC-N displayed a much lower microhardness. The authors attributed this result to the higher W_2C content ($\text{W}_2\text{C}/\text{WC}$ ratio equal to 40.42). Even though W_2C has a higher hardness than WC, the W_2C phase surrounding the WC grains decreases the cohesion of the grains with the matrix, deteriorating both the hardness and the fracture toughness. The WC-C coating, which had the lowest fraction of carbides, showed the highest fracture toughness value and an intermediate value of hardness.

Table 3. Microstructural and mechanical properties of the HVOF coatings investigated by Nahvi et al. [11].

Designation	Carbide Phase [vol. %]	($\text{W}_2\text{C}/\text{WC}$) Ratio	Porosity [vol. %]	Microhardness [HV0.3]	Mean K_{IC} [$\text{MPa}\sqrt{\text{m}}$]
WC-C	55	9.14	1.8	1305 \pm 71	5.9 \pm 0.13
WC-F	58	12.48	5.1	1498 \pm 82	3.1 \pm 0.23
WC-N	59	40.42	2.2	1254 \pm 38	2.8 \pm 0.27

4. Room Temperature Sliding Wear Behaviour of HVOF Coatings

In the paper cited above, La Vecchia et al. [17] investigated the dry sliding behaviour of three different HVOF coatings: WC-12Co; WC-10Co4Cr; Cr_3C_2 -25NiCr. All samples were ground to a surface roughness of $R_a = 0.1 \mu\text{m}$ and the tests were performed using a block-on-ring test. Both blocks and rings were coated. The results are shown in Table 4, where the experimental specific wear rates (given by the ratio of the wear volume to the applied load and sliding distance, and indicated hereafter by K_a) are reported as a function of sliding speed. The WC-12Co coating shows mild wear (with a specific wear coefficient, K_a , lower than $10^{-15} \text{ m}^2/\text{N}$), which is quite similar to that typically displayed by as-sintered WC-Co hard metals [8]. The second coating, however, displays a much larger K_a (at 0.2 m/s) even though its hardness is similar to that of the first coating. The different behaviour was attributed to the presence of the η -phase (pre-existing in the starting powder), which strongly embrittled the coating, promoting the formation and removal of wear fragments. The third coating shows a K_a similar to that of the second. This last coating does not contain the η -phase, but its hardness is lower than that of the first coating.

Table 4. Specific wear rate in m^2/N vs. sliding speed for three HVOF coatings dry sliding against a counterface of the same type in a block-on-ring configuration ([17]).

Material	0.2 m/s	0.6 m/s
WC-12Co	$4.8 \cdot 10^{-16}$	$1 \cdot 10^{-16}$
WC-10Co4Cr	$2 \cdot 10^{-14}$	$5 \cdot 10^{-15}$
Cr_3C_2 -25NiCr	$1.9 \cdot 10^{-14}$	$1.3 \cdot 10^{-14}$

Sudaprasert et al. [18], investigated the sliding wear behaviour of two WC-12Co coatings obtained using kerosene (liquid fuel) or hydrogen (gas fuel), with a hardness of 1230 and 1280 kg/mm^2 , respectively. The tests were conducted in a ball-on-disc configuration, using a ceramic (Al_2O_3) ball as a counterface. The obtained K_a -values were approximately $10^{-15} \text{ m}^2/\text{N}$ and $2 \cdot 10^{-16} \text{ m}^2/\text{N}$, in agreement with the results of La Vecchia et al. [17].

The specific wear coefficient, K_a , is expected to be directly proportional to the coating hardness. As seen, however, microstructural defects, such as the presence of embrittling phases, residual pores and insufficient bonding between the lamellae, may exert a very important role and render the hardness-wear relationship unreliable. A further complication to this is given by the roughness of the coatings and the counterparts. As an example, Picas et al. [19] investigated the sliding behaviour of different Cr_3C_2 -CoNiCrAlY coatings with a hardness of between approximately 1130 and 1290 kg/mm^2 . Pin-on-disc tests were carried out using WC-6Co spherical pins sliding against coated discs. The disc wear coefficients were found to vary between $1.7 \cdot 10^{-14} \text{ m}^2/\text{N}$ and $8 \cdot 10^{-15} \text{ m}^2/\text{N}$. The K_a -values were found to decrease as the coating hardness increased. Furthermore, they were higher than the values previously reported for coatings with similar hardness values. Recently, Bolelli et al. [20] studied the sliding wear of WC-CoCr and WC-(W,Cr)₂C-Ni coatings with a roughness of 0.02 μm . A ball-on-disc apparatus was used, with a ball made of alumina. Some of the microstructural and mechanical properties, including the specific wear coefficients, are listed in Table 5. In this case, the K_a -values are proportional to the coating microhardness, but they are from one to two orders of magnitude lower than the values previously reported.

Table 5. Microstructural and mechanical properties of the HVOF coatings investigated by Bolelli et al. [20].

Material	Microhardness [kg/mm^2]	Mean K_{IC} [$\text{MPa}\sqrt{\text{m}}$]	Friction Coefficient	K_a , [m^2/N]
WC-CoCr	1131	5.06	0.44	app. $6 \cdot 10^{-17}$
WC-(W, Cr) ₂ C-Ni	1090	3.66	0.63	app. 10^{-16}

The sliding tests discussed so far were carried out using ceramic counterfaces. However, in different applications, metal alloys, and in particular steel, are used as counterparts. Ishikawa et al. [3] studied the sliding wear behaviour of WC-20% Cr_3C_2 -7%Ni by means of a pin-on-disc apparatus. The discs were coated, and their surface roughness was decreased by polishing to 0.01–0.02 μm . Iron pins (with a hardness of 138 HV) were used as counterparts. Different mixtures of oxygen and fuel were used for the spray process. The sprayed coatings had quite high microhardness values, approximately between 1200 and 1650 kg/mm^2 . The obtained K_a -values are typical of the mild wear regime for both pins and discs. In particular, the wear rate of the coated disc with the highest hardness was not reported because its particularly low weight loss did not allow any detectable weight change before and after wear testing. The recorded friction coefficients were quite high, in the range 0.85–0.91. Quite interestingly, the K_a -values of the iron pins were also low, except one case. The authors consider this result to be due to the attainment, during sliding, of a tribo-oxidative wear, with the formation of protective oxide scales. Similar results were obtained by Sidhu et al. [4]. The authors investigated the wear performance of WC-Co and Cr_3C_2 -NiCr HVOF coated pins sliding against a hardened

steel (hardness of 62–65 HRC) disc. The roughness of the coatings was reduced to $1.00 \pm 0.32 \mu\text{m}$. The recorded friction coefficient was approximately 0.5 for the WC-Co coating, and 0.78 for the other. The recorded specific wear coefficients were quite low, below $10^{-15} \text{ m}^2/\text{N}$, and they were found to increase during sliding, although no steady state was reached before the end of the tests.

5. High Temperature Wear Behaviour of HVOF Coatings

HVOF cermet coatings are particularly suitable for high-temperature applications, since they are able to retain their hardness up to 600 °C or more. In these applications, ceramic materials are always used as counterparts. Valentinelli et al. [21] carried out pin-on-disc sliding tests at different temperatures, using HVOF WC-17Co coated discs (hardness of 1150 kg/mm²) and alumina balls (hardness equal to 1600 kg/mm²). At room temperature, the K_a -value is quite high (approximately $4 \cdot 10^{-14} \text{ m}^2/\text{N}$), most probably because of abrasive interactions during the sliding. The specific wear rate reaches a minimum at a temperature of about 400 °C (K_a approximately $7 \cdot 10^{-15} \text{ m}^2/\text{N}$). In fact, wear was by tribo-oxidation, and as the temperature was increased, the oxide layer was able to better protect the coating from wear. However, if the testing temperature exceeded 400 °C, the oxidation rate became too high and, at the same time, the hardness of the coating decreased. As a result, the specific wear rate increased.

Zhang et al. [22] investigated the high temperature sliding wear behaviour of WC-10Co-4Cr and Cr₃C₂-25%-NiCr coatings by means of a ball-on-disc apparatus. The tests were performed at 500 °C and 600 °C in a nitrogen atmosphere. The ball material was Si₃N₄. Before the tests, the coated discs were polished to reach a surface roughness lower than 0.35 μm. The recorded average steady-state friction coefficients are listed in Table 6. As far as the wear behaviour is concerned, for the WC-10Co4Cr coating the measured wear coefficients were $9.6 \cdot 10^{-17} \text{ m}^2/\text{N}$ at 500 °C and $4.2 \cdot 10^{-17} \text{ m}^2/\text{N}$ at 600 °C. For the Cr₃C₂-25NiCr coatings, the authors were not able to measure the wear track, demonstrating the well-known excellent high temperature wear resistance of this kind of coating. The K_a -values are extremely low, but it is not clear if the absence of oxygen in the testing atmosphere played a particular role in this.

Table 6. Friction coefficient of the coatings at the testing temperature [22].

Coating	500 °C	600 °C
WC-10Co-4Cr	0.59	0.44
Cr ₃ C ₂ -25NiCr	0.87	0.70

In the above-cited investigation, Bolelli et al. [20] studied the sliding wear behaviour (in air) of WC-CoCr and WC-(W,Cr)₂C-Ni coatings at different temperatures: room temperature, 400 °C, 600 °C and 750 °C. For temperatures up to 600 °C, the recorded specific wear coefficients were below $1 \cdot 10^{-16} \text{ m}^2/\text{N}$ for the WC-CoCr coating, and below $4 \cdot 10^{-15} \text{ m}^2/\text{N}$ for the WC-(W,Cr)₂C-Ni coating, in substantial agreement with the data reported by Zhang et al. [22]. At 750 °C, the specific wear coefficient of the WC-(W,Cr)₂C-Ni coating increased to $10^{-14} \text{ m}^2/\text{N}$, and became very severe for the WC-CoCr coating (in excess of $10^{-13} \text{ m}^2/\text{N}$). This confirms that at room and low ambient temperatures, the WC-CoCr coating performs better than cermet coatings based on Cr carbides. However, at high temperatures, the opposite trend is observed. At room temperature, the observed wear mechanism was the abrasion exerted by the alumina ball asperities, whereas at 400 °C and 600 °C, the thermal softening of the metal matrix causes a transfer of oxidised material onto the alumina ball, leading to a mild wear regime. At 750 °C, the WC-CoCr underwent severe oxidation of the matrix, which greatly reduced the wear resistance. On the other hand, at 750 °C the WC-(W,Cr)₂C-Ni was soon covered by a uniform and compact layer of NiWO₄ + CrWO₄, which protected the surface from severe wear [20].

6. Recently Proposed HVOF Coatings

Yuan et al. [23] investigated the possibility of improving the hardness and the sliding wear behaviour of WC-Co coatings with the addition of submicron-sized WC particles. A commercial WC-12Co powder with a particle size of $45 \pm 15 \mu\text{m}$ was blended with the submicron-sized WC powder (particle size about 300 nm) by ball milling. The microhardness of the coatings was found to increase from approximately 1150 HV for the traditional WC-12Co coating, to approximately 1400 HV for the coating with 5% of submicron particles. Sliding tests were carried out at room temperature and using Si_2N_4 balls as a counterpart. The experimental K_a -values were found to decrease from $6 \cdot 10^{-16} \text{ m}^2/\text{N}$ to $5.2 \cdot 10^{-16} \text{ m}^2/\text{N}$. This decrease was attributed to the submicron-sized particles embedded in the splat interfaces, which hinder the propagation of the wear cracks.

In recent years, the high fluctuation in the price of Ni and Co and the possible health issues caused by airborne wear fragments containing WC, Co, Cr, and Ni have become the driving force for replacing the traditional cermet coatings with less expensive Fe-based alloys. Milanti et al. [24] investigated the properties and the tribological behaviour of HVOF-sprayed Fe-Ni-Cr-B-C and Fe-Ni-Cr-Mo-B-C coatings. Ni was added to promote the formation of an austenitic matrix, with a better corrosion resistance than the ferritic matrix; Cr was added to promote the formation of fine and dispersed carbides; B was mainly added to favour the formation of a nanocrystalline/amorphous microstructure; Mo was added to promote the formation during sliding of beneficial MoO_3 and NiMoO_4 which are expected to act as solid lubricants, improving the sliding wear behaviour of the coating [25–27]. These innovative Fe-based coatings were deposited by HVOF on a low carbon steel substrate. The hardness of the coatings was approximately between 600 and 800 HV0.3, and, therefore, slightly lower than the typical hardness values of HVOF cermet coatings. The sliding behaviour of these Fe-based coatings was tested with a ball-on-disc apparatus, using an alumina ball. The wear rates of discs and counterparts are reported in Table 7 (the results relating to a conventional WC-CoCr coating with a microhardness of approximately 1300 HV are also included as a comparison).

Table 7. Wear rates after ball-on-disc tests [24].

Coating	Disc Wear Rate [m^2/N]	Alumina Ball Wear Rate [m^2/N]
Fe-Ni-Cr-B-C	$3.45 \cdot 10^{-15}$	$0.101 \cdot 10^{-15}$
Fe-Ni-Cr-Mo-B-C	$3.25 \cdot 10^{-15}$	$0.095 \cdot 10^{-15}$
WC-CoCr	$0.06 \cdot 10^{-15}$	$1.151 \cdot 10^{-15}$

The data in Table 7 clearly show that the novel Fe-based coatings have less wear resistance than the conventional WC-CoCr coating, and this is clearly due to their lower hardness. The K_a -values are approximately two orders of magnitude higher. However, it is also seen that the novel Fe-base coatings induce a lower wear on the alumina ball counterfaces (approximately one order of magnitude lower).

Terajima et al. [28] attempted to improve the wear resistance of amorphous Fe-based coatings (FeCrMoCB) by adding WC-12Co particles to the feedstock. Three compositions were investigated, containing 2 wt.%, 4 wt.% and 8 wt.% of WC-Co reinforcing particles. As a comparison, a coating without WC-Co particles was tested. It was noted that the Fe-based coating contained greater porosity than the coating reinforced with WC-Co particles. In fact, the added carbides were found to fill the cavities at the splat interfaces. As a consequence, the increasing content of WC-Co fraction improved the microhardness of the coatings from approximately 700 HV to approximately 900 HV. The sliding behaviour of the coatings was investigated by means of a reciprocating tribometer equipped with an alumina ball. Increasing the content of WC-Co particles resulted in a decrease in friction coefficient from 0.8 to approximately 0.6, and a reduction in K_a from $8 \cdot 10^{-14}$ to $1.5 \cdot 10^{-14} \text{ m}^2/\text{N}$. However, these K_a -values are still quite high, due to the relative low hardness of the coatings and the abrasive interaction exerted by WC debris peeled from the coatings.

More recently, Bolelli et al. [29] also investigated the possibility of reinforcing Fe-based coatings with WC particles. The results show that the K_a -values of the newly developed Fe-based coatings were comparable to those of the traditional WC-CoCr coatings, and lower than $10^{-17} \text{ m}^2/\text{N}$, i.e., extremely low. Moreover, the same authors tested different types of Fe-based coatings [30,31] detecting specific wear coefficients in the order of $10^{-15} \text{ m}^2/\text{N}$.

To summarise, the specific wear coefficients taken from references [3,4,6,13,14,18–20,28–31] are compared in Figure 1 with an indication of the counterface used during the tribological dry sliding tests. It is seen that K_a is quite low (below $10^{-15} \text{ m}^2/\text{N}$) when hardness is typically in excess of 1200 HV. However, the counterface, the coating quality and surface roughness play a paramount role, and this must be considered in designing.

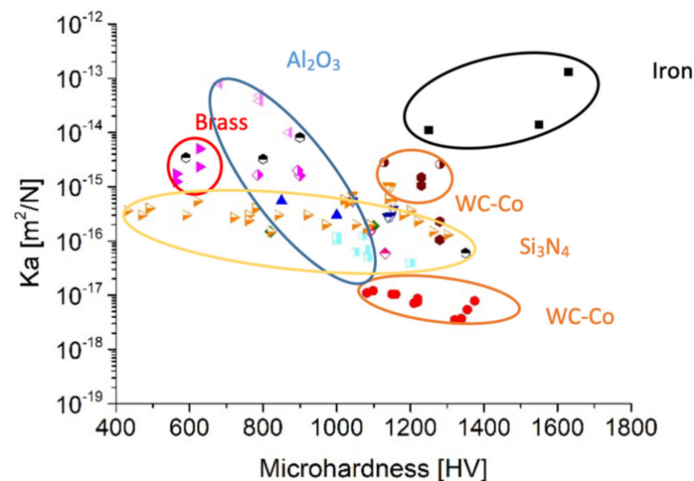


Figure 1. Specific wear coefficients taken from the literature with the indication of the counterfaces used during the tribological tests.

7. HVOF Cermet Coatings for Brake Discs

HVOF cermet coatings are quite promising in brake systems that are made of a friction material pad sliding against a rotating disc [32–34]. In fact, disc wear contributes significantly to system wear and also to the emission of wear particles into the environment [35]. Since the release into the environment of wear particles is strictly related to the wear of the components in sliding contact, by increasing the wear resistance of the discs a reduction in the emissions is expected.

Federici et al. [36] studied the influence of the initial surface roughness and skewness of HVOF WC-10Co4Cr coated discs sliding against a commercial low-metallic friction material. The best compromise between the frictional and wear performances and the industrial feasibility of the polishing process was attained at an average surface roughness of approximately $1 \mu\text{m}$. As surface roughness is decreased, the pin wear decreases only slightly whereas the friction coefficient increases considerably. The tribological characterisation was also extended to their running-in behaviour [37] showing the importance of the polishing process.

Federici et al. [32] also investigated the dry sliding behaviour of WC-CoCr and Cr_3C_2 -NiCr coated discs against a commercial friction material, at both room temperature and $300 \text{ }^\circ\text{C}$. The steady-state friction coefficients at room temperature were quite high, approximately 0.7 and 0.6 for the WC-CoCr and Cr_3C_2 -NiCr coated discs, respectively, but they were attained after quite a long running-in stage, necessary to form a proper friction layer. When sliding against an uncoated cast iron disc, the running-in is much shorter. In fact, the wear of the disc produces fragments that are oxidised and compacted on the friction material, producing a proper friction layer. This has to be properly taken into account in evaluating the brake performance of the tribological system. At $300 \text{ }^\circ\text{C}$, no running-in was observed and the friction coefficient was only slightly reduced. The specific wear coefficients of the coated discs were negligible in all cases.

Wahlström et al. [38] investigated the emission of airborne particles due to the wear of the materials in brake systems with HVOF cermet coated discs. The results were quite promising, showing that this kind of coating can effectively contribute to the reduction of particulate matter emissions. Menapace et al. [39] extended the study, investigating the chemical and phase composition of the airborne fraction of wear debris collected during dyno-bench tests with WC-CoCr coated discs. One of the main results of the investigation was the detection of some critical components transferred from the coating to the airborne fraction of wear debris, including WC and Co. Since some species of this element are considered as hazardous for the human body [40], they should be removed from coatings used for braking applications. In this respect, the novel Fe-based coatings could be promising, and merit further investigation in the future.

8. Conclusions and Future Research Directions

- The dry sliding wear resistance of HVOF cermet coatings is quite high, in particular if their microhardness is in excess of 1200 HV (and no embrittling phases are present).
- Wear rate may increase when using metal (such as steel) counterfaces.
- High wear resistance is also maintained at high temperature (up to at least 400 °C).
- HVOF cermet coatings are very effective in reducing brake system wear and also in reducing airborne particulate emissions.
- Surface roughness has to be optimised to obtain an adequate friction coefficient (proper formation of the friction layer) and low wear.
- However, some W and Co were found in collected airborne particles: Co-free coatings need to be developed and optimised for braking applications

To cope with the requirements of new applications, the development of innovative coatings is then often required. In this regard, the recent developments of novel HVOF cermet coatings, with Fe-based or Ni-based matrix and/or submicron sized carbide or oxide particles, can be seen from this perspective. Further research is still required to improve the microstructural characteristics and the mechanical properties of the novel coatings, so that they can better resist damaging mechanisms faced in real dry sliding conditions.

Funding: This research received no external funding.

Conflicts of Interest: The authors declare no conflict of interest.

References

1. Akhtari Zavareh, M.; Sarhan, A.A.D.M.; Razak, B.B.; Basirun, W.J. The tribological and electrochemical behavior of HVOF-sprayed Cr₃C₂-NiCr ceramic coating on carbon steel. *Ceram. Int.* **2015**, *41*, 5387–5396. [[CrossRef](#)]
2. Lekatou, A.; Sioulas, D.; Karantzalis, A.E.; Grimanelis, D. A comparative study on the microstructure and surface property evaluation of coatings produced from nanostructured and conventional WC-Co powders HVOF-sprayed on Al7075. *Surf. Coat. Technol.* **2015**, *276*, 539–556. [[CrossRef](#)]
3. Ishikawa, Y.; Kuroda, S.; Kawakita, J.; Sakamoto, Y.; Takaya, M. Sliding wear properties of HVOF sprayed WC-20%Cr₃C₂-7%Ni cermet coatings. *Surf. Coat. Technol.* **2007**, *201*, 4718–4727. [[CrossRef](#)]
4. Sidhu, H.S.; Sidhu, B.S.; Prakash, S. Wear characteristics of Cr₃C₂-NiCr and WC-Co coatings deposited by LPG fueled HVOF. *Tribol. Int.* **2010**, *43*, 887–890. [[CrossRef](#)]
5. Pan, J.; Hu, S.; Yang, L.; Ding, K.; Ma, B. Numerical analysis of flame and particle behavior in an HVOF thermal spray process. *Mater. Des.* **2016**, *96*, 370–376. [[CrossRef](#)]
6. Picas, J.A.; Punset, M.; Baile, M.T.; Martín, E.; Forn, A. Effect of oxygen/fuel ratio on the in-flight particle parameters and properties of HVOF WC-CoCr coatings. *Surf. Coat. Technol.* **2011**, *205*, S364–S368. [[CrossRef](#)]
7. Murugan, K.; Ragupathy, A.; Balasubramanian, V.; Sridhar, K. Optimizing HVOF spray process parameters to attain minimum porosity and maximum hardness in WC-10Co-4Cr coatings. *Surf. Coat. Technol.* **2014**, *247*, 90–102. [[CrossRef](#)]

8. Straffelini, G. *Friction and Wear Methodologies for Design and Control*; Springer International Publishing: Cham, Switzerland, 2015; ISBN 9783319058931.
9. Thermsuk, S.; Surin, P. Optimization Parameters of WC-12Co HVOF Sprayed Coatings on SUS 400 Stainless Steel. *Procedia Manuf.* **2019**, *30*, 506–513. [[CrossRef](#)]
10. Wang, Q.; Chen, Z.; Li, L.; Yang, G. The parameters optimization and abrasion wear mechanism of liquid fuel HVOF sprayed bimodal WC-12Co coating. *Surf. Coat. Technol.* **2012**, *206*, 2233–2241. [[CrossRef](#)]
11. Nahvi, S.M.; Jafari, M. Microstructural and mechanical properties of advanced HVOF-sprayed WC-based cermet coatings. *Surf. Coat. Technol.* **2016**, *286*, 95–102. [[CrossRef](#)]
12. Murthy, J.K.N.; Venkataraman, B. Abrasive wear behaviour of WC–CoCr and Cr₃C₂–20(NiCr) deposited by HVOF and detonation spray processes. *Surf. Coat. Technol.* **2006**, *200*, 2642–2652. [[CrossRef](#)]
13. Skandan, G.; Yao, R.; Kear, B.H.; Qiao, Y.; Liu, L.; Fischer, T.E. Multimodal powders: A new class of feedstock material for thermal spraying of hard coatings. *Scr. Mater.* **2001**, *44*, 1699–1702. [[CrossRef](#)]
14. Sahraoui, T.; Fenineche, N.E.; Montavon, G.; Coddet, C. Structure and wear behaviour of HVOF sprayed Cr₃C₂-NiCr and WC-Co coatings. *Mater. Des.* **2003**, *24*, 309–313. [[CrossRef](#)]
15. Zimmermann, S.; Kreye, H. Chromium carbide coatings produced with various HVOF spray systems. In Proceedings of the Thermal Spray Practical Solutions for Engineering Problems. In Proceedings of the 9th National Thermal Spray Conference, Cincinnati, OH, USA, 7–11 October 1996; Berndt, C.C., Ed.; ASM International: Materials Park, OH, USA, 1996; pp. 147–152.
16. Usmani, S.; Sampath, S.; Houck, D.L.; Lee, D. Effect of Carbide Grain Size on the Sliding and Abrasive Wear Behavior of Thermally Sprayed WC-Co Coatings. *Tribol. Trans.* **1997**, *40*, 470–478. [[CrossRef](#)]
17. La Vecchia, G.M.; Mor, F.; Straffelini, G.; Doni, D. Microstructure and sliding wear behaviour of thermal spray carbide coatings. *Int. J. Powder Metall.* **1999**, *35*, 37–46.
18. Sudaprasert, T.; Shipway, P.H.; McCartney, D.G. Sliding wear behaviour of HVOF sprayed WC–Co coatings deposited with both gas-fuelled and liquid-fuelled systems. *Wear* **2003**, *255*, 943–949. [[CrossRef](#)]
19. Picas, J.A.; Punset, M.; Menargues, S.; Martín, E.; Baile, M.T. Microstructural and tribological studies of as-sprayed and heat-treated HVOF Cr₃C₂–CoNiCrAlY coatings with a CoNiCrAlY bond coat. *Surf. Coat. Technol.* **2015**, *268*, 317–324. [[CrossRef](#)]
20. Bolelli, G.; Berger, L.M.; Bonetti, M.; Lusvarghi, L. Comparative study of the dry sliding wear behaviour of HVOF-sprayed WC-(W,Cr)2C-Ni and WC-CoCr hardmetal coatings. *Wear* **2014**, *309*, 96–111. [[CrossRef](#)]
21. Fedrizzi, L.; Valentinelli, L.; Rossi, S.; Segna, S. Tribocorrosion behaviour of HVOF cermet coatings. *Corros. Sci.* **2007**, *49*, 2781–2799. [[CrossRef](#)]
22. Zhang, W.C.; Liu, L.B.; Zhang, M.T.; Huang, G.X.; Liang, J.S.; Li, X.; Zhang, L.G. Comparison between WC-10Co-4Cr and Cr₃C₂-25NiCr coatings sprayed on H13 steel by HVOF. *Trans. Nonferrous Met. Soc. China (English Ed.)* **2015**, *25*, 3700–3707. [[CrossRef](#)]
23. Yuan, J.; Ma, C.; Yang, S.; Yu, Z.; Li, H. Improving the wear resistance of HVOF sprayed WC-Co coatings by adding submicron-sized WC particles at the splats' interfaces. *Surf. Coat. Technol.* **2016**, *285*, 17–23. [[CrossRef](#)]
24. Milanti, A.; Koivuluoto, H.; Vuoristo, P.; Bolelli, G.; Bozza, F.; Lusvarghi, L. Microstructural Characteristics and Tribological Behavior of HVOF-Sprayed Novel Fe-Based Alloy Coatings. *Coatings* **2014**, *4*, 98–120. [[CrossRef](#)]
25. Shin, J.H.; Wang, Q.M.; Kim, K.H. Microstructural evolution and tribological behavior of Mo–Cu–N coatings as a function of Cu content. *Mater. Chem. Phys.* **2011**, *130*, 870–879. [[CrossRef](#)]
26. Tian, B.; Yue, W.; Fu, Z.; Gu, Y.; Wang, C.; Liu, J. Surface properties of Mo-implanted PVD TiN coatings using MEVVA source. *Appl. Surf. Sci.* **2013**, *280*, 482–488. [[CrossRef](#)]
27. Woydt, M.; Skopp, A.; Witke, D.K. Wear engineering oxides/anti-wear oxides. *Wear* **1998**, *218*, 84–95. [[CrossRef](#)]
28. Terajima, T.; Takeuchi, F.; Nakata, K.; Adachi, S.; Nakashima, K.; Igarashi, T. Composite coating containing WC/12Co cermet and Fe-based metallic glass deposited by high-velocity oxygen fuel spraying. *J. Alloy. Compd.* **2010**, *504*, S288–S291. [[CrossRef](#)]
29. Bolelli, G.; Börner, T.; Bozza, F.; Cannillo, V.; Cirillo, G.; Lusvarghi, L. Cermet coatings with Fe-based matrix as alternative to WC–CoCr: Mechanical and tribological behaviours. *Surf. Coat. Technol.* **2012**, *206*, 4079–4094. [[CrossRef](#)]

30. Bolelli, G.; Bursi, M.; Lusvarghi, L.; Manfredini, T.; Matikainen, V.; Rigon, R.; Sassatelli, P.; Vuoristo, P. Tribology of FeVCrC coatings deposited by HVOF and HVAF thermal spray processes. *Wear* **2018**, *394–395*, 113–133. [CrossRef]
31. Bolelli, G.; Colella, A.; Lusvarghi, L.; Puddu, P.; Rigon, R.; Sassatelli, P.; Testa, V. Properties of HVOF-sprayed TiC-FeCrAl coatings. *Wear* **2019**, *418–419*, 36–51. [CrossRef]
32. Federici, M.; Menapace, C.; Moscatelli, A.; Gialanella, S.; Straffelini, G. Pin-on-disc study of a friction material dry sliding against HVOF coated discs at room temperature and 300 °C. *Tribol. Int.* **2017**, *115*, 89–99. [CrossRef]
33. Watremez, M.; Bricout, J.P.; Marguet, B.; Oudin, J. Friction, Temperature, and Wear Analysis for Ceramic Coated Brake Disks. *J. Tribol.* **1996**, *118*, 457. [CrossRef]
34. Öz, A.; Gürbüz, H.; Yakut, A.K.; Sağıroğlu, S. Braking performance and noise in excessive worn brake discs coated with HVOF thermal spray process. *J. Mech. Sci. Technol.* **2017**, *31*, 535–543. [CrossRef]
35. Wahlström, J.; Söderberg, A.; Olander, L.; Jansson, A.; Olofsson, U. A pin-on-disc simulation of airborne wear particles from disc brakes. *Wear* **2010**, *268*, 763–769. [CrossRef]
36. Federici, M.; Menapace, C.; Moscatelli, A.; Gialanella, S.; Straffelini, G. Effect of roughness on the wear behavior of HVOF coatings dry sliding against a friction material. *Wear* **2016**, *368–369*, 326–334. [CrossRef]
37. Federici, M.; Perricone, G.; Gialanella, S.; Straffelini, G. Sliding Behaviour of Friction Material Against Cermets Coatings: Pin-on-Disc Study of the Running-in Stage. *Tribol. Lett.* **2018**, *66*, 53. [CrossRef]
38. Wahlström, J.; Lyu, Y.; Matjeka, V.; Söderberg, A. A pin-on-disc tribometer study of disc brake contact pairs with respect to wear and airborne particle emissions. *Wear* **2017**, *384–385*, 124–130. [CrossRef]
39. Menapace, C.; Mancini, A.; Federici, M.; Straffelini, G.; Gialanella, S. Characterization of airborne wear debris produced by brake pads pressed against HVOF-coated discs. *Friction* **2019**, *8*, 421–432. [CrossRef]
40. ECHA. SVHC List. 2018. Available online: https://echa.europa.eu/it/candidate-list-table?p_p_id=dislists_WAR_dislistsportlet&p_p_lifecycle=1&p_p_state=normal&p_p_mode=view&p_p_col_id=column1&p_p_col_pos=2&p_p_col_count=3&dislists_WAR_dislistsportlet_javax.portlet.action=searchDislists (accessed on 1 June 2020).



© 2020 by the authors. Licensee MDPI, Basel, Switzerland. This article is an open access article distributed under the terms and conditions of the Creative Commons Attribution (CC BY) license (<http://creativecommons.org/licenses/by/4.0/>).

Article

Influence of Plasma Electrolytic Oxidation on Fatigue Behaviour of ZK60A-T5 Magnesium Alloy

Alessandro Morri , Lorella Ceschini , Carla Martini  and Alessandro Bernardi

Department of Industrial Engineering (DIN), Alma Mater Studiorum, University of Bologna, Viale Risorgimento 4, 40136 Bologna, Italy; lorella.ceschini@unibo.it (L.C.); carla.martini@unibo.it (C.M.); alessandr.bernardi10@studio.unibo.it (A.B.)

* Correspondence: alessandro.morri4@unibo.it

Received: 4 November 2020; Accepted: 1 December 2020; Published: 2 December 2020



Abstract: Magnesium alloys are used in the motorsport and aerospace fields because of their high specific strength. However, due to their low corrosion resistance, protective surface treatments, such as conversion coating or electroless plating, are necessary when they are used in humid or corrosive environments. The present study aimed at evaluating the effect of plasma electrolytic oxidation (PEO), followed by the deposition of a polymeric layer by powder coating, on the rotating bending fatigue behaviour of the wrought magnesium alloy ZK60A-T5. The specimens were extracted from forged wheels of racing motorbikes and were PEO treated and powder coated. Microstructural characterization was carried out by optical (OM) and scanning electron microscopy (SEM) to analyse both the bulk material and the multilayer, consisting of the anodic oxide interlayer with the powder coating top layer (about 40 μm total thickness). Rotating bending fatigue tests were carried out to obtain the S–N curve of PEO-treated specimens. The results of the rotating bending tests evidenced fatigue strength equal to 104 MPa at 10^6 cycles and 90 MPa at 10^7 cycles. The results of the investigation pointed out that PEO led to a reduction in fatigue strength between 14% and 17% in comparison to the untreated alloy. Fracture surface analyses of the fatigue specimens, carried out by SEM and by 3D digital microscopy, highlighted multiple crack initiation sites at the interface between the PEO layer and substrate, induced by the concurrent effects of coating defects, local tensile stresses in the substrate, and increased roughness at the substrate–coating interface.

Keywords: magnesium alloy; forging; fatigue; microstructure; plasma electrolytic oxidation (PEO); micro arc oxidation (MAO)

1. Introduction

Magnesium alloys, because of their low density, high specific strength, high damping capacity, and good castability [1–3], are attractive for lightweight applications in the automotive and aerospace industries, such as transmission housing, engine blocks, steering components, and wheels. Since many structural components are subjected to in-service cyclic stresses, the study of fatigue behaviour of both cast and wrought magnesium alloys, such as magnesium–zinc–zirconium (ZK) alloys, is gaining increasing interest [1,4–9].

Compared to other Mg alloys, ZK series show high strength and formability, mainly due to the presence of Zr, which acts as a grain refiner and leads to the development of a homogeneous equiaxed grain structure, not only in extruded but also in forged and cast-forged components [8]. In fact, even if Zn is added to produce age hardening by precipitation of intermetallic compounds, because of the moderate age hardening response of ZK alloys, the contribution of grain size strengthening is predominant [5]. For this reason, in recent years, some papers focused on the effects of the forging process on the ZK alloys' grain structure, widely used for the production of complex components.

Vasilev et al. [7] studied the effects of multiaxial isothermal forging (MIF) on the microstructure and fatigue behaviour of the as-cast ZK60 and demonstrated that MIF is able to refine coarse grains with a consequent improvement of the alloy fatigue response. Karparvarfard et al. compared the tensile and compressive behaviour [4] and the fatigue behaviour [8] of the as-cast and the cast-forged ZK60 alloy, concluding that the superior fatigue strength of the forged alloy compared to the as-cast one is due to grain refinement, the lower amount of porosities, and lower size of the intermetallics induced by plastic deformation.

Due to poor corrosion and wear resistance, when Mg components must be used in a humid or corrosive environment and/or an improvement of wear resistance is required, protective surface treatments are increasingly used [10–14]. For this reason, the fatigue strength of surface-treated Mg alloys has been attracting significant research interest in recent years.

Among surface modification techniques for magnesium alloys, Plasma Electrolytic Oxidation (PEO), also named Micro-Arc Oxidation (MAO), is a well-established solution for the improvement of wear and corrosion behaviour. PEO/MAO is an electrochemical conversion treatment applied not only to Mg alloys but also to Al and Ti alloys and other so-called valve metals [13,15]. This process is based on the modification of the growing anodic film by spark micro-discharges, initiated at potentials above the breakdown voltage of the oxide film [15]. Even though the PEO treatment generally improves wear and corrosion resistance, the production of a hard and rough PEO surface usually leads to a reduction in fatigue strength. This is mainly due to the generation of tensile residual stress during the oxidation treatment or to the presence of defects in the anodic layer, so that the conversion layer may be readily cracked when deformed [10,11,14].

Despite some drawbacks, these surface modification processes are widely used for the production of high-performance components. Up to now, however, only few data on the fatigue behaviour of anodized or PEO-treated magnesium alloys are available and to the best of our knowledge, no data about the effect of PEO treatment on the fatigue performance of ZK alloys are reported, even if these alloys find several applications in high strength aeronautic, military, and racing parts.

The available data on the effect of PEO on fatigue behaviour of Mg alloys, instead, concern the magnesium–gadolinium–rare earths (EV) and magnesium–aluminium–zinc (AZ) alloys [10,12,14]. Ceschini et al. [14] studied the influence of PEO on the fatigue behaviour of the sand cast EV31A Mg alloy. The results highlighted only a 15% reduction in fatigue strength of the PEO-treated alloy compared with the untreated, thanks to the low amount of defects and the good adhesion of the conversion layer. Similarly, Yerokhin et al. [10] demonstrated that PEO coating on the wrought AZ21 Mg alloy may cause no more than a 10% reduction in fatigue strength, which is lower than the effect of traditional anodizing. On the other hand, Nemcova et al. [12] showed a 35–40% reduction in fatigue properties of PEO-treated AZ61 wrought magnesium alloy with respect to the untreated one.

Based on the above, the present study aimed at evaluating the effect of PEO treatment on the rotating bending fatigue behaviour of a powder-coated ZK60A-T5 alloy. The samples were directly extracted from cast-forged wheels in order to test specimens with the same microstructure of the real component.

2. Materials and Methods

Samples used in the present investigation were extracted from forged wheels made of the ZK60A-T5 alloy (Figure 1), provided by Ducati Motor Holding SpA, Bologna (BO), Italy.

The nominal chemical composition of the investigated ZK60A alloy, reported in Table 1, is characterized by the presence of Zn to induce age hardening during heat treatment [5,16–18] and Zr as grain refiner [5,19,20].

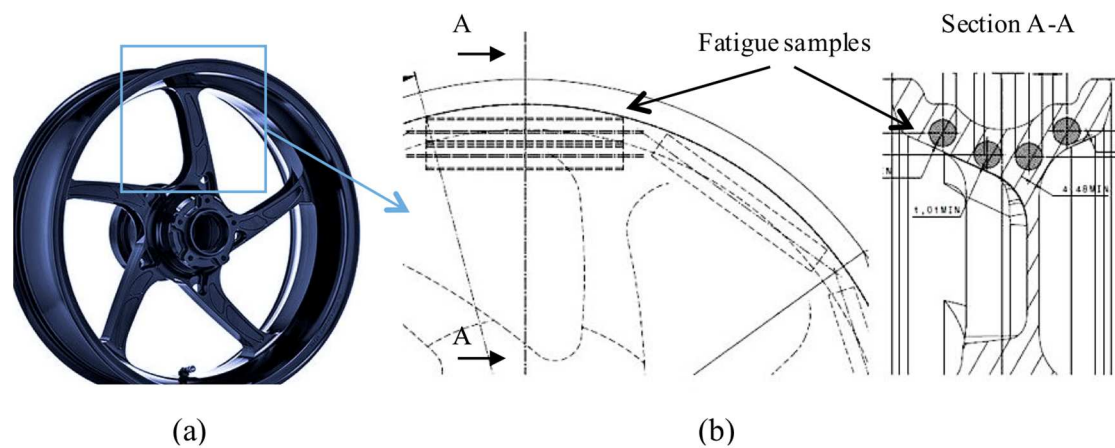


Figure 1. Wheel shape and dimensions (width 152 mm, diameter 431 mm) (a) and scheme of the fatigue samples extraction locations (b).

Table 1. Nominal chemical composition (wt.%) of the ZK60A magnesium alloy [21].

Zn	Zr	Other	Mg
4.8 ÷ 6.2	>0.45	<0.3	Bal.

The alloy was cast, forged, and T5 heat-treated according to the ASTM B 661 standard [22] to obtain the final geometry and increase the mechanical properties of the final wheel. The hot-working process was carried out at a temperature in the range 350–400 °C; immediately after forging, the wheels were water quenched and then, artificially aged at 150 °C for 24 h with final air cooling. Fatigue test samples were extracted from the wheels, as shown in Figure 1, and machined to the final geometry reported in Figure 2. Subsequently, they were PEO-treated and powder-coated. After PEO, the average surface roughness (R_a) was about 1.6 μm , but the deposition of the powder coating top layer decreased R_a down between 0.5 and 0.8 μm . The roughness was measured before and after deposition of the powder coating top layer by means of a stylus profilometer Hommelwerke T2000 (Hommelwerke, Schwenningen, Germany).

The PEO treatment was carried out in an industrial facility, using a dilute alkaline solution containing P-based as well as Zr-based compounds, above the dielectric breakdown potential of the anodic oxide in order to induce micro-arc discharges, which facilitates the growth of a thick layer and the incorporation of electrolyte compounds [13]. Further details on the forging process and the PEO treatment cannot be disclosed due to confidentiality reasons. A polymeric top layer was deposited above the PEO layer by powder coating (i.e., electrostatic painting) to improve the corrosion resistance of the component, as well as for aesthetical reasons. The polymeric top layer consisted of a carboxyl polyester resin.

Microstructural characterization was carried out using an Axio Imager optical microscope (OM; Zeiss, Oberkochen, Germany) and a scanning electron microscope (SEM) Tescan Mira-3 (Tescan, Brno, Czech Republic) equipped with an energy dispersive X-ray spectroscopy microprobe (EDS; Oxford Instruments, Abingdon, UK). The samples were prepared by standard metallographic techniques (grinding with SiC emery papers 800, 1200, and 2000 grit; polishing with diamond 9, 3, and 1 μm) and chemically etched with Kroll's reagent (HNO_3 4% HF 2% vol. with H_2O). Image analyses were carried out by the [®]Image Pro-Plus software (4.5) to evaluate the recrystallized fraction (induced by forging) and the average grain size, evaluated as the square root of the average grain area.

Brinell hardness tests were performed according to the ISO 6506 standard [23] using a 62.5 kg load and a 2.5 mm steel ball indenter (HB10).

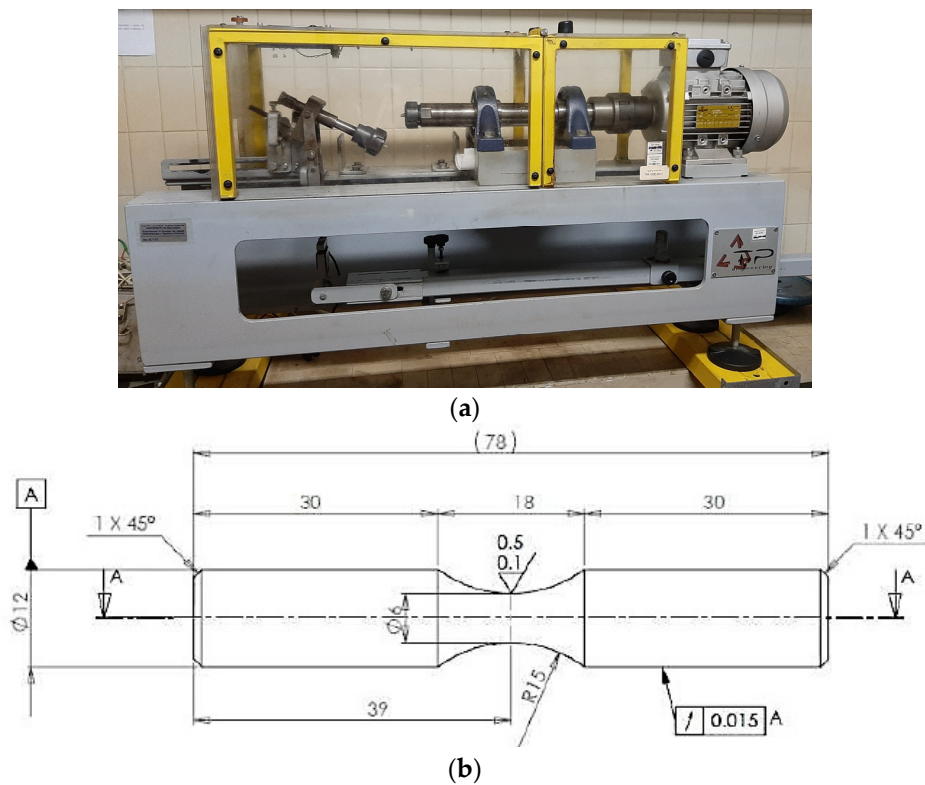


Figure 2. Three-point rotating bending machine (a); geometry and dimensions (mm) of fatigue specimens according to ISO 1143 [24] (b).

Fatigue tests were carried out by a three-point rotating bending machine (TP Engineering, Parma, Italy), shown in Figure 2, at a frequency of 47 Hz, at stress ratio $R = -1$, testing at least 4 samples at each stress level, in order to obtain the S–N curves according to ISO 1143 [24] and ISO 12107 [25] standards. The influence of the PEO treatment on the fatigue strength was investigated by comparing the experimental S–N curve to the literature data for the untreated alloy. The fracture surfaces, after fatigue failure, were analysed by 3D digital microscope Hirox KH-7700 (Hirox, Tokio, Japan) and by SEM–EDS.

3. Results and Discussion

3.1. Microstructure

Representative optical micrographs of the ZK60A-T5 forged alloy are reported in Figure 3, showing the presence of both large un-recrystallized dendrites oriented along the plastic flow (Figure 3a) and zones with fine and equiaxed recrystallized grains (Figure 3b) [8,26–29].

Grain size distribution (Figure 4), evaluated by image analysis, confirmed a bimodal grain structure, with an average grain size of about $4.5 \mu\text{m}$ for recrystallized grains and $24 \mu\text{m}$ for un-recrystallized dendrites, even if the length of some dendrites reached $150 \mu\text{m}$ (Figure 3). The area fraction of recrystallized grains is about 60%. This grain structure is probably ascribable to the synergic effect of localized plastic flow during forging [26] and to elements segregation in the dendrites [28,29].

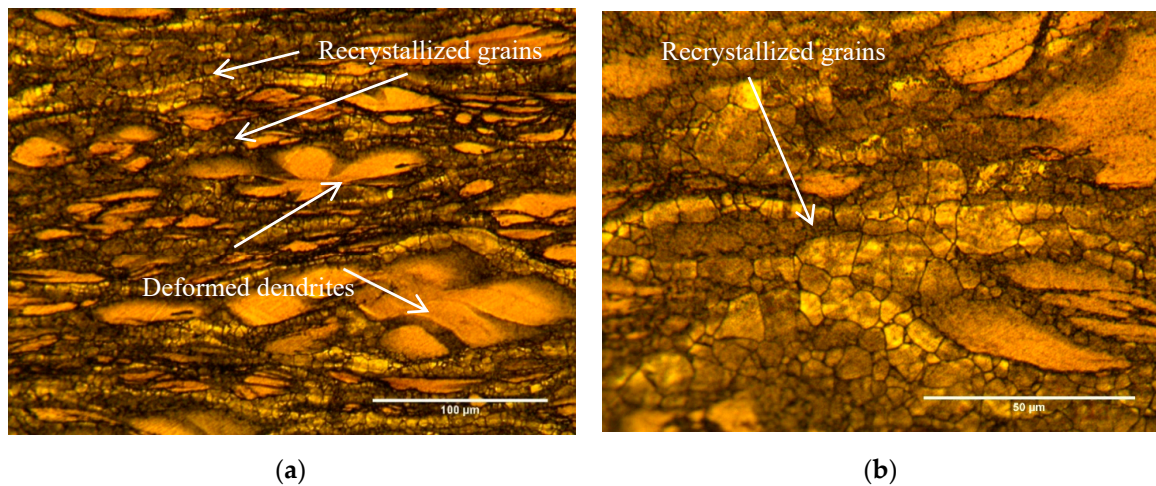


Figure 3. Optical microscope (OM) images of the bimodal grain structure of the ZK60A-T5 alloy etched with Kroll’s reagent. Large un-recrystallized dendrites oriented along the plastic flow direction (a); fine recrystallized grains (b). The specimen was extracted from an untested fatigue sample.

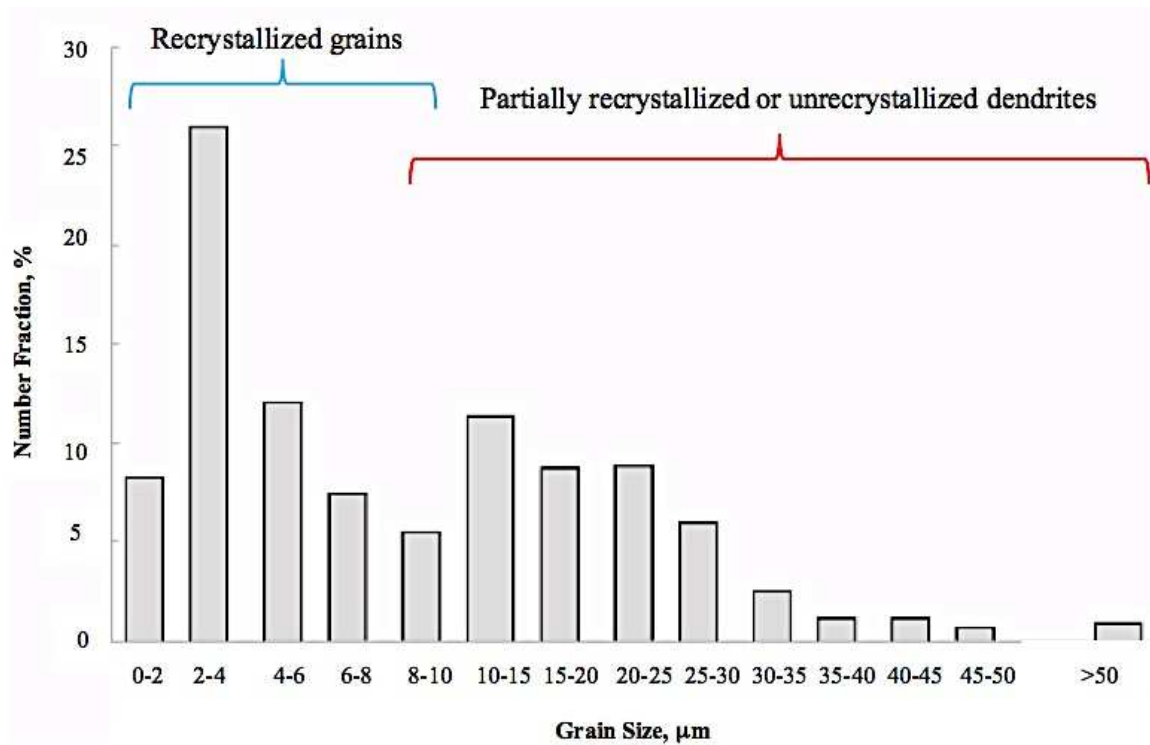


Figure 4. Grain size distribution of ZK60A-T5 microstructure, showing a bimodal distribution due to the presence of recrystallized grains, partially recrystallized, and un-recrystallized dendrites.

Moreover, SEM–EDS analyses pointed out the presence of micrometric Zn–Zr intermetallics at the dendrite boundaries (white in Figure 5a) and different amounts of Zn and Zr in the recrystallized equiaxed grains and un-recrystallized dendrites. In Figure 5, the light grey zones, with about 6.4 wt.% of Zn and 1.5 wt.% of Zr, correspond to un-recrystallized dendrites, while the dark grey ones, with about 4.5 wt.% of Zn and 0.5 wt.% of Zr, correspond to recrystallized grains. The higher amount of Zn and Zr in the dendritic zones is probably due to the presence of sub-micrometric and nanometric Zn–Zr based precipitates. These findings are in agreement with other authors [17,27–29], showing that during the recrystallization of Zn–Zr magnesium alloys, fine grains nucleate near the previous casting grain boundaries, while in the grain core, finely dispersed Zn–Zr submicrometric and nanometric

precipitates can pin dislocations and prevent the nucleation and growth of the new recrystallized grains. This process results in a “necklace” structure, caused by an incomplete dynamic recrystallization. Dynamic recrystallization (DRX) can occur during the hot deformation of metals and leads to the nucleation and growth of the new grains. Because during hot forging of the wheel, the alloy undergoes inhomogeneous strain rate and temperature fields, there is the possibility that in some regions, temperature or strain rate do not exceed the critical values of these parameters needed for DRX. In these regions, the recrystallization does not take place and therefore, the DRX is incomplete.

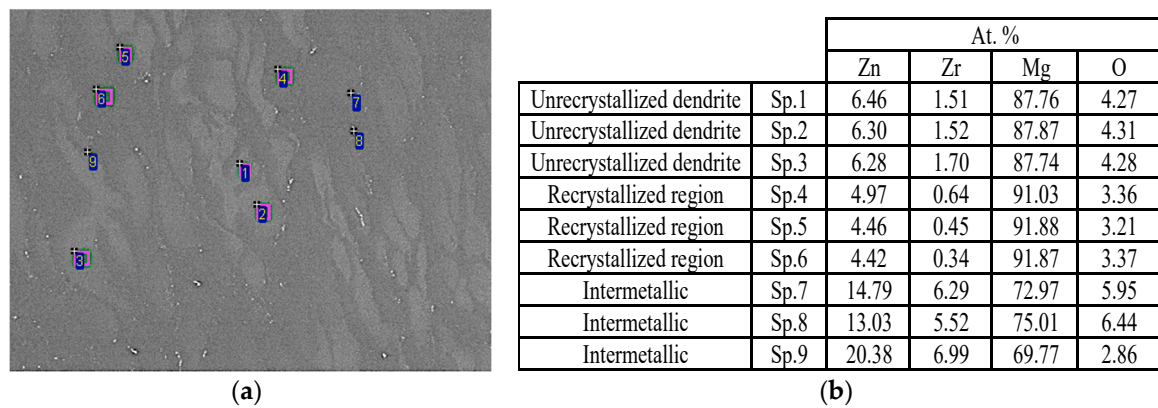


Figure 5. SEM image highlighting un-recrystallized dendrites (light grey), recrystallized grains (dark grey), and micrometric intermetallics (white) and the EDS analysis locations (spots—Sp.) (a); table with the results of EDS analyses (b).

Representative SEM micrographs of the polished cross-section of PEO and painting layers are reported in Figure 6. The average thicknesses of the PEO base layer and the powder coating top layer were 11 ± 3 and 26 ± 3 μm , respectively. The cross-sections revealed the typical micro-defective structure of PEO layers, due to discharge events which, on the one hand, favour coating growth and on the other, induce the formation of pores, microcracks, and microchannels, which can negatively affect fatigue strength [30,31]. Micro-arc discharge events also account for the typical micro-undulation of the interface with the substrate, due to localized inward coating growth [32].

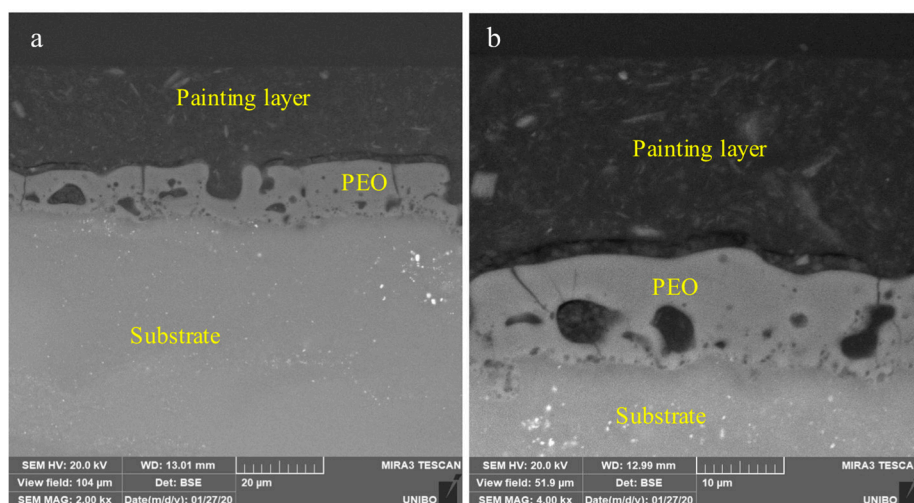


Figure 6. SEM images at low (a) and high (b) magnifications of PEO and painting layers cross-section. The cross-sections revealed the micro-defective structure of PEO layers: pores, microcracks, and microchannels. The SEM analyses were carried out on an untested fatigue sample.

The cross-section SEM–EDS images in Figure 7 highlight the rough, micro-undulated morphology of the PEO layer/alloy interface, as already pointed out by Figure 6. Moreover, EDS X-ray maps recorded on the polished cross-section (Figure 7) revealed a homogeneous distribution of phosphorus, zirconium, and oxygen in the PEO layer, due to incorporation of P- and Zr-based compounds from the electrolyte. Moreover, EDS maps also showed the presence of C (main constituent of the polymeric powder coating) as well as of Al- and Si-based compounds, typical inorganic fillers added to the powder coating top layer. Mechanical and fatigue properties of the polymeric top layer are not available. However, the effect of this type of layer on fatigue strength is usually considered negligible [11].

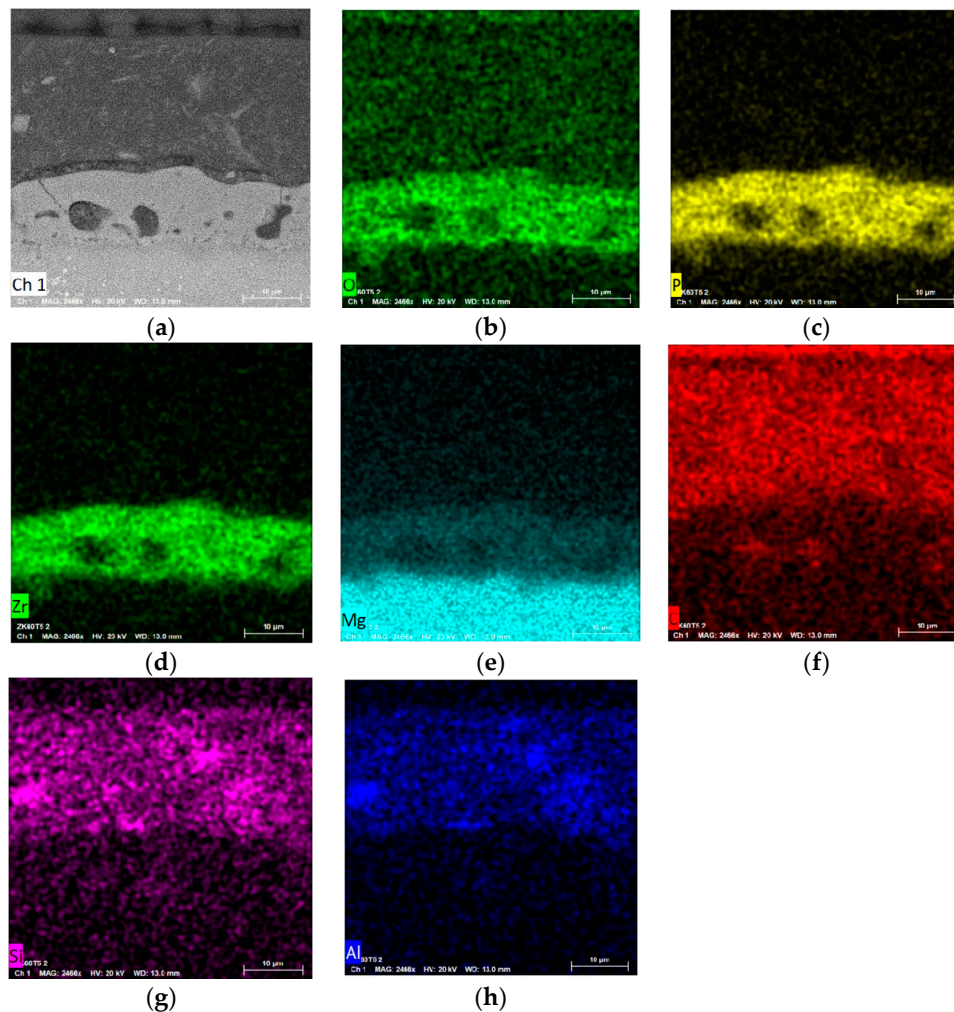


Figure 7. SEM–EDS and X-ray EDS elemental maps of a polished cross section of the ZK60A coated alloy. SEM image of PEO and painting layers cross-section (a); X-ray EDS elemental maps of the PEO base layer and powder coating top layer (b–h). The SEM–EDS analyses were carried out on an untested fatigue sample.

3.2. Mechanical Behaviour

The results of the hardness tests, carried out on the polished cross-section of metallographic samples of the ZK60A-T5 magnesium alloy extracted from the tested fatigue samples, gave hardness values between 70 and 71 HB10, which correspond to about 73–74 HV according to ASTM E 140-07 [33].

The results of the rotating bending fatigue tests, carried out by a three-point rotating bending testing machine according to ISO 12107 [25], are reported in the S–N curves of Figure 8, corresponding to a failure probability of 10% and 50%. In fact, since fatigue tests are typically characterized by large scatter, due to several factors like material inhomogeneity or incorrect specimen alignment,

statistical methods are necessary to evaluate the fatigue property of a material. Several approaches are reported in the standards [25], but usually for S–N curves, the mathematical analysis is performed to generate a curve corresponding to 50% probability of failure, although also other probabilities of failure (e.g., 10% or 90%) can be considered. According to the standard [25], the data at number of stresses represent a continuous single distribution that is log-normally distributed with constant variance as a function of stress; the failure probability represents the probability of failure of the tested material at a fixed stress within a defined number of loading cycles.

The fatigue strength for 50% probability of failure was equal to 104 MPa at 10^6 cycles and 90 MPa at 10^7 cycles. A comparison of these data with the literature data for the forged ZK60A-T6 alloy without PEO treatment [7,34] is reported in Figure 9. Slight differences can be observed in the S–N curves (failure probability of 50%), due to the differences in the forging processes of the alloy. In fact, while in [7] the data refer to a multiaxial isothermal forged and T6 heat treated alloy, the data reported in [34] concern a uniaxial forged and T6 heat-treated alloy.

The comparison of the literature fatigue data for the untreated ZK60A-T6 alloy [7] with those obtained in the present study for the PEO-treated alloy (Figure 9) showed that PEO induced a 4% decrease in the alloy fatigue strength at 10^6 cycles (108 vs. 104 MPa) and a 14% decrease at 10^7 cycles (104 vs. 90 MPa). When comparing the fatigue behaviour of the PEO-treated alloy with those reported for the untreated substrate in [34], the reduction in fatigue strength was 8% at 10^6 cycles (113 vs. 104 MPa) and 17% at 10^7 cycles (108 vs. 90 MPa).

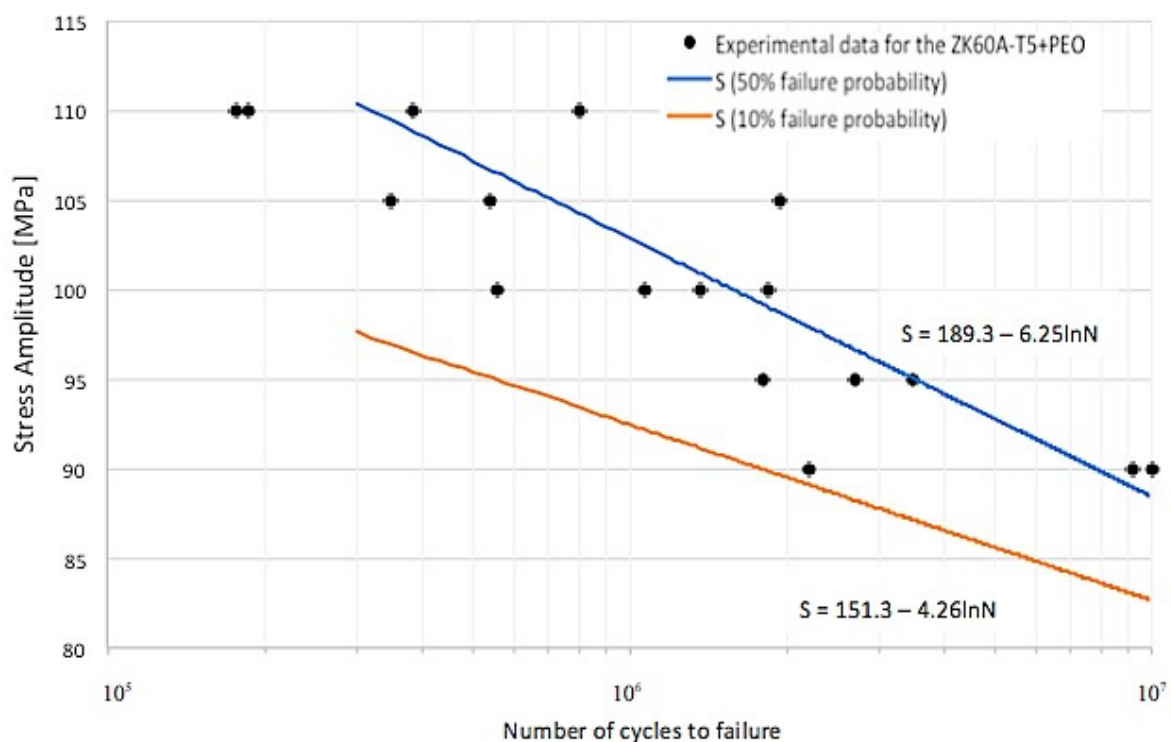


Figure 8. Stress amplitude versus number of cycles to failure (S–N curves) of the PEO-treated and powder coated ZK60A-T5 alloy (ZK60A-T5 + PEO), showing the typical linear fatigue response: the two straight lines correspond to 50% and 10% fatigue failure probability.

Similar results were also reported by Ceschini et al. [14] for the PEO-treated cast EV31A magnesium alloy, showing that the conversion treatment induced a 15% reduction in fatigue strength. Yerokhin et al. [10] also reported a fatigue strength reduction in the range 3–10% induced by PEO treatment on the extruded AZ21 alloy. Nemcova et al. [12], instead, showed a 35–40% reduction in fatigue properties of PEO-treated extruded AZ61 alloy compared to the untreated one. The detrimental influence of the PEO layer on fatigue behaviour of Mg alloys can be ascribed to a combination of factors

leading to enhanced surface stresses: high defect density and microcracks in the coating as well as roughness of the alloy/coating interface (Figures 6 and 7), which can produce multiple crack initiation sites [12].

According to [10,12–14], the reduction in fatigue strength, in fact, is mainly related to the intrinsic defectiveness of the ceramic conversion layer. The micro-discharges cause local melting of the growing oxide layer, inducing the formation of pores, microchannels, and microcracks, as well as the typical volcano-like surface features responsible for surface roughness increase. The subsequent very rapid solidification also generates tensile residual stresses that notoriously negatively affect fatigue strength.

In order to further confirm the previous assessments, an evaluation of the effect of PEO treatment on fatigue behaviour of the ZK60A-T5 alloy has been also carried out by comparing the results of fatigue tests with the fatigue strength of the untreated alloy evaluated from hardness data. According to [6], indeed, a good linear relationship can be established between rotating fatigue strength at 10^7 cycles and the hardness of different cast and wrought heat-treated magnesium alloys. The linear relationship between fatigue strength (S_f) and Vickers hardness of magnesium alloys is given by:

$$S_f \approx n \cdot HV \tag{1}$$

where HV is the Vickers hardness, and n is a coefficient generally equal to 1.32 and 1.66 for artificially and naturally aged alloys, respectively. On the basis of the fatigue strength and hardness values, the n coefficient for the PEO-treated ZK60A-T5 is approximately 1.21, which is about 10% lower than the value reported in [6] for artificially aged magnesium alloys. Therefore, the fatigue strength of the PEO-treated alloy is about 10% lower than the fatigue strength expected for an untreated alloy according to (1), that is equal to 98 MPa (Figure 9). This is in agreement with the results of the previous comparison of the experimental and literature fatigue data, respectively, for PEO-treated and untreated alloys.

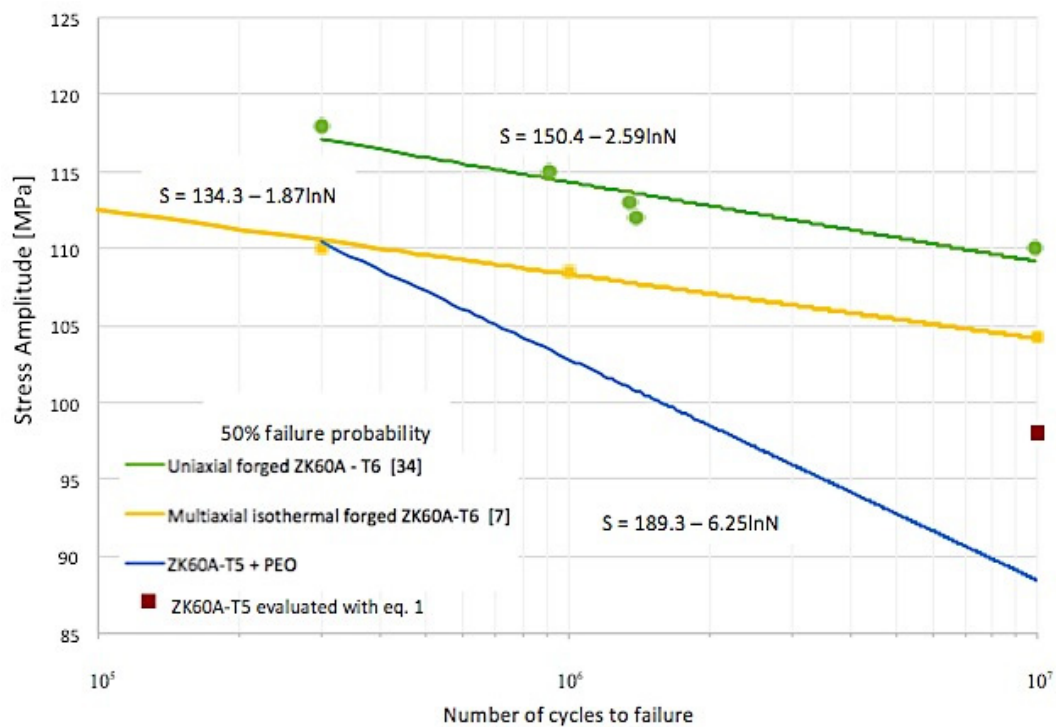


Figure 9. Comparison of the stress amplitude versus number of cycles to failure (S–N curves) at 50% failure probability of the PEO-treated ZK60A-T5 alloy (ZK60A-T5 + PEO), the uniaxial forged untreated ZK60A-T6 alloy [34], and the multiaxial isothermal forged untreated ZK60A-T6 alloy [7]. The fatigue strength for the ZK60A-T5 at 10^7 cycles, evaluated with Equation (1), is also reported.

3.3. Fracture Surfaces Analysis

Fractographic analyses were carried out firstly by 3D digital microscopy and then, by SEM. A representative low magnification micrograph of the fatigue fracture surface is reported in Figure 10. The surface is characterized by the presence of multiple and superficial nucleation sites, radial ratchet marks in the crack propagation region, and a rough feature in the final fracture zone due to overloading. The presence of the ratchet marks is a consequence of the multiple nucleation sites, since they develop when fatigue cracks, initiated at different positions and propagated in different planes, join together, creating steps on the fracture surface [35,36].

High magnification analyses of the nucleation sites (Figure 10b) pointed out the presence of zones with cracked, fragmented, and even detached PEO coating, which led to an increased roughness of the interface between substrate and PEO layer in comparison to the untested material. Therefore, the multiple nucleation sites, slightly below the specimen surface, could be the result of the synergic effect of the coating defects, tensile stresses in the substrate at the interface with the coating [10,12], and the increased roughness of the interface induced by fragmentation and debonding of the coating during cyclic loading. According to [11,12], in fact, not only tensile stresses in the substrate and coating defects, but also roughness at the interface, acting as a stress riser, can facilitate fatigue crack nucleation during cyclic loading.

Furthermore, the absence, next to the initiation sites, of typical forging defects (e.g., oxides), large intermetallics, or slip bands, that usually induce local stress concentration and the formation of cracks [36] confirms that the observed fatigue strength reduction is mainly due to the detrimental effect of the PEO layer whose typical microstructure facilitates crack nucleation.

A representative SEM image of the crack growth region is shown in Figure 11. The propagation zone (Figure 11a) shows the presence of classic fatigue striations, bright micro-cliffs, respectively, perpendicular and parallel to the direction of crack propagation [8,35], as well as secondary cracks probably due to the local strengthening of the matrix [8] or the activation of twinning during cycling loading [9]. Both for primary and secondary cracks, the crack path is mainly transgranular [12], as highlighted in the OM cross-sections in Figure 12.

SEM image of the overloading region in Figure 11b, instead, display a mixed morphology with quasi-cleavage features and zones with dimples and tear ridges, the latter typical of a ductile fracture [8].

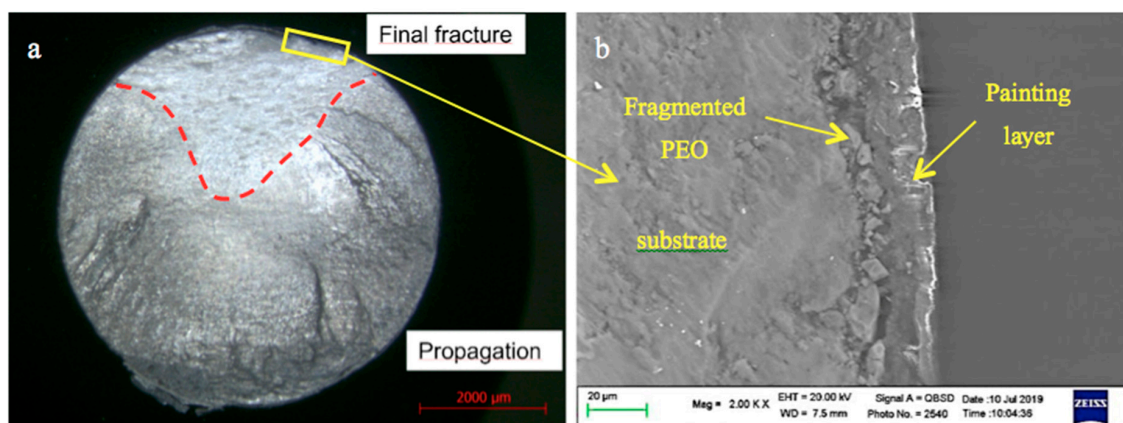


Figure 10. Representative 3D digital microscopy of the fracture surface of a PEO-treated ZK60A-T5 fatigue sample tested at 100 MPa and failed after 1.5×10^6 cycles (a); SEM image of the morphology of the PEO layer next to a crack nucleation site (b).

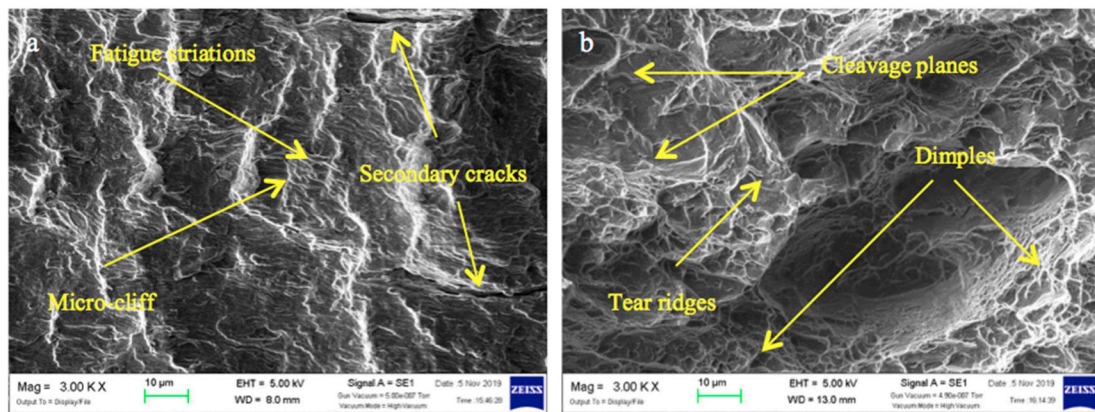


Figure 11. Representative SEM images at high magnification of the crack growth region with fatigue striations and secondary cracks (a), and of the overloading region with dimples and cleavage planes (b). Fatigue samples tested at 100 MPa and failed after 1.5×10^6 cycles.

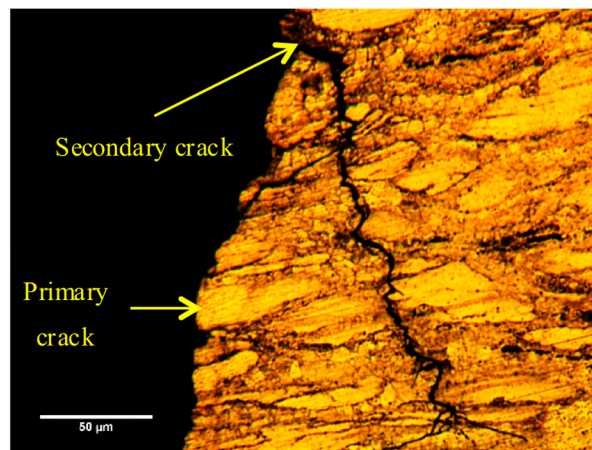


Figure 12. OM image of a fracture surface cross section, highlighting the presence of transgranular secondary cracks. Fatigue samples tested at 95 MPa and failed after 3.5×10^6 cycles.

4. Conclusions

The present study investigated the effect of PEO-treatment on fatigue behaviour of the ZK60A-T5 alloy by testing samples directly extracted from forged wheels under rotating bending conditions. The following conclusions can be drawn:

1. The microstructure of the alloy was partially recrystallized, with zones of fine equiaxed grains mixed with un-recrystallized dendrites, the latter characterized by a higher amount of Zr than the recrystallized ones.
2. The PEO coating was uniform but with the typical micro-defective structure of these layers such as pores, microcracks, and microchannels.
3. The PEO-treatment induced a fatigue strength reduction in the range of 14–17% at 10^7 cycles compared to the literature data for the untreated alloy.
4. The fatigue strength reduction is probably mainly related to the intrinsic defectiveness of the PEO and the residual tensile stresses generated during the treatment. These induce PEO layer fragmentation during cyclic loading, facilitating the formation of fatigue crack nucleation sites.

Author Contributions: Conceptualization, A.M., L.C., and C.M.; data curation, A.M. and A.B.; formal analysis, A.M., L.C., and C.M.; investigation, A.M. and A.B.; methodology, A.M., L.C., and C.M.; validation, A.M., C.M., and A.B.; writing—original draft, A.M. and A.B.; writing—review and editing, L.C. and C.M. All authors have read and agreed to the published version of the manuscript.

Funding: This research received no external funding.

Acknowledgments: This research did not receive any specific grant from funding agencies in the public, commercial, or not-for-profit sectors. We wish to thank Iuri Boromei at the Dept. of Industrial Engineering (University of Bologna) for SEM observations and EDS analyses of PEO-treated samples, as well as Andrea Morri for his support of experimental work. We also wish to thank Simone Messieri for providing fatigue samples.

Conflicts of Interest: The authors declare no conflict of interest.

References

1. Li, Z.M.; Wang, Q.G.; Luo, A.A.; Peng, L.M.; Fu, P.H.; Wang, Y.X. Improved high cycle fatigue properties of a new magnesium alloy. *Mater. Sci. Eng. A* **2013**, *582*, 170–177. [[CrossRef](#)]
2. Friedrich, H.; Schumann, S. Research for a “new age of magnesium” in the automotive industry. *J. Mater. Process. Technol.* **2001**, *117*, 276–281. [[CrossRef](#)]
3. Pantelakis, S.G.; Alexopoulos, N.D.; Chamos, S.N. Mechanical performance evaluation of cast magnesium alloys for automotive and aeronautical applications. *J. Eng. Mater. Technol.* **2007**, *129*, 422–430. [[CrossRef](#)]
4. Karparvarfard, S.M.H.; Shaha, S.K.; Behraves, S.B.; Jahed, H.; Williams, B.W. Microstructure, texture and mechanical behavior characterization of hot forged cast ZK60 magnesium alloy. *J. Mater. Sci. Technol.* **2017**, *33*, 907–918. [[CrossRef](#)]
5. Robson, J.D.; Paa-Rai, C. The interaction of grain refinement and ageing in magnesium–zinc–zirconium (ZK) alloys. *Acta Mater.* **2015**, *95*, 10–19. [[CrossRef](#)]
6. Li, Z.; Wang, Q.; Luo, A.A.; Fu, P.; Peng, L. Fatigue strength dependence on the ultimate tensile strength and hardness in magnesium alloys. *Int. J. Fatigue* **2015**, *80*, 468–476. [[CrossRef](#)]
7. Vasilev, E.; Linderov, M.; Nugmanov, D.; Sitdikov, O.; Markushev, M.; Vinogradov, A. Fatigue performance of Mg–Zn–Zr alloy processed by hot severe plastic deformation. *Metals* **2015**, *5*, 2316–2327. [[CrossRef](#)]
8. Karparvarfard, S.M.H.; Shaha, S.K.; Behraves, S.B.; Jahed, H.; Williams, B.W. Fatigue characteristics and modeling of cast and cast-forged ZK60 magnesium alloy. *J. Mater. Sci. Technol.* **2019**, *118*, 282–297. [[CrossRef](#)]
9. Yang, F.; Yin, S.M.; Li, S.X.; Zhang, Z.F. Crack initiation mechanism of extruded AZ31 magnesium alloy in the very high cycle fatigue regime. *Mater. Sci. Eng. A* **2008**, *491*, 131–136. [[CrossRef](#)]
10. Yerokhin, A.L.; Shatrov, A.; Samsonov, V.; Shashkov, P.; Leyland, A.; Matthews, A. Fatigue properties of keronite coatings on a magnesium alloy. *Surf. Coat. Technol.* **2004**, *182*, 78–84. [[CrossRef](#)]
11. Khan, S.A.; Miyashita, Y.; Mutoh, Y.; Koike, T. Effect of anodized layer thickness on fatigue behavior of magnesium alloy. *Mater. Sci. Eng. A* **2008**, *474*, 261–269. [[CrossRef](#)]
12. Nemcova, A.; Skeldon, P.; Thompson, G.E.; Morse, S.; Cizek, J.; Pacal, B. Influence of plasma electrolytic oxidation on fatigue performance of AZ61 magnesium alloy. *Corros. Sci.* **2014**, *82*, 58–66. [[CrossRef](#)]
13. Blawert, C.; Bala, P. Plasma electrolytic oxidation treatment of magnesium alloy. In *Surface Engineering of Light Alloys*; Dong, H., Ed.; Woodhead Publishing Limited: Cambridge, UK, 2010; pp. 155–183.
14. Ceschini, L.; Morri, A.; Angelini, V.; Messieri, S. Fatigue behavior of the rare earth rich EV31A Mg alloy: Influence of plasma electrolytic oxidation. *Metals* **2017**, *7*, 212. [[CrossRef](#)]
15. Yerokhin, A.L.; Nie, X.; Leyland, A.; Matthews, A.; Dowey, S.J. Plasma electrolysis for surface engineering. *Surf. Coat. Technol.* **1999**, *122*, 73–93. [[CrossRef](#)]
16. Chen, H.; Kang, S.B.; Yu, H.; Cho, J.; Kim, H.W.; Min, G. Effect of heat treatment on microstructure and mechanical properties of twin roll cast and sequential warm rolled ZK60 alloy sheets. *J. Alloy Compd.* **2009**, *476*, 324–328. [[CrossRef](#)]
17. Whalen, S.; Overman, N.; Joshi, V.; Varga, T.; Graff, D.; Lavender, C. Magnesium alloy ZK60 tubing made by shear assisted processing and extrusion (ShAPE). *Mater. Sci. Eng. A* **2019**, *755*, 278–288. [[CrossRef](#)]
18. Gao, X.; Nie, J.F. Characterization of strengthening precipitate phases in a Mg–Zn alloy. *Scr. Mater.* **2007**, *56*, 645–648. [[CrossRef](#)]
19. Volkova, E.F. Microstructural and mechanical characterization of magnesium based alloy MA14 (ZK60 A): Evolution under deformation and heat treatment. *WIT Trans. Built Environ.* **2014**, *137*, 17–23.
20. Sun, M.; Easton, M.A.; StJohn, D.H.; Wu, G.; Abbott, T.B.; Ding, W. Grain refinement of magnesium alloys by Mg–Zr Master Alloys: The role of alloy chemistry and Zr particle number density. *Adv. Eng. Mater.* **2013**, *15*, 373–378. [[CrossRef](#)]

21. ASTM B91-17, *Standard Specification for Magnesium-Alloy Forgings*; ASTM International: West Conshohocken, PA, USA, 2017; Available online: <http://www.astm.org/cgi-bin/resolver.cgi?B91> (accessed on 3 April 2020).
22. ASTM B661-12, *Standard Practice for Heat Treatment of Magnesium Alloys*; ASTM International: West Conshohocken, PA, USA, 2012; pp. 1–5. Available online: <http://www.astm.org/cgi-bin/resolver.cgi?B661-12> (accessed on 3 April 2020).
23. ISO 6506-1:2014 *Metallic Materials—Brinell Hardness Test—Part 1: Test Method*; International Organization for Standardization: Brussels, Belgium, 2014. Available online: <https://www.iso.org/obp/ui/#iso:std:iso:6506:-1:ed-3:v1:en> (accessed on 22 March 2020).
24. ISO 1143:2010 *Metallic Materials—Rotating Bar Bending Fatigue Testing*; International Organization for Standardization: Brussels, Belgium, 2010. Available online: <https://www.iso.org/obp/ui/#iso:std:41875:en> (accessed on 9 January 2020).
25. ISO 12107:2012 *Metallic Materials—Fatigue Testing—Statistical Planning and Analysis of Data*; International Organization for Standardization: Brussels, Belgium, 2012. Available online: <https://www.iso.org/obp/ui/#iso:std:iso:12107:ed-2:v1:en> (accessed on 9 January 2020).
26. Wang, C.Y.; Wang, X.J.; Chang, H.; Wu, K.; Zheng, M.Y. Processing maps for hot working of ZK60 magnesium alloy. *Mater. Sci. Eng. A* **2007**, *464*, 52–58. [[CrossRef](#)]
27. Jamali, A.; Mahmudi, R. Evolution of microstructure, texture, and mechanical properties in a multidirectionally forged ZK60 Mg alloy. *Mater. Sci. Eng. A* **2019**, *752*, 55–62. [[CrossRef](#)]
28. Hadadzadeh, A.; Mokdad, F.; Shalchi Amirkhiz, B.; Wells, M.A.; Williams, B.W.; Chen, D.L. Bimodal grain microstructure development during hot compression of a cast-homogenized Mg–Zn–Zr alloy. *Mater. Sci. Eng. A* **2018**, *724*, 421–430. [[CrossRef](#)]
29. Ohishi, K.; Mendis, C.L.; Homm, T.; Kamado, S.; Ohkubo, T.; Hono, K. Bimodally grained microstructure development during hot extrusion of Mg–2.4 Zn–0.1 Ag–0.1 Ca–0.16 Zr (at.%) alloys. *Acta Mater.* **2009**, *57*, 5593–5604. [[CrossRef](#)]
30. Arrabal, R.; Matykina, E.; Hashimoto, T.; Skeldon, P.; Thompson, G.E. Characterization of AC PEO coatings on magnesium alloys. *Surf. Coat. Technol.* **2009**, *203*, 2207–2220. [[CrossRef](#)]
31. Ko, Y.G.; Namgung, S.; Shin, D.H. Correlation between KOH concentration and surface properties of AZ91 magnesium alloy coated by plasma electrolytic oxidation. *Surf. Coat. Technol.* **2010**, *205*, 2525–2531. [[CrossRef](#)]
32. Gao, Y.; Yerokhin, A.; Parfenov, E.; Matthews, A. Application of Voltage Pulse Transient Analysis during Plasma Electrolytic Oxidation for Assessment of Characteristics and Corrosion Behaviour of Ca- and P-containing Coatings on Magnesium. *Electrochim. Acta* **2014**, *149*, 218–230. [[CrossRef](#)]
33. ASTM E140-12b. *Standard Hardness Conversion Tables for Metals Relationship among Brinell Hardness, Vickers Hardness, Rockwell Hardness, Superficial Hardness, Knoop Hardness, and Scleroscope Hardness*; ASTM International: West Conshohocken, PA, USA, 2002; pp. 1–25. Available online: <http://www.astm.org/cgi-bin/resolver.cgi?E140-12b> (accessed on 18 May 2020).
34. Shiozawa, K. *Databook on Fatigue Strength of Metallic Materials*; Elsevier: Amsterdam, The Netherlands, 1996.
35. Sachs, N.W. Understanding the surface features of fatigue fractures: How they describe the failure cause and the failure history. *J. Fail. Anal. Prev.* **2005**, *5*, 11–15. [[CrossRef](#)]
36. Becker, W.T.; Shipley, R.J. *ASM Handbook: Failure Analysis and Prevention*; ASM International: Materials Park, OH, USA, 2002; Volume 11, pp. 559–586.





Publisher’s Note: MDPI stays neutral with regard to jurisdictional claims in published maps and institutional affiliations.



© 2020 by the authors. Licensee MDPI, Basel, Switzerland. This article is an open access article distributed under the terms and conditions of the Creative Commons Attribution (CC BY) license (<http://creativecommons.org/licenses/by/4.0/>).

Article

The Effect of Co-Deposition of SiC Sub-Micron Particles and Heat Treatment on Wear Behaviour of Ni–P Coatings

Donya Ahmadkhaniha ^{1,*}, Lucia Lattanzi ^{2,*} , Fabio Bonora ², Annalisa Fortini ² , Mattia Merlin ²  and Caterina Zanella ¹ 

¹ Department of Materials and Manufacturing, Jönköping University, P.O. Box 1026, 55111 Jönköping, Sweden; caterina.zanella@ju.se

² Department of Engineering, University of Ferrara, Via Saragat 1, 44122 Ferrara, Italy; fabio01.bonora@edu.unife.it (F.B.); annalisa.fortini@unife.it (A.F.); mattia.merlin@unife.it (M.M.)

* Correspondence: donya.ahmadkhaniha@ju.se (D.A.); lucia.lattanzi@unife.it (L.L.)

Abstract: The purpose of the study is to assess the influence of SiC particles and heat treatment on the wear behaviour of Ni–P coatings when in contact with a 100Cr6 steel. Addition of reinforcing particles and heat treatment are two common methods to increase Ni–P hardness. Ball-on-disc wear tests coupled with SEM investigations were used to compare as-plated and heat-treated coatings, both pure and composite ones, and to evaluate the wear mechanisms. In the as-plated coatings, the presence of SiC particles determined higher friction coefficient and wear rate than the pure Ni–P coatings, despite the limited increase in hardness, of about 15%. The effect of SiC particles was shown in combination with heat treatment. The maximum hardness in pure Ni–P coating was achieved by heating at 400 °C for 1 h while for composite coatings heating for 2 h at 360 °C was sufficient to obtain the maximum hardness. The difference between the friction coefficient of composite and pure coatings was disclosed by heating at 300 °C for 2 h. In other cases, the coefficient of friction (COF) stabilised at similar values. The wear mechanisms involved were mainly abrasion and tribo-oxidation, with the formation of lubricant Fe oxides produced at the counterpart.

Keywords: electroplating; Ni–P coatings; SiC particles; heat treatment; wear



Citation: Ahmadkhaniha, D.; Lattanzi, L.; Bonora, F.; Fortini, A.; Merlin, M.; Zanella, C. The Effect of Co-Deposition of SiC Sub-Micron Particles and Heat Treatment on Wear Behaviour of Ni–P Coatings. *Coatings* **2021**, *11*, 180. <https://doi.org/10.3390/coatings11020180>

Academic Editor:

Armando Yáñez-Casal

Received: 8 January 2021

Accepted: 29 January 2021

Published: 3 February 2021

Publisher's Note: MDPI stays neutral with regard to jurisdictional claims in published maps and institutional affiliations.



Copyright: © 2021 by the authors. Licensee MDPI, Basel, Switzerland. This article is an open access article distributed under the terms and conditions of the Creative Commons Attribution (CC BY) license (<https://creativecommons.org/licenses/by/4.0/>).

1. Introduction

Coatings are often applied to industrial components to enhance the durability of materials in abrasive conditions or corrosive environments. Nickel-phosphorous (Ni–P) alloys are one of the most applied alternatives for applications such as aerospace, electronics, machinery, automotive, oil and gas [1–4]. Ni–P coatings have been mainly obtained through electroless plating [2]. However, due to the low overall speed (the deposition rate is only a few micrometres per hour) and continuous maintenance, electroplating could be a valid alternative [3]. The properties of Ni–P coatings depend on their phosphorus (P) content. Based on the P content, Ni–P coatings can be classified into low (2 wt.%–4 wt.%), medium (5 wt.%–9 wt.%) and high (>10 wt.%) P coatings, according to the ASTM B733-15 [5] standard. The increase of P leads to microstructural changes from crystalline to amorphous structures (P > 10 wt.%) [6,7]. Amorphous Ni–P coatings present good corrosion resistance with a hardness around ~600 HV. Heat treatment and addition of reinforcing particles (to produce composite coatings) can be applied to enhance the hardness of these coatings for the demanding situation. The hardness of the coatings depends on the heating time and temperature. Biswas et al. [8] studied the effect of heating temperature for 1 h on the tribological behaviour of Ni–P coatings. They obtained the maximum hardness of ~1085 HV0.1 at 400 °C, which slightly decreased to 975 HV0.1 at 600 °C. In the case of composite coatings, the nature of the reinforcing particles, their size, their percentage, and their distribution within the matrix can affect the hardness of the coatings [9–12]. Metzger et al. [13]

demonstrated that SiC and Al₂O₃ particles resulted in better wear resistance of Ni–P coatings than SiO₂ particles. Sliem et al. [14] co-deposited ZrO₂ nanoparticles in Ni–P coating by means of pulse electrodeposition and showed a gradual improvement in the mechanical properties of the coating. The hardness and modulus of the coating reached to the maximum value of 6.7 and 21.72 GPa, respectively, by adding 1 g/L ZrO₂ to the plating bath. Tamilarasan et al. [15] investigated the effect of surfactant on wear and friction behaviour of Ni–P/TiO₂ coatings. They found that by optimum concentration of the surfactants, a smoother surface with better distribution of TiO₂ particles were achieved which in turn resulted to low frictional coefficient, and high wear resistance.

Besides, the effect of heat treatment on properties of Ni–P composite coatings has also been investigated. Karthikeyan et al. [16] studied the effect of heat treatment on indentation behaviour of electroless Ni–P/Al₂O₃ coating. They reported that incorporation of Al₂O₃ nanoparticles induces strengthening. They also found that heat treatment results in the precipitation of Ni₃P intermetallic compound, which was increased with the heat treatment temperature up to 400 °C. However, the maximum hardness (16.4 GPa) was gained by heat treatment at 300 °C. Ram et al. [17] studied the wear behaviour of as deposited and heat-treated Ni–P and Ni–P/Al₂O₃ coatings in dry sliding conditions. Oxidation and adhesion in Ni–P coating and a combination of oxidation, adhesion, and abrasion in Ni–P/Al₂O₃ coatings were reported as the main wear mechanisms. They demonstrated that heat treatment enhanced the hardness of both Ni–P and Ni–P/Al₂O₃ coatings. The incorporation of Al₂O₃ nanoparticles reduced the propagation of micro cracks during the wear test of heat-treated coatings. Thus, maximum wear resistance was achieved for Ni–P/Al₂O₃ heat treated at 400 °C. De Hazan et al. [18] investigated three heat treatment procedures, at 270 °C for 10 h, 390 °C for 2 h, and 480 °C for 1 h. The authors observed a reduction in hardness HV0.3 of heat-treated Ni–P/SiO₂ coatings in all cases, while the wear resistance was improved. Chang et al. [19] annealed the Ni–P and Ni–P/SiC coatings at 200, 400, and 600 °C for 1 h. SiC particles led to increased hardness of minimum 30% compared to Ni–P coatings, in all the annealing conditions investigated. The authors also found a decreasing trend in hardness for heat-treated coatings at 600 °C, and they attributed it to an excessive number of porosities related to Ni₃P precipitation during heat treatment. Besides, heating at a temperature higher than 450 °C resulted in decomposition of SiC, which then reacted with Ni to form γ -Ni₅Si₂ and β -Ni₃Si phases and produced carbon (C) precipitation. Apachitei et al. [20] found that the heat treatments at 500 °C changed the deformation mechanisms in electroless Ni–P and reduced the Ni–P coatings' abrasive wear resistance. Besides, Ni₃Si formed, and the adhesion between the reinforcement and the matrix was improved. Aslanyan et al. [21] observed different wear mechanisms in Ni–P and composite coatings. Although the hardness of the coatings increased by heat treatment, composite coatings' wear rate was enhanced with respect to Ni–P one [22].

According to the above information, it is necessary to find a proper heat treatment procedure that can enhance the hardness and wear resistance of electrodeposited Ni–P and Ni–P composite coatings. The present study aims to evaluate the effect of SiC particles in combination with different heat treatment conditions on the wear behaviour of Ni–P coating. For this purpose, the effect of SiC particles addition on composition, hardness and wear resistance was evaluated to find out the relation between the composition and wear behaviour of Ni–P coatings. Besides, heat treatment on Ni–P as well as composite coatings was carried out and the wear behaviour of the heat-treated samples was studied to disclose any difference between the wear behaviour of heat-treated Ni–P and Ni–P/SiC coatings. For wear behaviour studies, the 100Cr6 steel was chosen as the antagonist in the wear system to describe non-abrasive conditions since the literature of electrodeposited Ni–P coatings investigated abrasive systems [15–21].

2. Experimental Methods

Ni–P coatings were deposited by direct plating on low alloyed steel (UNI EN ISO 683-4:2018 [22]) pins. The pins with the geometry shown in Figure 1 were machined by

computer numerical controlled HAAS CNC ST 10 lathe (Haas Automation, Oxnard, CA, USA). Before deposition, the steel substrates were ultrasonically cleaned in an alkaline soap and activated by pickling for 8 min in 2.5 M H_2SO_4 , between each step the samples were rinsed with distilled water.

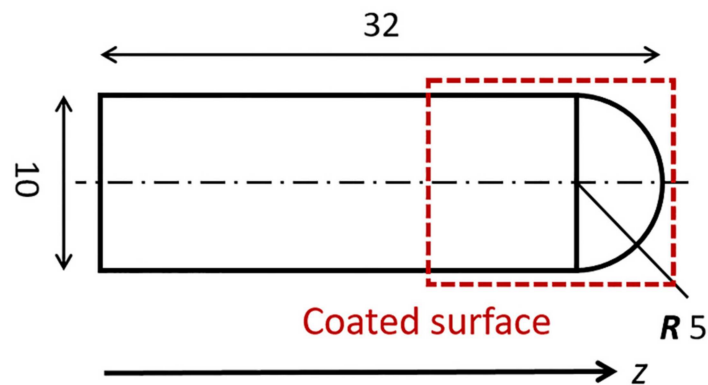


Figure 1. Dimensions of the pin in mm.

The electrodeposition was carried out in 2 L modified Watts bath containing $NiSO_4 \cdot 7H_2O$, $NiCl_2 \cdot 6H_2O$, H_3PO_3 , H_3BO_3 , and two additives (saccharin and sodium dodecyl sulfate). In the case of composite coatings, 20 g/L of SiC particles (β -SiC provided by Get Nano Materials, Saint-Cannat, France) were added to the electrolyte 24 h in advance, and they were stirred by a magnetic stirrer. The particles have an average particle size of 100 nm and irregular morphology. For better dispersion of the particles, the electrolyte was stirred ultrasonically for 30 min before plating. For deposition, the pin (cathode) was immersed in the electrolyte, and two pure bent Ni anode sheets surrounded it. The distance between anode and cathode was 5 cm. Two different cathode configurations were adopted for pure (Figure 2a) and composite (Figure 2b) coatings, the latter was chosen to achieve the maximum SiC particles co-deposition.

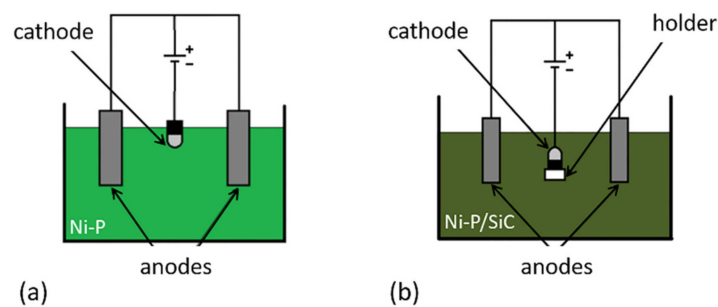


Figure 2. Configurations of the deposition cells for (a) pure coatings and (b) composite coatings.

The deposition was carried out at a current density of $4 A/dm^2$, for a total time of 105 min at $70^\circ C$ with a pH of 2.15. The deposition parameters were kept the same for pure and composite coatings. The deposited layers have an average thickness of about $38 \mu m$, depending on the current efficiency (CE). Different heat treatments, optimised in previous work [23] and listed in Table 1, were applied to some coated samples while the remaining were kept in the as-plated (AP) condition.

Table 1. Heat treatment conditions.

Heat Treatment	Temperature (°C)	Time (h)
HT300	300 °C	2
HT360	360 °C	2
HT400	400 °C	1

Surface morphology and composition of the coatings were characterised by a scanning electron microscope (SEM, JSM-7001F, JEOL, Akishima, Japan) equipped with energy dispersive spectroscopy (EDS, Octane Pro, EDAX, Mahwah, NJ, USA). The coatings' microhardness was measured on the cross-section of the pin by a Vickers indenter (NanoTest™ Vantage, 40.36, Micro Materials, Wrexham, UK) with a load of 200 mN and dwell time of 10 s. A total of 15 measurements were carried out on two samples for each investigated condition.

Wear tests were performed at room temperature in a ball-on-disc configuration, with uni-directional sliding, on a 100Cr6 steel (EN ISO 683-17 [24], AISI 52100) disc. The tests were carried out on a pin-on-disc tribometer (Pin-on-disc tester TR-20LE, Ducom instruments PVT LTD, Bangalore, India) with a load of 20 N under dry conditions. The tribometer tests were run at a constant linear sliding speed of 0.15 m/s and a total sliding length of 200 m for the as-plated samples and of 1000 m for the heat-treated samples. The trends of the coefficient of friction (COF) were acquired and registered during the tests. A minimum of three samples for each condition was tested. The wear debris and the worn surfaces on the pins were investigated by SEM (Evo MA15, Carl Zeiss Microscopy, Milan, Italy) coupled with EDS (Oxford Instruments, Abingdon, UK) analysis.

The tip surface of each pin was acquired before (Figure 3a) and after (Figure 3b) the wear test by a non-contact 3D optical profilometer (Talysurf CCI Lite, Taylor-Hobson Limited, Leicester, UK) with an optical resolution of 0.76 µm.

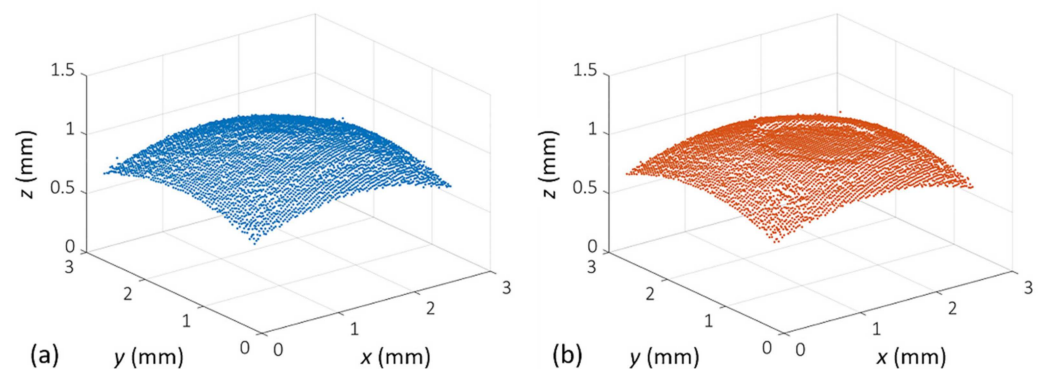


Figure 3. Point clouds of the pin tip surface from the profilometer acquisitions: (a) unworn; (b) worn, at the end of the wear test.

The comparison of the point clouds before and after wear enabled us to evaluate the volume loss with a tailored Matlab® code, integrating the volume under the point clouds of the surfaces. The wear rate (WR) was defined via Equation (1):

$$WR = \frac{\Delta V}{F \times L} \left(\frac{\text{mm}^3}{\text{N} \times \text{m}} \right) \quad (1)$$

where ΔV (mm³) is the volume loss, F (N) is the applied load, and L (m) is the total sliding length.

3. Results

3.1. Coating Appearance and Morphology

Figure 4 shows the coated pin with both Ni-P and Ni-P/SiC. The Ni-P coating (Figure 4a) had a shiny appearance while the Ni-P/SiC was a matt coating (Figure 4b). This difference was attributed to the presence of SiC particles, which increased the surface roughness of the coatings and therefore changed the reflection of the light.

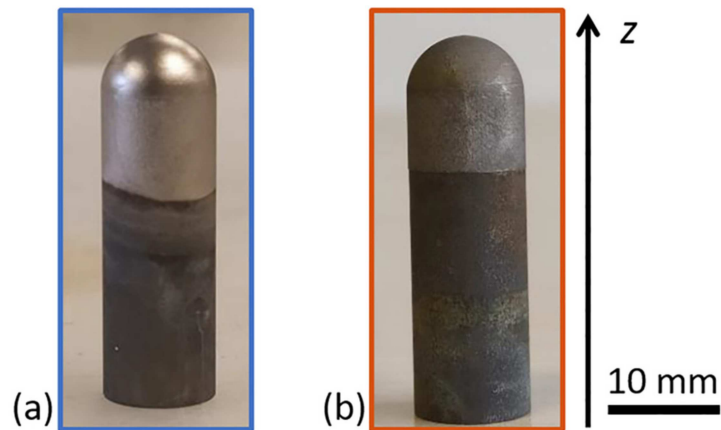


Figure 4. Coated pins with (a) Ni-P and (b) Ni-P/SiC coatings.

The morphology of the coatings on the surface of the pin can be seen in Figure 5. Figure 5a demonstrates a nodular morphology for Ni-P coating. In contrast, by adding SiC particles, the morphology was changed to smaller nodules than those in Ni-P (Figure 5b). A cross-sectional image of the composite coating (Figure 5c) exhibited the SiC particles distributed homogeneously along the coating thickness, as highlighted in the EDS map in Figure 5d. According to the SEM cross-section image, it was evident that SiC particles agglomerated during the coating process.

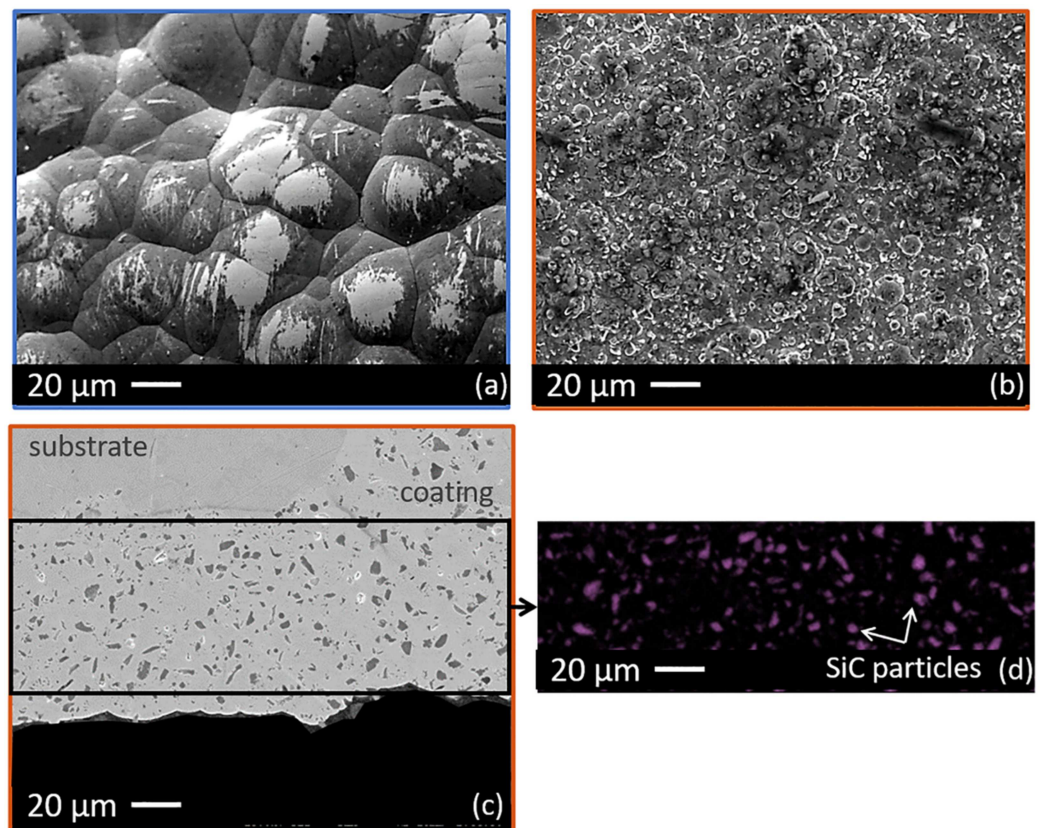


Figure 5. SEM image of (a) Ni-P surface and (b) Ni-P/SiC surface; (c) SEM image of the cross-section of Ni-P/SiC coating; and (d) EDS map of Si element related to (c).

The composition of the surface of the coatings was measured by EDS, and the results are listed in Table 2. Both Ni-P and Ni-P/SiC coating had more than 12 wt.% of P, and they were categorised as Ni high-P coatings. The addition of SiC particles slightly reduced the P content of the coating. This reduction was not observed in the previous study [25].

Table 2. Surface composition and current efficiency (CE) of Ni-P and Ni-P/SiC coatings.

Coating	P/(P + Ni) (wt.%)	SiC (wt.%)	CE
Ni-P	13.9 ± 0.08	–	$46\% \pm 8\%$
Ni-P/SiC	12.6 ± 0.03	11.3 ± 0.05	$45\% \pm 5\%$

Table 2 also lists the CE values of the exposition that was not affected by the addition of SiC particles.

3.2. Coatings Hardness

Coatings hardness was measured by Vickers indenter on the cross-section of the coatings, and the results are shown in Figure 6. Ni-P coating had 650 ± 30 HV0.02 and the addition of SiC particles increased the hardness values of 15% to 740 ± 10 HV0.02. However, heat treatment had more impact on enhancing the hardness values of these coatings. The maximum hardness in Ni-P coating was 1130 ± 30 HV0.02 achieved by HT400, while HT360 resulted in the maximum hardness of Ni-P/SiC coatings, 1240 ± 130 HV0.02.

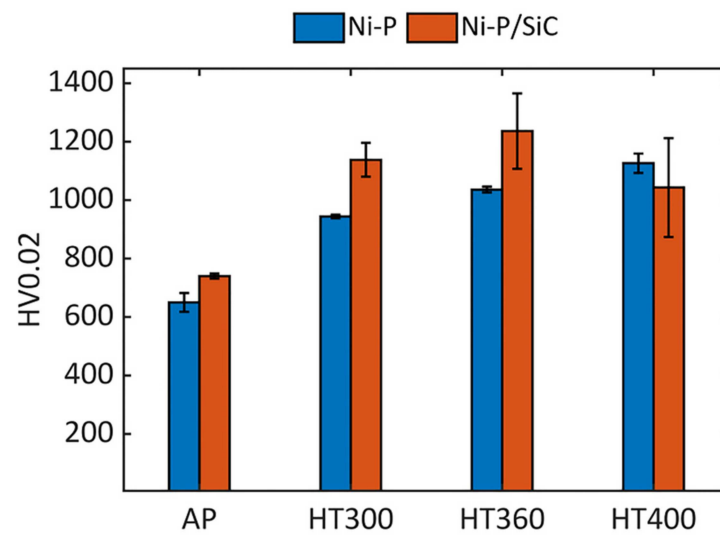


Figure 6. Microhardness valued of Ni-P and Ni-P/SiC coatings before and after heat treatments. Error bars represent standard deviation.

3.3. Wear

Coefficient of friction (COF) trends and wear rate of as-plated samples are represented in Figure 7. The COF evolution (Figure 7a) differed significantly with the presence of SiC particles. The average COF value for the Ni-P coating was 0.4, and it increased to 0.6, with the presence of SiC particles. Figure 7a shows one curve for each condition, the closest to the average, representing all tested samples. The wear rates (Figure 7b) did not differ significantly in the same condition, as all values are $\sim 10^{-5}$ mm³/Nm for the pure coating and $\sim 2 \times 10^{-5}$ mm³/Nm for the composite ones. Figure 7b gives the correspondent P and Si content on the pin tip for each wear rate value, the changes were not significant to influence the wear rate.

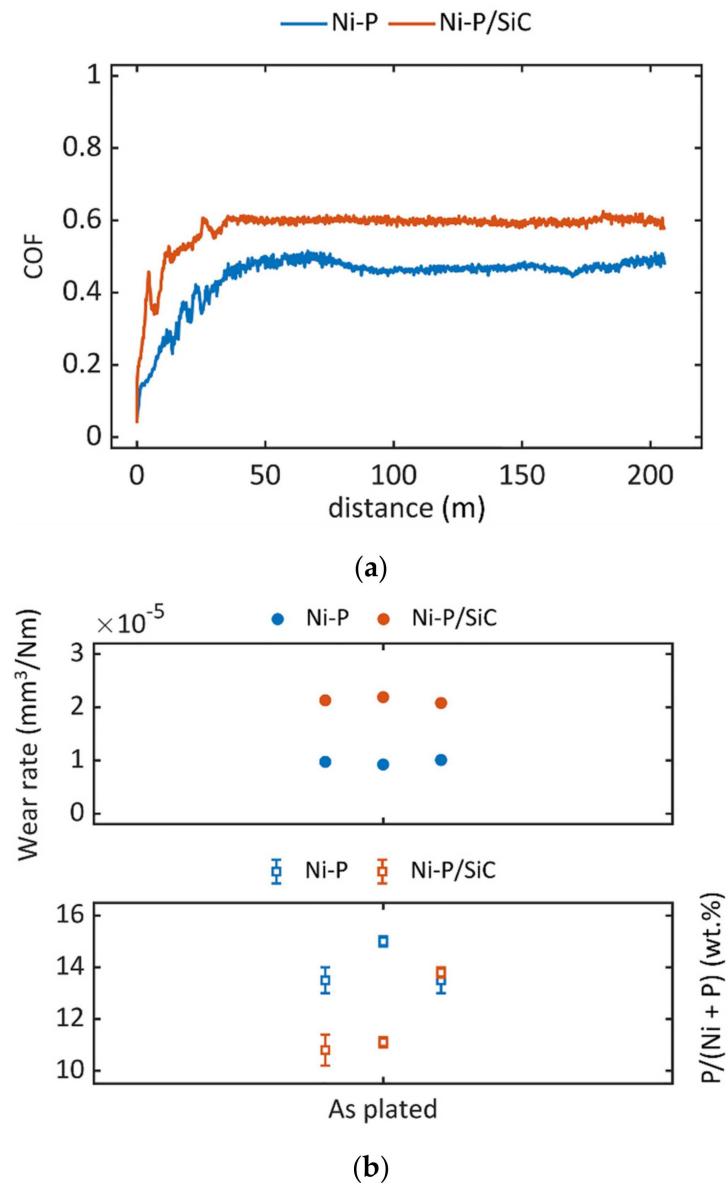


Figure 7. As-plated samples: (a) coefficient of friction (COF) evolution; (b) wear rate and P and Si content.

Representative wear tracks of the as-plated samples are depicted in Figure 8a for the Ni-P coatings, and Figure 8b for the composite ones. The yellow arrow in Figure 8a points at the residual layers of Fe oxides, coming from the antagonist, that adhere to the wear track. The representative wear track in Ni-P coating (Figure 8a) has a diameter of $\sim 600 \mu\text{m}$, smaller than the one of Ni-P/SiC coating (Figure 8b) with a diameter of $\sim 800 \mu\text{m}$. This observation mirrors the comparison of wear rate values in Figure 7b. In all cases, the substrate was not reached during the wear test.

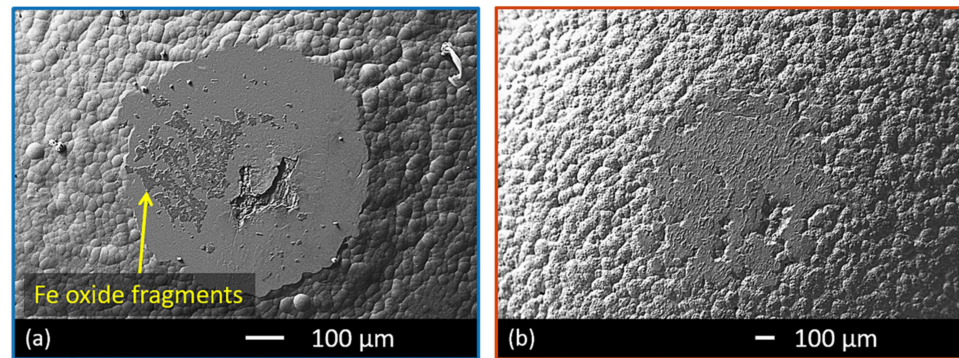
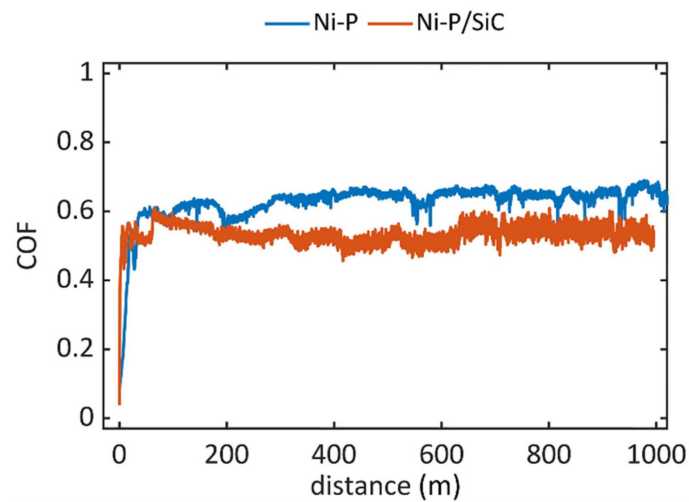
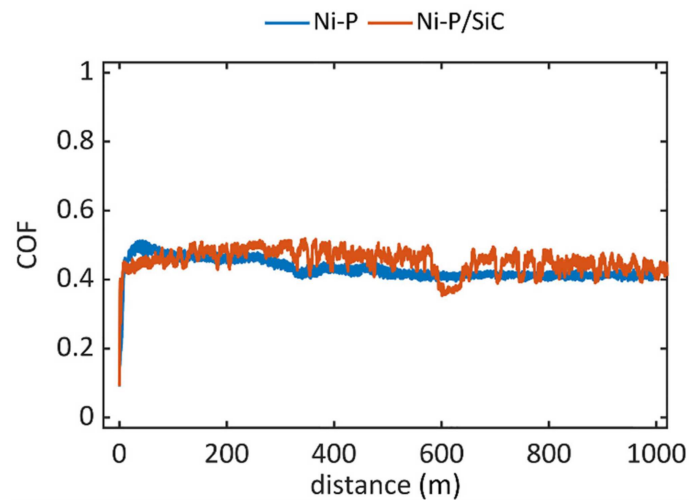


Figure 8. Wear tracks of the as-plated samples: (a) Ni-P; (b) Ni-P/SiC.

Figure 9 depicts the COF evolution and wear rate of heat-treated samples. For HT300 samples (Figure 9a), the presence of SiC particles determined a slight decrease in the average COF, from ~ 0.65 to ~ 0.5 . On the contrary, the COF curves reached the stable state at the same value for pure and composite coating in HT360 (Figure 9b) and HT400 (Figure 9c) treatments. Figure 9d gives the correspondent P and Si content on the pin tip for each sample as even small changes could influence the precipitation during the HT.

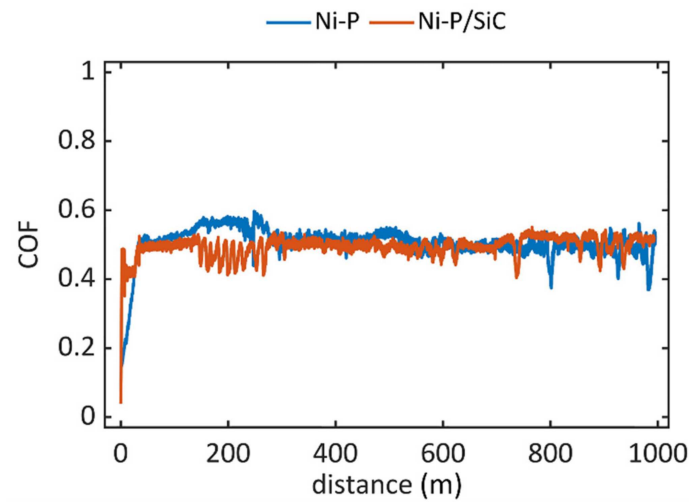


(a)

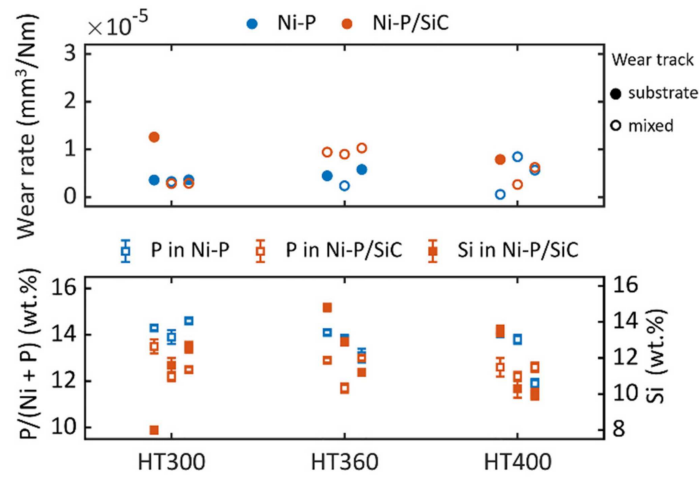


(b)

Figure 9. Cont.



(c)



(d)

Figure 9. Heat-treated samples: (a) COF evolution of HT300; (b) COF evolution of HT360; (c) COF evolution of HT400; (d) wear rate and P content.

Figure 10 depicts the representative wear tracks for pure and composite coatings in each heat-treated condition: HT300 (Figure 10a,b), HT360 (Figure 10c,d) and HT400 (Figure 10e,f). In some cases the substrate steel was reached during wear, as visible for example in Figure 10a; in others, the wear track presented a mixed surface, characterised by substrate, coating residuals and Fe oxides originated from the antagonist (Figure 10d).

No specific trends were evident, as summarised in Table 3, although the substrate was reached more times with the pure coatings than with the composite ones. The different occurrence can be ascribed to local features, like the local thickness of the coating.

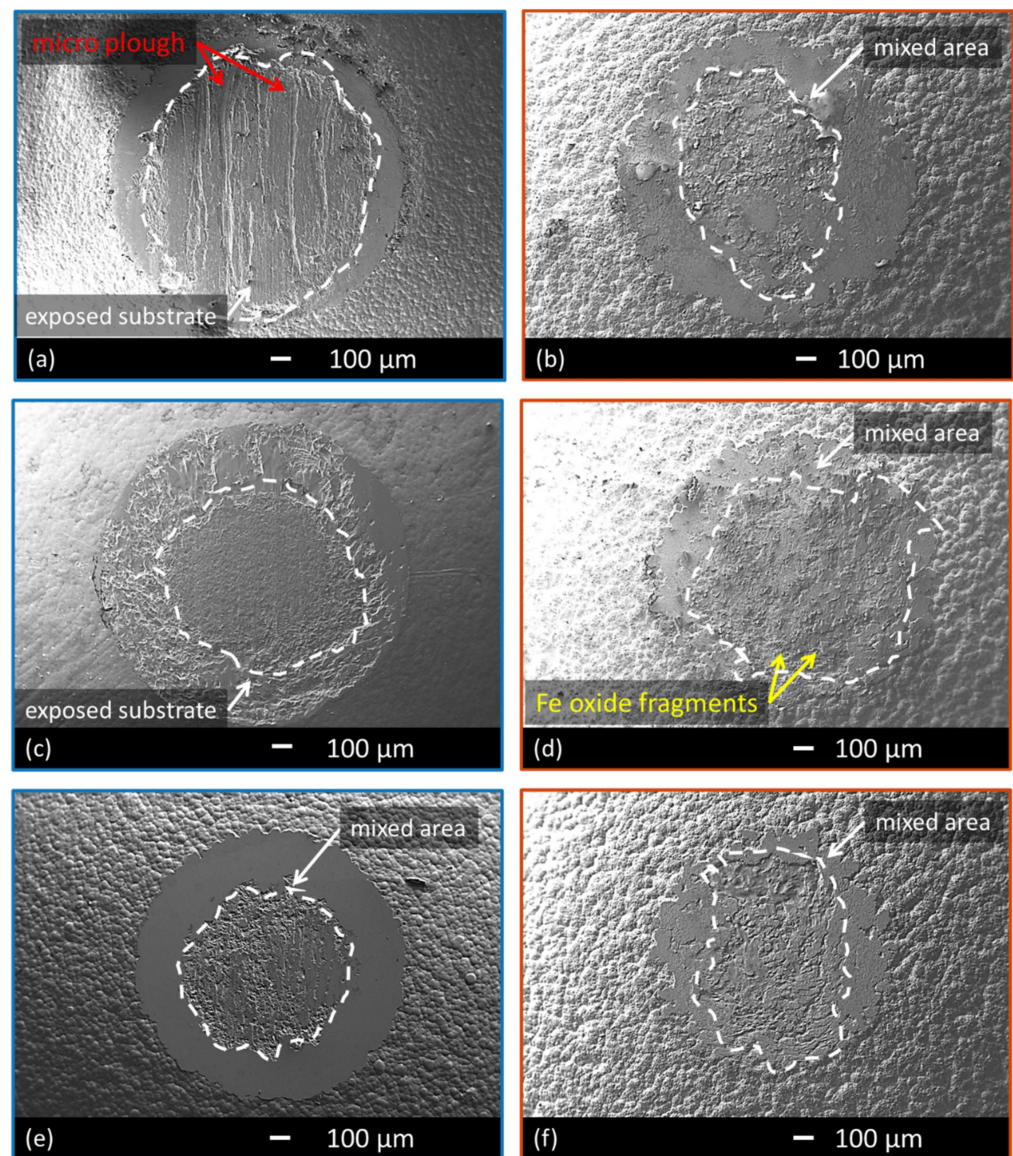


Figure 10. Wear tracks, after acetone rinsing, of the heat-treated samples: for HT300 treatment, (a) Ni-P and (b) Ni-P/SiC; for HT360 treatment, (c) Ni-P and (d) Ni-P/SiC; for HT400 treatment, (e) Ni-P and (f) Ni-P/SiC.

Table 3. Wear rate and surface condition of the wear track of Ni-P and Ni-P/SiC coatings.

Coating	Repetition	HT300		HT360		HT400	
		Wear Rate (mm ³ /Nm)	Surface	Wear Rate (mm ³ /Nm)	Surface	Wear Rate (mm ³ /Nm)	Surface
Ni-P	i	3.6×10^{-6}	substrate	4.5×10^{-6}	substrate	5.9×10^{-7}	mixed
	ii	3.3×10^{-6}	mixed	2.4×10^{-6}	mixed	8.5×10^{-6}	mixed
	iii	3.7×10^{-6}	substrate	5.8×10^{-6}	substrate	5.7×10^{-6}	mixed
Ni-P/SiC	i	1.2×10^{-5}	substrate	9.4×10^{-6}	mixed	7.9×10^{-6}	substrate
	ii	2.9×10^{-6}	mixed	9.0×10^{-6}	mixed	2.7×10^{-6}	mixed
	iii	2.9×10^{-6}	mixed	1.0×10^{-5}	mixed	6.2×10^{-6}	mixed

4. Discussion

4.1. As-Plated Coatings

Addition of SiC particles reduced the P content of the coating by 10%, although this reduction was not seen in the previous study [25]. This decrease can be related to the significant amount of co-deposited SiC, around 11 wt.% in this study. It has been reported that for Ni plating at low pH, SiC particles enhance the hydrogen (H₂) evolution by absorbing protons on their surfaces [26,27] and consequently, results in increased hydrogen evolution. Therefore, the nascent H₂ required for reducing P source to phosphine (according to the indirect reactions) [28] is decreased, hence reducing the P content in the coating. Besides, a CE reduction is expected by the P decrease in the coatings due to the H₂ catalysis by SiC particles. In this study, the CE for Ni–P and Ni–P/SiC coatings were comparable, as seen in Table 2.

The wear mechanism involved in these coatings consisted of abrasion and tribo-oxidation. Abrasive wear was dominant in the early stages of contact. Then, the formation of Fe-based oxides led to tribo-oxidation. According to EDS measurements, the oxide layers were present in both pure and composite coatings, with no significant difference in the composition. The presence of the Cr signal confirmed that these oxides formed at expenses of the 100Cr6 antagonist. The COF evolution stabilised at a higher value for the composite coatings than the pure ones, as represented in Figure 7a. These results were mirrored by the wear rates in Figure 7b and suggested that the SiC particles determined an increase of friction in the system. Comparing the two wear tracks in Figure 8a,b, the SiC particles also acted as the third body in abrasive wear. They determined a rough appearance of the wear track. The SiC agglomerations are exposed by coating wear and can be easily disrupted during the sliding under load, leading to a spread of particles between the coating and the antagonist. In this case, the presence of Fe oxides mitigated the abrasive action of the ceramic particles, without fully compensating it. The steady-state COF values did not align with the results from Aslanyan et al. [21] that obtained similar COF trends for both Ni–P and Ni–P/SiC coatings in a system with corundum (Al₂O₃) as the antagonist. Nevertheless, the difference between these results can be expected, given the significant role of the antagonist. Similar observations hold for the work by Aghaie et al. [29], that tested as-plated Ni–P/SiC against copper (Cu). The authors reported a COF in the 0.5–0.7 range for the initial 200 m, with fluctuation peaks, and these values align with the present study despite the different wear system. They also observed the pull-out of SiC particles from the matrix as wear proceeded, and those particles determined abrasion at expenses of the coating. Chang et al. [19] compared Ni–P and Ni–P/SiC coatings against zirconium oxide (ZrO₂), observing a higher volume loss for the composite coating than the pure one, as well as a higher COF. These results are comparable with what reported in the present study with a different wear system. In summary, different coupling systems can lead to different wear mechanisms, and in the present study the formation of Fe oxides coming from the antagonist influenced the response of coatings to wear.

4.2. Heat-Treated Coatings

The hardness values in Figure 6 support the hypothesis that crystallisation and precipitation happened at a lower temperature in Ni–P/SiC coating than Ni–P one. Since all the tested samples had similar composition (similar P and SiC wt.%), the hardness of the coatings in Figure 6 was related to the different heat treatments. At 400 °C, after reaching the maximum hardness, grain growth started, and so hardness was reduced. Hence, SiC particles did not influence the grain boundaries migration in this case.

The wear mechanisms consisted of abrasion and tribo-oxidation for the heat-treated coatings, similarly to the as-plated coatings. The presence of SiC particles determined a slight difference in the COF evolution for the HT300 samples (Figure 9a). At the same time, it did not influence the COF values for HT360 (Figure 9b) and HT400 (Figure 9c) samples. Nevertheless, the composite coatings presented noisier curves because of the presence of reinforcing particles acting as third body once exposed and pulled-out from the matrix.

For what concerns wear rates, it is necessary to distinguish the samples with wear tracks that reached the substrate (solid circles in Figure 9d) from the ones that presented a mixed surface (empty circles in Figure 9d).

The wear tracks of HT300 pure coatings showed the substrate presented a wear rate of $\sim 3.5 \times 10^{-6} \text{ mm}^3/\text{Nm}$. Micro-plough traces were evident on the surfaces, and due to the fragmentation of coating during sliding (Figure 10a). The lubricant role of Fe oxides did not compensate for the abrasive action of such fragments on the substrate. In the cases with substrate exposed, the thickness of the coating was ~ 26 and $\sim 34 \text{ }\mu\text{m}$, respectively. These values were estimated from the dimension of the annular section of the coating that characterised the wear track. The sample that presented a mixed surface also presented a slightly lower P than the other samples. For the HT300 composite coatings, the wear track presented a mixed surface, with the simultaneous presence of substrate, Fe oxides, and residual coating in the centre (Figure 10b). The higher hardness of composites (Figure 6) and SiC particles' presence as the third body was mitigated by the Fe oxides. The one sample that showed the substrate had a thickness of $\sim 27 \text{ }\mu\text{m}$. The substrate surface was smooth and regular, resulting from a homogeneous abrasion due to the action of SiC particles. It was also the sample that showed the higher content of P with respect to the other ones. These observations align well with the COF trends of Figure 9a since the presence of Fe oxides did not prevent micro-ploughing mechanisms in pure coatings but showed a beneficial effect for the composite coatings. Kong et al. [30] also reported similar COF values for electroless Ni-P coatings treated at $300 \text{ }^\circ\text{C}$ and observed abrasive wear mechanisms, although the antagonist material was not stated.

Moving to the pure coatings after HT360 treatment, the substrate emerged in the wear track for two samples, and the wear rate values are in the 4.5×10^{-6} – $5.8 \times 10^{-6} \text{ mm}^3/\text{Nm}$ range. The centre of wear tracks appeared uniform and regular (Figure 10c), thanks to the Fe oxide's presence that mitigated the damaging effect of coating fragments. In these cases, the coating thickness was estimated at ~ 35 and $\sim 48 \text{ }\mu\text{m}$. One sample presented a mixed surface. In composite coatings, all samples presented a mixed surface on the wear track, with the co-presence of residual coating and Fe oxides. In all these cases, the wear rate was $\sim 10^{-5} \text{ mm}^3/\text{Nm}$, higher than the average value obtained for the pure ones. These results accord well with the hardness values, significantly higher for the Ni-P/SiC coating than the pure ones after the HT360 treatment (Figure 6). Nevertheless, these results are not mirrored by the COF trends in Figure 9b, comparable for both pure and composite coatings. Kong et al. [30] investigated electroless Ni-P coatings and in particular the influence of the heat-treatment on the wear response. They reported that the coatings treated at $350 \text{ }^\circ\text{C}$ present the maximum hardness of $\sim 6100 \text{ MPa}$. The friction coefficient is 0.8. This is also the condition that determines the change from abrasive wear, for temperatures below $350 \text{ }^\circ\text{C}$, to adhesive wear for temperatures higher than $350 \text{ }^\circ\text{C}$.

The results for the HT400 treated samples were different. The Ni-P coatings presented a mixed surface on the wear track in all cases, as depicted in Figure 10e. The wear rate values are lower than $\sim 10^{-5} \text{ mm}^3/\text{Nm}$, and values in the same range were found for the composite coatings, as represented in Figure 10f. One sample presented the substrate, and the estimated thickness was $\sim 38 \text{ }\mu\text{m}$. The appearance is comparable with the other samples that reached the substrate because similar Fe oxides originated from the antagonist. The mechanism is still abrasive, and this result differs from what reported by Kong et al. [30] on electroless Ni-P treated at $400 \text{ }^\circ\text{C}$. Prabu Ram et al. [17] also tested electroless Ni-P after heat treatment performed at $400 \text{ }^\circ\text{C}$ against AISI 440C steel. They observed the formation of an iron oxide layer that adheres on the coatings and has a strong influence on the wear mechanism. Delamination of the coating was not observed, and these results are in line with the present study. The wear system is different, but the similarities are due to the nature of the Fe-based antagonist materials. The overlapping of wear rate values for the two conditions mirrors the COF trends in Figure 9c and the similar hardness values measured for the HT400 samples (Figure 6). The presented results for the HT400 treatment agree with Aslanyan et al. [21] despite the different coupling system. They reported similar COF trends

for both pure and Ni–P/SiC coatings after 1 h at 420 °C. Using corundum as the antagonist, the authors reported a wear volume loss higher for the composite coatings than the pure ones. They attributed it to the pull out of SiC particles during wear, that contributed to the abrasion of the material. The same observations apply to the non-abrasive coupling of the present study with 100Cr6 steel. On the other hand, Chang et al. [19] reported different results with zirconium oxide as antagonist. After the heat treatment carried out at 400 °C for 1 h, the pure coating presented a higher volume loss than the composite one. Similarly, the average COF was slightly higher for the Ni–P coating. The authors attributed these results to the formation of Ni₅Si₂ during heat treatment, that increases ductility due to the small angle phase boundary. A similar behaviour was not observed with the samples of the present study.

The presence of reinforcing particles did not alter the COF values for HT360 and HT400 conditions; however, it affected the wear rate, particularly for the HT360 samples. It is critical to underline that the influence of heat treatment is determined by the P content within the high-P family. Ahmadkhaniha et al. [23] recently clarified that small variations in the P content, within 10 wt.%–16 wt.%, led to different mechanical properties after heat treatment. Thus, the P content is the dominant variable, yet it cannot be controlled during the production process, either electrodeposited or electroless. Nevertheless, the samples of the present study are of interest because they represent the real condition in production systems, with P content in the 10 wt.%–16 wt.% range. The difficulties in optimising specific heat treatments stem from the variation of composition obtained in real production.

5. Conclusions

The present work investigated the wear behaviour of Ni–P and Ni–P/SiC coatings in the as-plated condition and after different heat treatments. The antagonist was a 100Cr6 steel, representative of non-abrasive systems. The interest of the present study was the representation of the real industrial production of Ni–P coatings and the related variations in P content. The aim of the present work was to differentiate the contributions of SiC addition and heat treatment on the wear properties of Ni–P coatings, to find the optimum condition that minimizes the wear rate.

The presence of SiC particles significantly influenced the COF and the wear rate of the as-plated coatings, despite the limited influence in increasing hardness. The presence of Fe oxides, originated in the tribo-oxidation wear mechanisms on the antagonist side, did not completely mitigate the ceramic particles' abrasive action in the composite coatings. These presented higher COF and wear rate than the pure ones.

After heat treatment, the maximum hardness of pure coatings was after 1 h at 400 °C (HT400), while the maximum hardness of composite coatings was after 2 h at 360 °C (HT360). During wear tests, the COF trends reported a difference between pure and composite coatings only in the HT300 condition (300 °C for 2 h). In other cases, the COF stabilised at similar values. The wear mechanisms involved were mainly abrasion and tribo-oxidation, with the formation of lubricant Fe oxides at expenses of the antagonist steel. Micro-plough also occurred for the pure HT300 samples, and Fe oxides combined with SiC particles mitigated it in the composite coating. The COF trends were not mirrored by hardness and wear rates in the HT360 condition, that shown distinct values.

Author Contributions: Conceptualisation, C.Z. and M.M.; methodology, C.Z., D.A., L.L., and A.F.; resources, C.Z. and M.M.; data curation, D.A., L.L., and F.B.; writing—original draft preparation, D.A., L.L., and F.B.; writing—review and editing, A.F., C.Z., and M.M.; supervision, C.Z. and M.M. All authors have read and agreed to the published version of the manuscript.

Funding: This research received no external funding.

Institutional Review Board Statement: Not applicable.

Informed Consent Statement: Not applicable.

Data Availability Statement: The data presented in this study are available on reasonable request from the corresponding author. The data are not publicly available due to privacy.

Acknowledgments: No acknowledgements are needed.

Conflicts of Interest: The authors declare no conflict of interest.

References

- Sahoo, P.; Das, S.K. Tribology of electroless nickel coatings—A review. *Mater. Des.* **2011**, *32*, 1760–1775. [\[CrossRef\]](#)
- Agarwala, R.C.; Agarwala, V. Electroless alloy/composite coatings: A review. *Front. Mater. Sci.* **2005**, *28*, 475–493. [\[CrossRef\]](#)
- Lelevic, A.; Walsh, F.C. Electrodeposition of Ni–P alloy coatings: A review. *Surf. Coat. Technol.* **2019**, *369*, 198–220. [\[CrossRef\]](#)
- Mahidashti, Z.; Aliofkhaezrai, M.; Lotfi, N. Review of nickel-based electrodeposited tribo-coatings. *Trans. Indian Inst. Met.* **2018**, *71*, 257–295. [\[CrossRef\]](#)
- ASTM B733-15 Standard Specification for Autocatalytic (Electroless) Nickel-Phosphorus Coatings on Metal*; ASTM International: West Conshohocken, PA, USA, 2015.
- Buchtik, M.; Kosár, P.; Wasserbauer, J.; Tkacz, J.; Doležal, P. Characterization of electroless Ni–P coating prepared on a wrought ZE10 magnesium alloy. *Coatings* **2018**, *8*, 96. [\[CrossRef\]](#)
- Berkh, O.; Zahavi, J. Electrodeposition and properties of NiP alloys and their composites—A literature survey. *Corros. Rev.* **1996**, *14*, 323–341. [\[CrossRef\]](#)
- Biswas, A.; Das, S.K.; Sahoo, P. A comparative study in microstructural and tribological aspects of phosphorus enriched electroless Ni–P and Ni–P–Cu coating. *Mater. Today Proc.* **2019**, 1–6. [\[CrossRef\]](#)
- Zanella, C.; Lekka, M.; Bonora, P.L. Influence of the particle size on the mechanical and electrochemical behaviour of micro- and nano-nickel matrix composite coatings. *J. Appl. Electrochem.* **2009**, *39*, 31–38. [\[CrossRef\]](#)
- Ahmadkhaniha, D.; Zanella, C. The effects of additives, particles load and current density on codeposition of SiC particles in NiP nanocomposite coatings. *Coatings* **2019**, *9*, 554. [\[CrossRef\]](#)
- Gao, J.; Liu, L.; Wu, Y.; Shen, B.; Hu, W. Electroless Ni–P–SiC composite coatings with superfine particles. *Surf. Coat. Technol.* **2006**, *200*, 5836–5842. [\[CrossRef\]](#)
- Sarret, M.; Müller, C.; Amell, A. Electroless NiP micro- and nano-composite coatings. *Surf. Coat. Technol.* **2006**, *201*, 389–395. [\[CrossRef\]](#)
- Metzger, M.; Ott, R.; Pappé, G.; Schmidt, H. Articles Having Electroless Metal Coatings Incorporating Wear-Resisting Particles Therein. U.S. Patent 3,753,667A, 21 August 1973.
- Sliem, M.H.; Shahzad, K.; Sivaprasad, V.N.; Shakoor, R.A.; Abdullah, A.M.; Fayyaz, O.; Kahraman, R.; Umer, M.A. Enhanced mechanical and corrosion protection properties of pulse electrodeposited NiP–ZrO₂ nanocomposite coatings. *Surf. Coat. Technol.* **2020**, *403*, 126340. [\[CrossRef\]](#)
- Tamilarasan, T.R.; Rajendran, R.; Siva shankar, M.; Sanjith, U.; Rajagopal, G.; Sudagar, J. Wear and scratch behaviour of electroless Ni–P–nano-TiO₂: Effect of surfactants. *Wear* **2016**, *346–347*, 148–157. [\[CrossRef\]](#)
- Karthikeyan, S.; Vijayaraghavan, L.; Madhavan, S.; Almeida, A. Study on the mechanical properties of heat-treated electroless NiP coatings reinforced with Al₂O₃ nano particles. *Metall. Mater. Trans. A Phys. Metall. Mater. Sci.* **2016**, *47*, 2223–2231. [\[CrossRef\]](#)
- Prabu Ram, G.; Karthikeyan, S.; Emmanuel Nicholas, P.; Sathya Sofia, A. Dry sliding wear behavior of electroless NiP and NiP–Al₂O₃ composite coatings. *Mater. Today Proc.* **2020**. [\[CrossRef\]](#)
- De Hazan, Y.; Zimmermann, D.; Z'Graggen, M.; Roos, S.; Aneziris, C.; Bollier, H.; Fehr, P.; Graule, T. Homogeneous electroless Ni–P/SiO₂ nanocomposite coatings with improved wear resistance and modified wear behavior. *Surf. Coat. Technol.* **2010**, *204*, 3464–3470. [\[CrossRef\]](#)
- Chang, C.S.; Hou, K.H.; Ger, M.-D.; Chung, C.K.; Lin, J.F. Effects of annealing temperature on microstructure, surface roughness, mechanical and tribological properties of Ni- and Ni–P/SiC films. *Surf. Coat. Technol.* **2016**, *288*, 135–143. [\[CrossRef\]](#)
- Apachitei, I.; Tichelaar, F.D.; Duszczuk, J.; Katgerman, L. The effect of heat treatment on the structure and abrasive wear resistance of autocatalytic NiP and NiP–SiC coatings. *Surf. Coat. Technol.* **2002**, *149*, 263–278. [\[CrossRef\]](#)
- Aslanyan, I.R.; Bonino, J.P.; Celis, J.P. Effect of reinforcing submicron SiC particles on the wear of electrolytic NiP coatings: Part 1. Uni-directional sliding. *Surf. Coat. Technol.* **2006**, *200*, 2909–2916. [\[CrossRef\]](#)
- UNI EN ISO 683-4:2018 Heat-Treatable Steels, Alloy Steels and Free-Cutting Steels—Part 4: Free-Cutting Steels*; UNI: Milano, Italy, 2018.
- Ahmadkhaniha, D.; Eriksson, F.; Zanella, C. Optimizing heat treatment for electroplated NiP and NiP/SiC coatings. *Coatings* **2020**, *10*, 1179. [\[CrossRef\]](#)
- EN ISO 683-17 Heat-Treated Steels, Alloy Steels and Free-Cutting Steels—Part 17: Ball and Roller Bearing Steels*; ISO: Geneva, Switzerland, 2015.
- Ahmadkhaniha, D.; Eriksson, F.; Leisner, P.; Zanella, C. Effect of SiC particle size and heat-treatment on microhardness and corrosion resistance of NiP electrodeposited coatings. *J. Alloys Compd.* **2018**, *769*, 1080–1087. [\[CrossRef\]](#)
- Pavlatou, E.A.; Stroumbouli, M.; Gyftou, P.; Spyrellis, N. Hardening effect induced by incorporation of SiC particles in nickel electrodeposits. *J. Appl. Electrochem.* **2006**, *36*, 385–394. [\[CrossRef\]](#)
- Zoikis-Karathanasis, A.; Pavlatou, E.A.; Spyrellis, N. Pulse electrodeposition of Ni–P matrix composite coatings reinforced by SiC particles. *J. Alloys Compd.* **2010**, *494*, 396–403. [\[CrossRef\]](#)

28. Hansal, W.E.G.; Sandulache, G.; Mann, R.; Leisner, P. Pulse-electrodeposited NiP–SiC composite coatings. *Electrochim. Acta.* **2013**, *114*, 851–858. [[CrossRef](#)]
29. Aghaie, E.; Najafi, A.; Maleki-Ghaleh, H.; Mohebi, H. Effect of SiC concentration in electrolyte on Ni–SiC composite coating properties. *Surf. Eng.* **2013**, *29*, 177–182. [[CrossRef](#)]
30. Kong, D.; Wang, J.; Fu, G.; Liu, H. Friction and wear performances of Ni–P coatings by chemical plating after crystallization treatment. *Rare Metal Mater. Eng.* **2015**, *44*, 1314–1319.

Article

Microcracks Reduction in Laser Hardened Layers of Ductile Iron

Eduardo Hurtado-Delgado ^{*}, Lizbeth Huerta-Larumbe , Argelia Miranda-Pérez  and Álvaro Aguirre-Sánchez 

Corporación Mexicana de Investigación en Materiales, COMIMSA, Ciencia y Tecnología 790, Saltillo 25290, Coahuila, Mexico; lahuertal1990@gmail.com (L.H.-L.); argelia.miranda@comimsa.com (A.M.-P.); alvarois@hotmail.com (Á.A.-S.)

* Correspondence: eduardoehd@alitmac.com; Tel.: +52-844-411-3200

Abstract: A study of surface hardening of Ductile Iron (DI) with and without austempering heat treatment was developed. The chemical composition of the material contains alloying elements such as Cu and Ni, that allow to obtain a Ductile Iron Grade 120-90-02, based on ASTM A536, which was heat treated to be transformed to Austempered Ductile Iron (ADI). Specimens of $10 \times 10 \times 5 \text{ mm}^3$ were obtained for application of surface hardening by Nd:YAG UR laser of 150 W maximum power. The parameters used were advance speed of 0.2 and 0.3 mm/s and power at 105, 120, 135 and 144 W; the departure microstructures were fully pearlitic in the samples without heat treatment, and ausferrite for austempered samples. Microstructural characterization of hardened samples was performed were analyzed and martensite and undissolved carbides were identified in the pearlitic samples, while in ausferrite samples it was found finer martensite without carbides. The depth of hardened surface to different conditions and their respective microhardness were measured. The results indicate that the surface hardening via laser is a suitable method for improving wear resistance by means of hardness increment in critical areas without compromising the core ductility of DI components, but the surface ductility is enhanced when the DI is austempered before the laser hardening, by the reduction of surface microcracks.

Keywords: laser hardening; ausferrite; austempered ductile iron; nodular iron; heat treatment



Citation: Hurtado-Delgado, E.; Huerta-Larumbe, L.; Miranda-Pérez, A.; Aguirre-Sánchez, Á. Microcracks Reduction in Laser Hardened Layers of Ductile Iron. *Coatings* **2021**, *11*, 368. <https://doi.org/10.3390/coatings11030368>

Academic Editor: Mattia Merlin

Received: 15 February 2021

Accepted: 18 March 2021

Published: 23 March 2021

Publisher's Note: MDPI stays neutral with regard to jurisdictional claims in published maps and institutional affiliations.



Copyright: © 2021 by the authors. Licensee MDPI, Basel, Switzerland. This article is an open access article distributed under the terms and conditions of the Creative Commons Attribution (CC BY) license (<https://creativecommons.org/licenses/by/4.0/>).

1. Introduction

1.1. Characteristics of the Ductile Iron and the Austempered Ductile Iron

Ductile Iron (DI) is commonly used in many engineering applications, like sheet forming dies and rolling mills, as reported in literature [1,2]. Their high manufacturability and machinability represent an excellent combination of economic application performances [1,3,4]. By subjecting the DI to heat treatment, it transforms to Austempered Ductile Iron (ADI), which is essentially a spheroidal graphitic iron with ausferrite microstructure comprising mainly low carbon ferrite (α) and high carbon retained austenite (γ). Because of an excellent combination of strength, ductility, toughness and fatigue resistance [5], ADI is now being increasingly used in key automobile components like crank shafts, steering parts, camshafts and gears [6–8], sometimes substituting steel parts [9].

1.2. Laser Surface Hardened Melting

Despite the good properties of DI and ADI, under some operating conditions such as erosive and corrosive environments its performance is limited by their relative low hardness [10–12]. This problem can be overcome by improving the surface properties of DI. High-power laser treatment (Nd: YAG, CO₂) is found as a significant technique to enhance the mechanical properties of ductile iron according to [13,14], including multi-pass and surface alloying using different powders [15,16], as reported by some authors who proposed some general guidelines for this process. Nevertheless, the presence of microcracks in the hardened case and other surface defects, as reported by [17], constrain

its applicability. Zheng et al. in 2013 proposed a novel technique in order to avoid crack formation in multiple overlapping laser tracks that represent a potential problem that must be reduced as possible [18].

To improve the wear resistance of the ductile iron, laser surface modification, without remelting, has been used in industrial applications, as it prevents failure by propagation of surface cracks [19,20]. In those cases when the iron has a ferrite-pearlite or even only a ferrite matrix, however, it is necessary to use laser hardening by melting the surface layer. This procedure creates a thin, microstructurally modified surface layer with a higher hardness. This layer consists of two parts: a melted zone and a heat hardened zone. The depth and width of the modified layer depend directly on the energy distribution and laser-beam diameter on the workpiece surface, the laser beam speed with respect to the workpiece, and the physical properties of the working material. The temperature and hence the properties of the surface can be controlled by the power density and the scan speed (in case of line hardening) or the interaction time (in case of single-shot hardening) of the beam [21].

Laser surface hardened melting (LSM) offers several advantages over other surface-modification techniques. This process is a non-equilibrium method of surface modification reaching cooling rates around 103–108 K/s, which are considerably high. The resultant microstructures, some of them metastable phases, are mainly composed of unique properties that are only obtained with this process and not with conventional ones [22,23]. Laser hardening is usually constrained to low heat inputs in order to avoid surface microcracks in ductile irons, resulting in shallow hardened layers [24].

1.3. Microstructure and Typical Hardness

During laser hardening process, the surface of the irradiated material is heated in order to transform the microstructure of the heat affected zone into austenite. The surrounding material acts as an efficient heat sink, quickly cooling the material likely below the martensite start temperature [19].

The present microstructure after treatment LSM depends on the parameters used in the process as well as the initial microstructure of the workpiece. In this way, Benyonius [10] reported that if the microstructure in the DI is ferritic, after LSM treatment, eventually it will be formed a microstructure of dendrites made of austenite, surrounded by continuous networks of Fe_3C and some martensite needles within the austenite islands. Alabeedi [23] presented an LSM treatment in a ferritic DI and showed that the laser melting led to complete dissolution of the graphite nodules which on solidifying created an interdendritic network of ledeburite eutectic with a very fine structure, good homogeneity and high hardness (650 HV). In another paper presented by Fernández [2], it was studied the effects of laser surface treatment on the microstructure, crackability and stresses generated on laser hardened layers produced in several ductile cast iron materials; in the study, two principal types of spheroidal graphite were selected. Considerable cracking by thermal stresses was produced on both irons, pearlitic and acicular bainitic, the energy densities achieved was above 40 J/mm^2 . It was observed that lower energy densities refrain cracking but only in the pearlitic ones, this was achieved by the excessive austenite retention that controlled the generation of transformational stresses. Grum [25] reported that in case of having an initial pearlitic matrix in the ductile iron, after a laser surface hardening, the resultant and predominant structure produced in the surface is martensite.

Regarding ADI that presents ausferrite microstructure initially, Roy [26] observed that the structure of the laser surface melted area was mainly austenitic, while a higher microhardness of more than 1000 HV happened with a martensitic microstructure. Furthermore, LSM produced more compressive residual stresses and enhanced significantly the wear resistance of the austempered ductile iron [19]. Putatunda [27], who applied laser hardening techniques, carried out an investigation on ADI. They used manganese phosphate coatings and colloidal graphite to achieve more uniform hardness. The hardness

values reached were around 700 HV and the microstructure of a thin hardened martensitic layer improved the mechanical properties of the material.

Amirsadeghi [28] studied the microhardness and wear resistance of different microstructures formed by tungsten inert gas (TIG) surface melting and chromium surface alloying (using ferrochromium) of ADI. Surface melting resulted in the formation of a ledeburitic structure in the melted zone, and this structure has hardness up to 896 HV, as compared to 360 HV in that of ADI. The results also indicated that surface melting reduced the wear rate of the ADI by approximately 37%. Finally, in a work presented by Grum [25], it was studied the laser surface-melt hardening in gray and nodular irons, and found that the melting produced by low-power laser beam can obtain an adequately modified hardened layer, which results in an increment of the surface wear resistance. Material properties play a dominant role in determining the interaction between the laser beams and engineering materials. Many material properties change with temperature. The mechanical properties of many engineering materials may be favorably modified by application of a suitable heat treatment, which can be full or superficial [29]. One of the most important superficial treatments of metals has been the laser transformation hardening of steel [29,30], but this treatment can also be applied successfully to ductile irons.

In the present study, an attempt has been made to enhance surface hardness and wear resistance of DI with and without austempering heat treatment. The aim of this work is to show that the austempered heat treatment before laser hardening of ductile iron is effective in reducing the amount of surface microcracks in a wide range of heat inputs.

2. Materials and Methods

2.1. Ductile Iron

The nodular iron utilized for these experiments corresponds to 120-90-02 grade, under the ASTM A536 [31] standard and it has a chemical composition that is typical for this type of irons. Cu and Ni were added to increase the amount of pearlite in the as-cast microstructure. The chemical composition is shown in Table 1.

Table 1. Chemical composition (wt. %) of the Ductile Iron (DI).

C	Si	Mn	Cu	Mo	Ni	Mg	Cr	P	Fe
3.52	2.11	0.32	0.39	0.21	0.33	0.05	0.15	0.025	Bal.

The carbon equivalent for this ductile iron was of $C_e = 3.82$, which is defined as hypereutectic iron. Besides this, eutectic saturation was calculated as $S_c = 1.05$ considering Si, Mn and P, according to the equation presented in [32].

2.2. Austempered Ductile Iron

The DI samples were fully austenitized at 900 °C for 120 min and austempered in an isothermal salt bath at 340 °C to 360 °C for 60 min followed by cooling in air at room temperature. The salt bath was 60% KNO₃ and 40% NaNO₂ a schematic diagram of the austempering heat treatment process is shown in Figure 1.

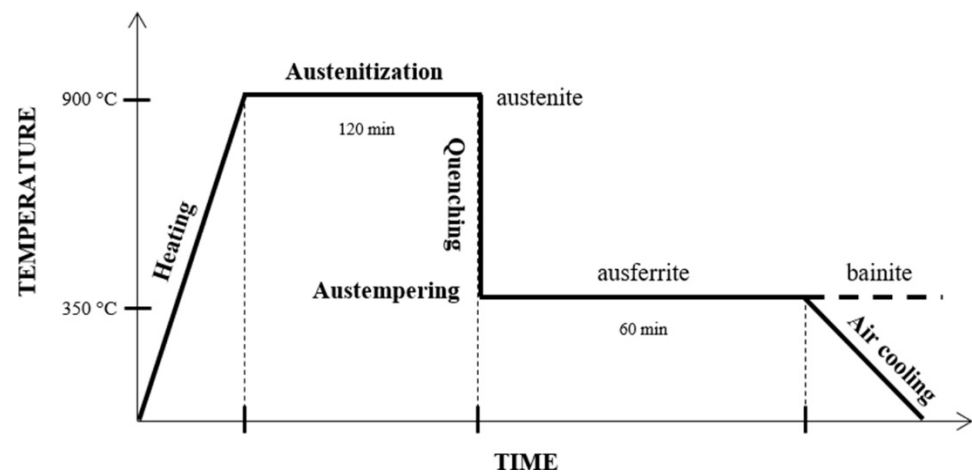


Figure 1. Schematic heat treatment process.

2.3. Experiment Design and Laser Parameters

In this study, DI samples with and without austempering heat treatment were surface hardened by UR LaserTechnologie Nd:YAG laser of 150 W maximum power. Diameter of laser spot was about a half of the bead width, which can be observed as the length of the transversal fusion zone near the surface. It is difficult to assign a defined value because there is a power density reduction from the center to the periphery, following a Gaussian function. However, the effective spot size, in this case can be considered as that which produces the fusion of the metal in the axial direction; it is approximately the full length of the fusion zone at the half depth, shown in the micrographs in results section. The specimen dimensions were $10 \times 10 \times 5$ mm. The selected parameters for the surface treatment were the following:

- Two advance speeds: 0.2 and 0.3 mm/s
- Four powers: P1 = 144 W, P2 = 135 W, P3 = 120 W, P4 = 105 W

Four samples were used for the experiment: two DI and two ADI samples. For each sample, four laser-melted beads were produced, one for each power level, according to the Figure 2 schemes.

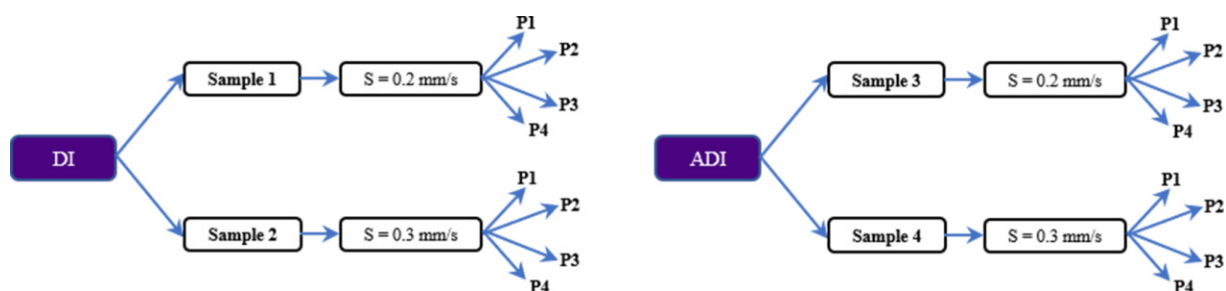


Figure 2. Design of experiments for the laser surface hardening.

2.4. Laser Surface Melting-Hardening of DI and ADI

Cross sections of the samples were cut for metallographic examination. The microstructural characterization was consisted in grinding (using 120, 240, 320, 600, 800 SiC paper) and polishing with a one μm diamond paste, using Nital at 1% as reactive etchant for 5 s. The samples were inspected in the different seams weld zones with an optical microscope (OM) Nikon Eclipse MA200 and electron microscope Tescan Mira 3; besides this, hardness examinations in each zone were performed using 300 g for Vickers indentation. Microhardness evaluation, using a Wilson hardness Tukon 2500 equipment, was performed in order to compare the parameters effect in the weld beads and to find a proper

combination with the higher hardness without cracks. Wear resistance is favored with these characteristics [33]. Figure 3 shows each zone area where RZ and HZ correspond to the re-melted zone and hardened zone (affected by the heat), respectively. All the indentations for microhardness profile are shown as well: 3 indentations for each position (H1, H2, H3, H4) in order to obtain the average and more reliable results.

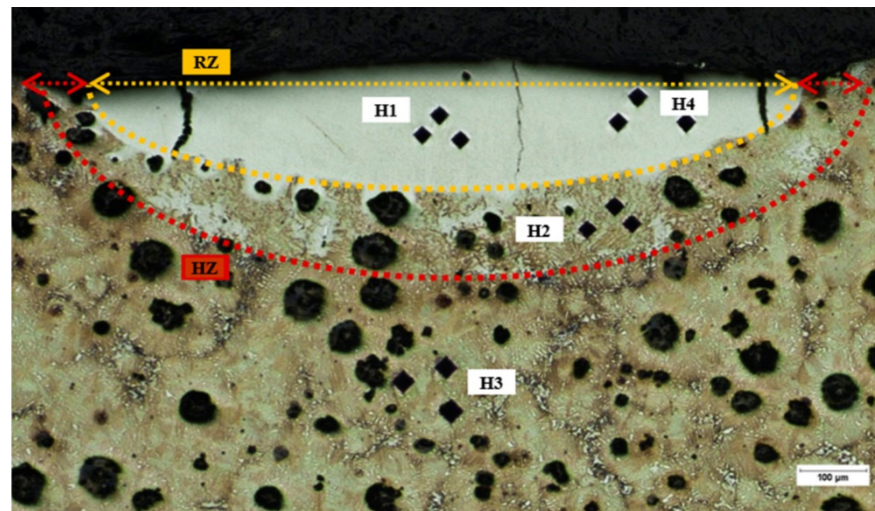


Figure 3. Current zones in the weld seam of the laser surface hardened melting (LSM).

3. Results and Discussion

3.1. Base Material

The original microstructures for DI samples before the surface hardening are shown in Figure 4. Microstructure consist mainly of pearlite and graphite nodules, around 30 µm diameter, with a composition of 84% and 12%, respectively, and the difference may indicate segregation zones predominantly Ni and Cr (Figure 4a). The microstructure was measured by image analysis with Image Pro Software and NIS Element coupled to the OM; for the ADI samples (Figure 4b), it was present ausferrite, graphite nodules and austenite islands, and the segregated zones disappeared with the austempering. The compositions of these phases were 83%, 11% and 6%, respectively, measured by image analysis.

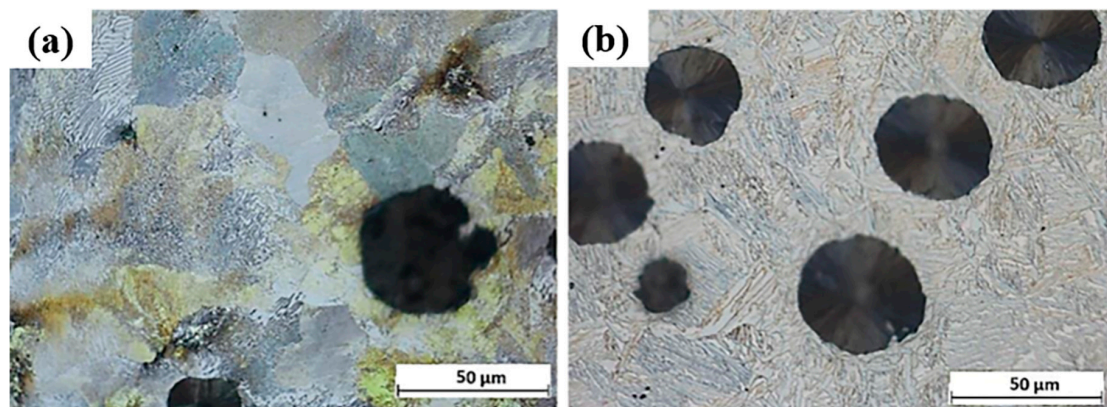


Figure 4. Optical micrograph, (a) DI (Pearlite + Nodules + Segregations), (b) Austempered Ductile Iron (ADI; Ausferrite + Nodules + Austenite).

On average hardness in the DI was 295 HB and heat treatment increased the ADI to 314 HB.

3.2. Dimensions and Morphology of the Melted Zone

As the iron castings are a mixture of phases of iron and graphite, when the metal is re-melted by the laser it dissolves all the free graphite in the liquid and in the subsequent and fast cooling it results in an oversaturated carbon alloy, mainly formed by martensite, some retained austenite and iron carbides. The proportion of these phases depends upon the maximum temperature reached, the holding time at this temperature and the cooling rate. The first variable depends on the laser power, and the last two variables depend on the advanced speed of the laser beam and the thermal metal properties.

The DI can be hardened by a laser beam because of the great amount of carbon contained in the microstructure which can be dissolved and form martensite after the fast fusion of the metal, taking advantage of the high-density power of the laser beam [34]. This can be realized using even a low power equipment, of only 150 W, like that used in this study. In Figure 5 shows the morphology of the left half beads produced with the laser at its highest power, 144 W and their dimensions. DI beads are wider and deeper than their corresponding ADI seams with slower speed. They also have more and larger surface cracks. DI cracks are observed as larger as the hardened layer, as in S1P1 where its value corresponds to 371 μm , crossing thoroughly the melted zone. Cracks in the hardened iron are in the diagonal and vertical direction. As reported for surface alloyed carbon steels [35,36], the presence of cracks is due to hot cracking. Since susceptibility for hot cracking is determined by the alloy plasticity and solidification temperature range (ΔT); in the surface area, a composition near the eutectic point (3.4–4.5 C wt.%) is expected, so ΔT is small, resulting in some plasticity and fine dendritic structure at laser temperatures. Therefore, once the metal is partially solid, crack appearance depends on the thermal contraction of the remaining molten metal.

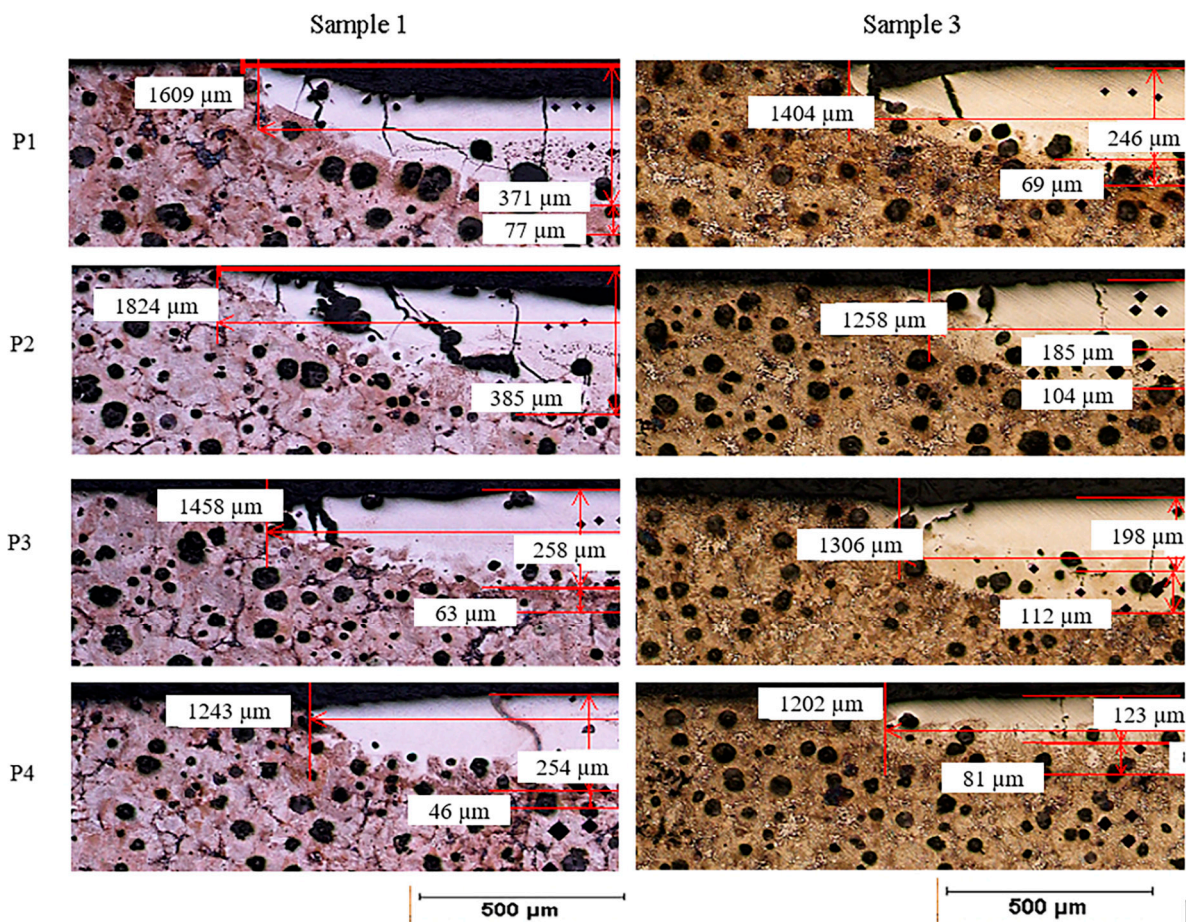


Figure 5. Seams dimensions of DI: Sample 1 (S1) and ADI: Sample 3 (S3), with 0.2 mm/s speed.

If the advance speed of the laser source is changed from 0.2 mm/s to 0.3 mm/s, DI beads are wider than their corresponding ADI beads, in all cases, but not necessarily deeper; this can be observed in Figure 6, where the depth of ADI increases except for the highest power. Moreover, due to their greater depths of melted zone, 0.2 mm/s speed presented greater nodule dissolution.

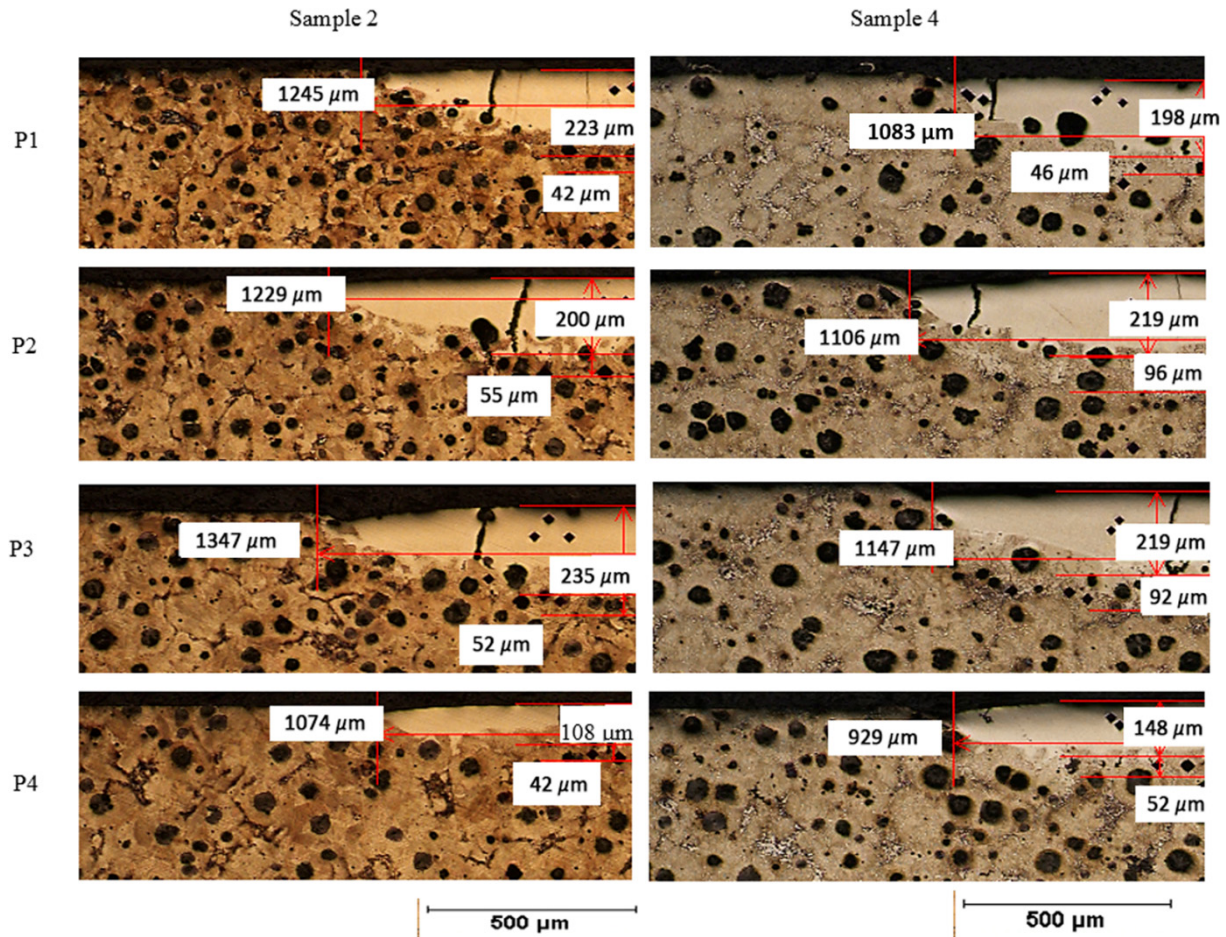


Figure 6. Beads dimensions of DI: Sample 2 (S2) and ADI: Sample 4 (S4), with 0.3 mm/s speed.

The results shown in Tables 2 and 3 indicate that the power input density was between 325 J/mm² and 579 J/mm² for speed of 0.2 mm/s; furthermore, the power density was between 248 J/mm² and 385 J/mm² for 0.3 mm/s. This outcome is far from the power density of 40 J/mm², reported by [2]. Nevertheless, there is no evidence of crack appearance at the lowest power used in the experiments of this work, so the later reference value is likely conservative.

Table 2. Bead measures in different samples (0.2 mm/s speed).

	S1_P1	S1_P2	S1_P3	S1_P4	S3_P1	S3_P2	S3_P3	S3_P4
Width (μm)	1609	1824	1458	1243	1404	1258	1306	1202
Depth melting (μm)	371	385	258	254	246	185	198	123
Thickness HAZ (μm)	77	>10	63	46	69	104	112	81

Table 3. Bead measures in different zones (0.3 mm/s speed).

	S2_P1	S2_P2	S2_P3	S2_P4	S4_P1	S4_P2	S4_P3	S4_P4
Width (μm)	1245	1229	1347	1074	1083	1106	1147	929
Depth melting (μm)	223	200	235	108	198	219	219	148
Thickness HAZ (μm)	42	55	52	42	46	96	92	52

3.3. Microstructure

3.3.1. Base Metal

Figure 7a shows the pearlitic initial microstructure of the DI samples; the pearlite is constituted of Fe_3C lamellae with ferrite, and the hardness value is around 320 HV. In Figure 7b, the ausferritic microstructure that is characteristic of ADI is presented; this structure has a hardness of approximately 410 HV and consists of high carbon austenite plates with ferrite. Ausferrite microstructure refinement is dependent of the austempering temperature. In this case, the ausferrite is not as fine as could be under lower austempering temperatures [37].

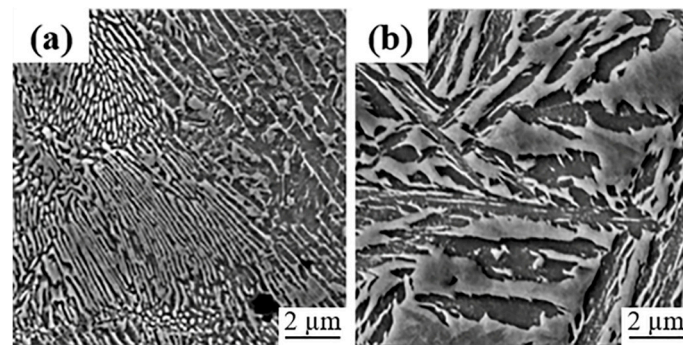


Figure 7. Microstructure, (a) DI: Pearlite, (b) ADI: Ausferrite.

3.3.2. High Power Remelted Zone

On the fusion zone (H1) from DI samples, sample 1 (S1) presented in Figure 8a has a large amount of refined acicular Fe_3C (AFC), high carbon martensite (HCM) at the bottom and some retained austenite (γ_r); for that reason, the reached hardness in this area was >1000 HV. On the other hand, sample 2 (S2) obtained a lower hardness (731 HV). As can be seen, the hardness reduction from S1 to S2 is due to the increase of speed, Fe_3C is present in lower quantities and is coarser (ACC), the presence of HCM increased as well as γ_r , and the carbides decreased and some of them were separated from martensite to be grouped and form a platelike constituent (Figure 8b).

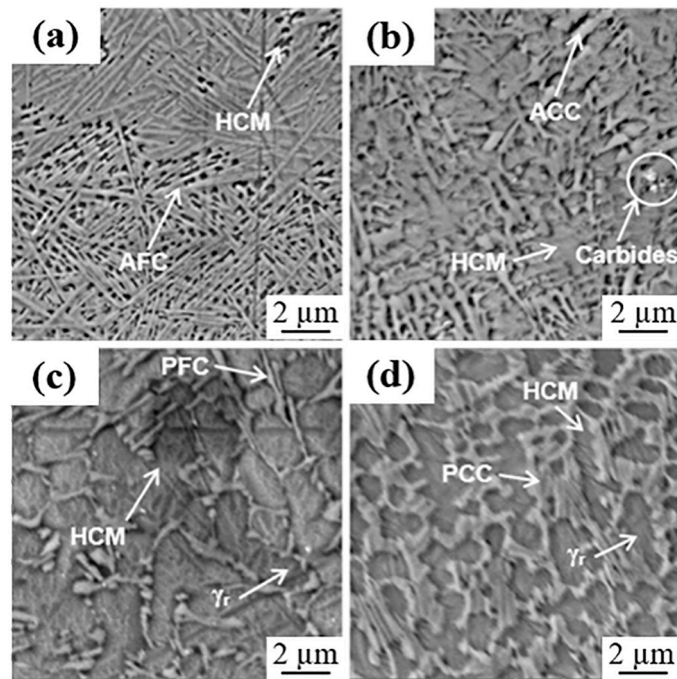


Figure 8. Microstructure of the melting zone (H1) to 150 W (P1), (a) Sample 1, (b) Sample 2, (c) Sample 3 and (d) Sample 4.

Regarding the ADI, the reached temperatures on the fusion zone were lower than those for the DI; for that reason, the dissolved carbon amount was minor. Figure 8c shows the H1 zone microstructure which corresponds to sample 3 (S3); it is constituted of HCM islands surrounded by Fe_3C fine plates (PFC) and small amounts of γ_r , with almost 968 HV. This microstructure was formed due to the lower laser speed and the higher temperature reached; the γ from the sample was not rich in carbon, which prevented its stabilization at room temperature and, from the rapid cooling, the microstructure transformed mostly to HCM [34,38] and the surrounded liquid to Fe_3C .

At higher advance speed, the maximum temperature in the sample is lower and the arising γ dissolves more carbon that stabilizes it at room temperature. Figure 8d exhibits sample 4 (S4), on the H1 zone, and presents large quantities of γ_r in form of islands surrounded by coarser and greater Fe_3C plates (PCC). Some zones, wherein γ could not dissolve too much carbon, transformed into HCM with rapid cooling. The higher amount of γ_r in this sample is the cause of the hardness decay (864 HV) compared to S3.

Using the diagram in Figure 9, the microstructures from different samples were deduced. In this diagram [39] the carbon concentration curves as a function of the cooling and heating rates are presented, as an example. The amount and type of resultant microstructures depend on the maximum temperature reached, as well as the heating and cooling rates, which in turn depend on the power and advance speed of the laser beam. This can be visualized using the Fe-C-Si phase diagram, the heating and cooling cycles superimposed for a high speed-high power, and a low speed-low power beams, both acting upon a surface of nodular iron with a fully pearlitic matrix (i.e., 0.8% C). In the first case, fusion zone, a high temperature is reached very fast, but there is no time to dissolve a great amount of carbon from the graphite spheroids; after the fast heating, a fast cooling is followed and the result is an austenite with low carbon content which is transformed to a mixture of martensite and some γ_r , surrounded by Fe_3C , which arose from the molten metal, as the final microstructure. In the second case (low speed-low power), the reached temperature is lower, but there is more time to dissolve carbon and, according to the Fe-C-Si diagram, carbon has more solubility in austenite at lower temperatures above the eutectic; after heating, the cooling is faster but, because the greater content of carbon, less austenite

transforms to martensite, since M_s (martensite start transformation temperature) is lower, and the austenite is more stable at ambient temperature in this condition. The total amount of molten metal can be greater, at lower speed (and lower T), but the liquid volume fraction is lower because, at lower temperature, more austenite can coexist with the liquid; the carbon dissolution has the effect to lower the liquidus temperature in the Fe-C-Si system. Consequently, the volume fraction of cementite formed at the end is greater when higher advance speed is used, even when the temperature had been lower. It is important to know this, because the number and extension of surface microcracks depend on the amount of martensite and cementite in the microstructure.

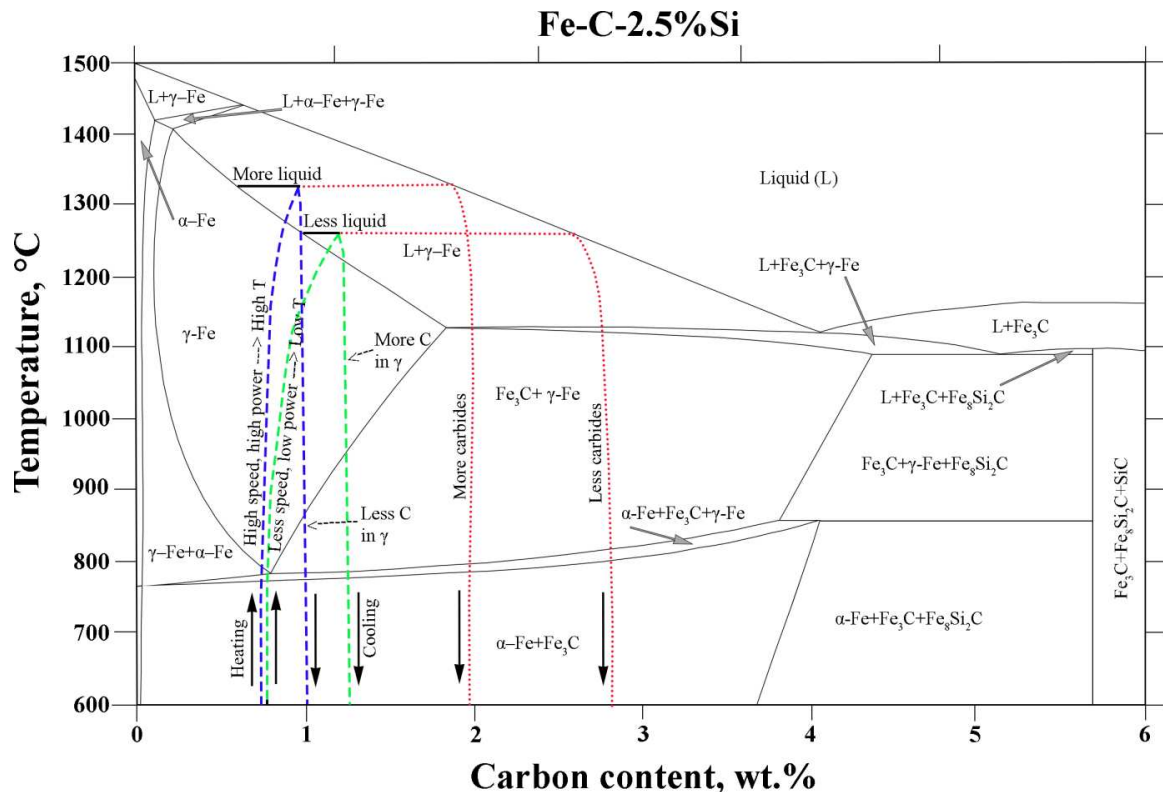


Figure 9. Schematic Fe-C-Si diagram [39].

3.3.3. Low Power Remelted Zone

Due to the low temperature reached on the H1 zone (P4) in S1 sample the microstructure formed (Figure 10a) consisted mostly in γ_r with HCM islands surrounded by PFC; the amount of carbides decreased compared to the P1 power, and for that reason the hardness decay >1000 HV (P1) to 633 HV (P4). In Figure 10b are shown the microstructures obtained in the H1 zone from S2 sample; unlike the previous one, more presence of PFC is evident since the required liquidus temperature in this zone was greater than S1 at the same power, due to the lower carbon dissolution.

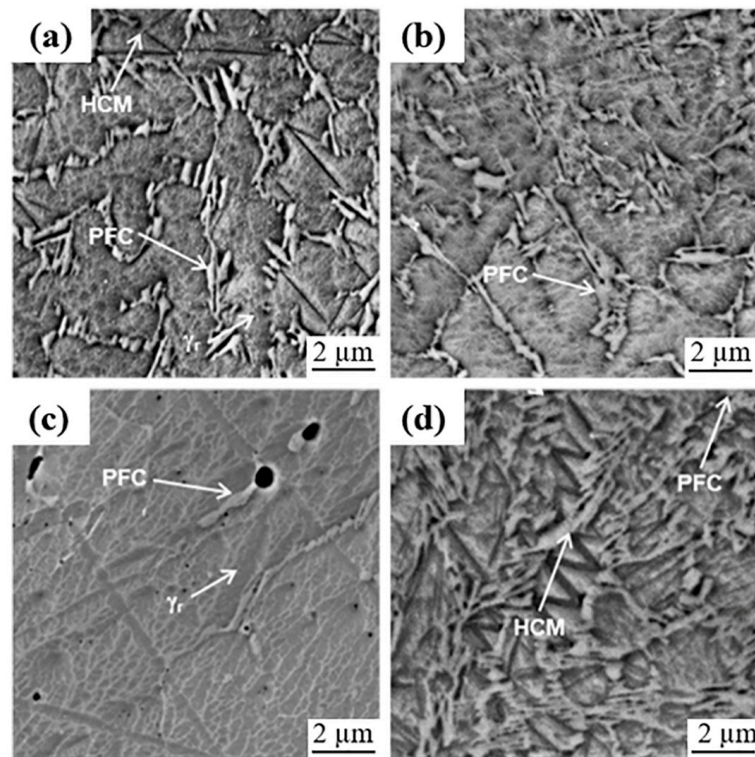


Figure 10. Melting zone (H1) microstructure 70 W (P4), (a) Sample 1, (b) Sample 2, (c) Sample 3, (d) Sample 4.

Instead, for ADI at P4 power with 0.2 mm/s the maximum temperature barely melted the metal; it exceeded the liquidus line but did not get to dissolve a considerable amount of nodules; when cooling begins, the material transforms to austenite with high carbon content and a small quantity of liquid, at certain intermediate temperature this small quantity of liquid transforms to ledeburite and high carbon austenite. A slight amount of Fe_3C that encloses the γ_r grains arises from ledeburite. The sample at higher speed S4_P4 did not reach the liquidus line when it started to cool; the liquid that forms, as well as the austenite, has lower carbon content than the maximum achievable, which corresponds to the eutectic, just at the maximum solubility of austenite; at high cooling rate the liquid rapidly reaches an inferior temperature than the eutectic, starting the cementite formation. Most of the prior austenite, with insufficient carbon to prevail as a metastable phase at low temperature, transforms to martensite.

3.3.4. HAZ

As observed in Figure 11, the heat affected zone is very similar for both materials and both speeds; it consists mainly of martensite and retained austenite as mentioned in [16]. The structure is finer for the DI samples because it reached lower temperature and the carbon homogenization is faster in the pearlitic condition than in the ausferritic.

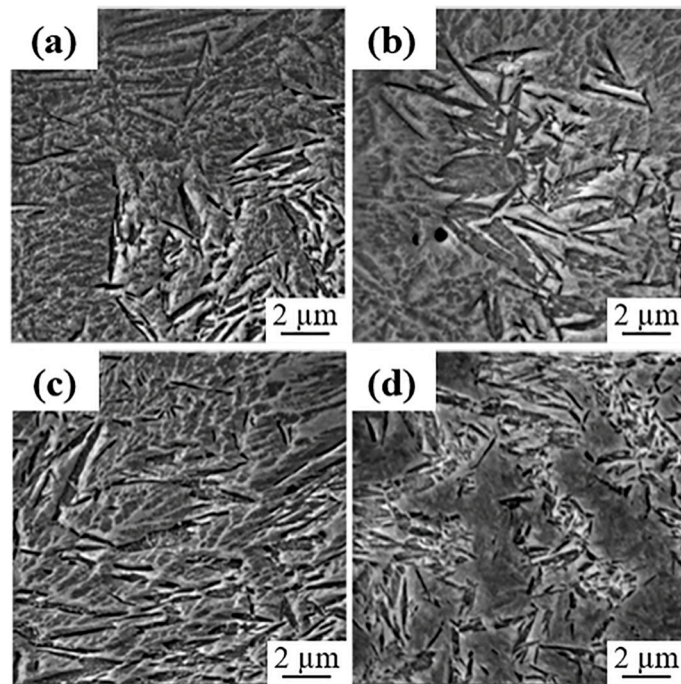


Figure 11. Microstructure of the HAZ (H2) to 70 W (P4), (a) Sample 1, (b) Sample 2, (c) Sample 3, (d) Sample 4.

3.4. Cracks and Microhardness

3.4.1. High Hardness

Table 4 shows microhardness results obtained at different positions of all samples. The beads of DI that presented higher hardness values were those with the lower speed and higher power (P1), this is due to most of the microstructure being Fe_3C in S1_P1; the Fe_3C was in acicular form and martensite in small amounts. For that reason, high hardness was obtained >1000 HV, so that it caused embrittlement at cooling producing a great number of cracks (Figure 5). On the other hand, S2_P1 presented a coarser Fe_3C with larger martensite volume fraction than S1_P1; therefore, the hardness resulted lower (731 HV) and the cracks presence was reduced, hence the sample was less fragile, as pointed out in [2].

Table 4. Microhardness at different positions (HV).

	H1 (HV)	H2 (HV)	H3 (HV)	H4 (HV)
S1_P1	1022	846	335	1055
S1_P2	1145	748	268	1017
S1_P3	872	529	327	673
S1_P4	633	606	363	565
S2_P1	731	397	317	750
S2_P2	695	410	318	563
S2_P3	738	610	314	780
S2_P4	662	571	305	765
S3_P1	968	560	415	908
S3_P2	557	573	424	623
S3_P3	609	561	358	648
S3_P4	542	674	401	565
S4_P1	867	569	308	713
S4_P2	724	647	413	643
S4_P3	898	606	353	939
S4_P4	721	576	394	667

At the same P1 in the ADI samples, S3 achieved hardness values of 968 HV that are close to S1_P1, the crack appearance was abruptly reduced due to the microstructure but graphite flotation was evident on the surface. In S4_P1, the hardness value was 867 HV since γ_r transformation, compared to S3_P1, the cracks were smaller and graphite flotation was removed.

3.4.2. Low Hardness

At lower power and speeds, the hardness decreased significantly from 1022 HV (S1_P1) to 633 HV (S1_P4), and crack presence was eliminated due to the resulted microstructure. At higher speed hardness, decay was not evident for beads P1 to P4, since it passes from 731 HV to 622 HV. In the ADI at lower power a similar behavior was maintained as in DI samples, since hardness decrease was more noticeable at lower speeds (968 HV a 542 HV); this behavior was also reported in [19].

4. Conclusions

The parameters which demonstrate improved performance regarding hardness, dimensions and crack formations were:

- Material = ADI
- Power = P4 (105 W)
- Speed = 0.3 mm/s

Surface hardening by laser treatment is reliable, but cracks are generated during the solidification if not properly applied.

ADI re-melted beads are more narrow than their corresponding DI beads.

The highest hardness was 1145 HV obtained from the DI condition, without austempering heat treatment.

The DI samples presented more and larger cracks in all experimental conditions because the contraction of cementite during cooling.

ADI is less prone to crack formation than DI, because it contains less cementite and more martensite, and because ausferrite is more heat-conductive than pearlite.

Concisely, this work has demonstrated with no doubt that the ADI is a better option for laser hardening than DI, because the former can dissipate the heat input faster and more evenly, due to the thermal characteristics of both materials, identical in chemical composition, but not in phase composition. ADI has a metal conductive matrix with carbon saturated austenite and graphite nodules, while DI has a mixture of metal and ceramic (pearlite) matrix and graphite nodules which is less heat-conductive. Microcracks are related to the excessive accumulation of heat, which produces higher thermal gradients and formation of greater amounts of carbides.

Author Contributions: E.H.-D. conceived and planned all experiments. L.H.-L. and Á.A.-S. performed all experimentations. A.M.-P. and L.H.-L. wrote the manuscript, and all authors participated in results analysis and discussion. All authors have read and agreed to the published version of the manuscript.

Funding: The present work was funded by CONACyT Mexico under the project Proinnova 216536.

Institutional Review Board Statement: Not applicable.

Informed Consent Statement: Not applicable.

Data Availability Statement: Data discussed in this contribution is available on request from the corresponding author.

Conflicts of Interest: The authors declare no conflict of interest.

References

1. Nêmeček, S. Surface of cast iron after laser hardening. *Adv. Mater. Res.* **2013**, *685*, 92–96. [[CrossRef](#)]

2. Fernández, A.; Pellizzari, M.; Arias, J. Feasibility of laser surface treatment of pearlitic and bainitic ductile irons for hot rolls. *J. Mater. Process. Technol.* **2012**, *212*, 989–1002. [[CrossRef](#)]
3. Pagano, N.; Angelini, V.; Ceschini, L.; Campana, G. Laser remelting for enhancing tribological performances of a ductile iron. *Proc. CIRP* **2016**, *41*, 987–991. [[CrossRef](#)]
4. Riposan, I.; Chisamera, A.; Stan, S. Control of surface graphite degeneration in ductile iron for windmill applications. *Am. Found. Soc.* **2013**, *7*, 9–20. [[CrossRef](#)]
5. Polishetty, A.; Singamneni, S.; Littlefair, G. A comparative assessment of austempered ductile iron as a substitute in weight reduction applications. In Proceedings of the International Manufacturing Science and Engineering Conference, Evanston, IL, USA, 7–10 October 2008; pp. 49–57.
6. Rathod, M.; Deore, H. Laser surface hardening of ductile irons. In Proceedings of the International Conference on Automotive Materials & Manufacturing, Pune, India, 28–30 April 2014; pp. 1–5. [[CrossRef](#)]
7. Lefevre, J.; Hayrynen, K. Austempered materials for powertrain applications. *J. Mater. Eng. Perform.* **2013**, *22*, 1914–1922. [[CrossRef](#)]
8. Meena, A.; Mansori, M. Study of dry and minimum quantity lubrication drilling of novel austempered ductile iron (ADI) for automotive applications. *Wear* **2011**, *27*, 2412–2416. [[CrossRef](#)]
9. Harding, R. The production, properties and automotive applications of austempered ductile iron. *Kov. Mater.* **2007**, *45*, 1–16.
10. Benyonius, K.; Fakron, O.; Abboud, J.; Olabi, A.; Hashmi, M. Surface melting of nodular cast iron by Nd-YAG laser and TIG. *J. Mater. Process. Technol.* **2005**, *170*, 127–132. [[CrossRef](#)]
11. Lu, G.-X.; Zhang, H. Sliding wear characteristics of austempered ductile iron with and without laser hardening. *Wear* **1990**, *138*, 1–12.
12. Fischer, S.; Muschna, S.; Bührig-Polaczek, A.; Bünck, M. In-situ surface hardening of cast iron by surface layer metallurgy. *Mater. Sci. Eng. A* **2014**, *615*, 61–69. [[CrossRef](#)]
13. Li, Y.; Liu, J. Experimental Study of Laser Surface Treatment of Low-carbon Ductile Iron. *Appl. Mech. Mater.* **2012**, *155–156*, 965–968. [[CrossRef](#)]
14. López, V.; Bello, J.M.; Ruíz, J.; Fernández, B.J. Surface laser treatment of ductile irons. *J. Mater. Sci.* **1994**, *29*, 4216–4224. [[CrossRef](#)]
15. Wang, H.; Bergmann, H. Rapid Graphitization of a Pulsed Laser Remelted Ductile Cast Iron during Multipass Overlap Melting. *Metall. Mater. Trans. A* **1995**, *26*, 793–800. [[CrossRef](#)]
16. Heydarzadeh, M.; Ebrahimi, M.; Ghasemi, H.; Shahripour, A. Microstructural study of surface melted and chromium surface alloyed ductile iron. *Appl. Surf. Sci.* **2012**, *258*, 7348–7353.
17. Sun, G.; Zhou, R.; Li, P.; Feng, A.; Zhang, Y. Laser surface alloying of C-B-W-Cr powders on nodular cast iron rolls. *Surf. Coat. Technol.* **2011**, *205*, 2747–2754. [[CrossRef](#)]
18. Li, Z.-Y.; Zhao, H.-Y.; Gu, Y.; Zhong, M.-L.; Zhang, B.; Zhang, H.-J.; Liu, W.-J.; Ren, Z.-Y.; Yang, M.-J.; Li, H.-Q. Fatigue crack propagation in laser alloyed ductile cast iron surface. *J. Laser Appl.* **2013**, *25*. [[CrossRef](#)]
19. Soriano, C.; Lamnbarri, J.; García, V.; Leunda, C.S.Y.L. Effect of laser surface hardening on the microstructure, hardness and residual stresses of austempered ductile iron grades. *Appl. Surf. Sci.* **2011**, *257*, 7101–7106. [[CrossRef](#)]
20. Li, D.-Y.; Xu, Z.-Y.; Ma, X.-L.; Shi, D.-Q. Review of current research and application of ductile cast iron quality monitoring technologies in Chinese foundry industry. *China Foundry* **2015**, *12*, 239–250.
21. Deore, H.; Rathod, M.; Hiwarkar, V. Influence of laser surface hardening on microstructure and mechanical properties of austempered ductile iron. In Proceedings of the International Conference on Ideas, Impact and Innovation in Mechanical Engineering (ICIIME 2017), Pune, India, 1–2 June 2017; Volume 5, pp. 1126–1132.
22. da Costa, A.R.; Craievich, A.; Vilar, R. Phase transitions in Nb rich coating produced by laser alloying: A synchrotron radiation diffraction study. *Mater. Sci. Eng.* **2001**, *336*, 215–218. [[CrossRef](#)]
23. Alabeedi, K.; Abboud, J.; Benyonius, K. Microstructure and erosion resistance enhancement of nodular cast iron by laser melting. *Wear* **2009**, *266*, 925–933. [[CrossRef](#)]
24. Chen, Y.; Gan, C.; Wang, L.; Yua, G.; Kaplan, A. Laser surface modified ductile iron by pulsed Nd:YAG laser beam with two-dimensional array distribution. *Appl. Surf. Sci.* **2005**, *245*, 316–321. [[CrossRef](#)]
25. Grum, J.; Sturm, R. Laser surface melt hardening of gray and nodular irons. *Appl. Surf. Sci.* **1997**, *109–110*, 128–132. [[CrossRef](#)]
26. Roy, A.; Manna, I. Laser surface engineering to improve wear resistance of austempered ductile iron. *Mater. Sci. Eng. A* **2001**, *297*, 85–93. [[CrossRef](#)]
27. Putatunda, S.; Bartosiewicz, L.; Hull, R.; Lander, M. Laser Hardening of Austempered Ductile Cast Iron (ADI). *Mater. Manuf. Process.* **1997**, *12*, 137–151. [[CrossRef](#)]
28. Amirsadeghi, A.; Heydarzadeh, M.; Kashani, S. Effects of TIG Surface Melting and Chromium Surface Alloying on Microstructure Hardness and Wear Resistance of ADI. *J. Iron Steel Res. Int.* **2008**, *15*, 86–94. [[CrossRef](#)]
29. Saretta, A.; Goldenstein, H.; Guesser, W.; de Campos, M. Quenching and partitioning heat treatment in ductile cast irons. *Mater. Res.* **2014**, *17*, 115–1123.
30. Visscher, H.; de Rooij, M.; Vroegop, P.; Schipper, D. The influence of laser line hardening of carbon steel AISI 1045 on the lubricated wear against steel AISI 52100. *Wear* **1995**, *181–183*, 638–647. [[CrossRef](#)]
31. ASTM A536-84(2019). *Standard Specification for Ductile Iron Castings*; ASTM International: West Conshohocken, PA, USA, 2019.

32. Gumienny, G.; Kurowska, B. Analysis of the graphite shape in cast iron obtaining by in mold process. *Arch. Foundry Eng.* **2015**, *15*, 15–20.
33. Medynski, D.; Janus, A.; Samociuk, B.; Checmanowski, J. Effect of Microstructures on Working Properties of Nickel-Manganese-Copper Cast Iron. *Metals* **2018**, *8*, 341. [[CrossRef](#)]
34. Mahmoud, A.; Mohamed, M. Laser surface hardening of ductile cast iron. *Mach. Technol. Mater.* **2013**, *12*, 8–11.
35. Li, S.; Hu, Q.-W.; Zeng, X.-Y.; Ji, S.-Q. Effect of carbon content on the microstructure and the cracking susceptibility of Fe-based laser-clad layer. *Appl. Surf. Sci.* **2005**, *240*, 63–70. [[CrossRef](#)]
36. Wulin, S.; Beidi, Z.; Changsheng, X.; Wei, H.; Krun, C. Cracking susceptibility of a laser-clad layer as related to the melting properties of the cladding alloy. *Surf. Coat. Technol.* **1999**, *115*, 270–272. [[CrossRef](#)]
37. Pérez, M.; Cisneros, M.; López, H. Wear resistance of Cu–Ni–Mo austempered ductile iron. *Wear* **2006**, *260*, 879–885. [[CrossRef](#)]
38. Grum, J.; Sturm, R. Microstructure analysis of nodular iron 400-I 2 after laser surface melt hardening. *Mater. Charact.* **1996**, *37*, 81–88. [[CrossRef](#)]
39. Janicki, D.; Górka, J.; Kwasny, W.; Pakieła, W.; Matus, K. Influence of solidification conditions on the microstructure of laser-surface-melted ductile cast iron. *Materials* **2020**, *13*, 1174. [[CrossRef](#)]

Article

Microstructural and Erosive Wear Characteristics of a High Chromium Cast Iron

Annalisa Fortini , Alessio Suman , Alessandro Vulpio, Mattia Merlin  and Michele Pinelli

Department of Engineering, University of Ferrara, 44122 Ferrara, Italy; alessio.suman@unife.it (A.S.); alessandro.vulpio@unife.it (A.V.); mattia.merlin@unife.it (M.M.); michele.pinelli@unife.it (M.P.)

* Correspondence: annalisa.fortini@unife.it

Abstract: Surface material loss due to erosive wear is responsible for the increased cost of maintenance and downtime in industries. Hence, hardfacing is one of the most valuable and effective techniques employed to improve the wear resistance of heavy-duty components. The present paper investigates the microstructural and erosive wear characteristics of a hypereutectic high-chromium cast iron, considering the erosion resistance, resulting from the impact of micro-sized particles, of both as-received and heat-treated conditions. Micro-sized particles involve the erosion-resistant characteristics of carbide and matrix, contemporary. Due to this, the enhancement of the matrix strength could improve the mechanical support to withstand cracking deformation and spalling. Accordingly, the effect of a destabilization heat treatment on the microstructure was firstly investigated by hardness tests, X-ray diffraction analyses, optical and scanning electron microscopy. Specifically designed erosive tests were carried out using a raw meal powder at an impingement angle of 90°. The resulting superior wear resistance of the heat-treated samples was relayed on the improved matrix microstructure: consistent with the observed eroded surfaces, the reduced matrix/carbides hardness difference of the heat-treated material is pivotal in enhancing the erosion resistance of the hardfacing. The present results contribute to a better understanding of the microstructure–property relationships concerning the erosive wear resistance.



Citation: Fortini, A.; Suman, A.; Vulpio, A.; Merlin, M.; Pinelli, M. Microstructural and Erosive Wear Characteristics of a High Chromium Cast Iron. *Coatings* **2021**, *11*, 490. <https://doi.org/10.3390/coatings11050490>

Received: 30 March 2021
Accepted: 19 April 2021
Published: 22 April 2021

Publisher's Note: MDPI stays neutral with regard to jurisdictional claims in published maps and institutional affiliations.



Copyright: © 2021 by the authors. Licensee MDPI, Basel, Switzerland. This article is an open access article distributed under the terms and conditions of the Creative Commons Attribution (CC BY) license (<https://creativecommons.org/licenses/by/4.0/>).

Keywords: hardfacing; high chromium cast iron; heat treatment; erosion tests; wear resistance

1. Introduction

A widespread solution in industrial applications to extend the service life of components, in machinery equipment or construction, is found in cladding certain areas of the surface exposed to various severe wear conditions. Within the different surface coating protective and hardening techniques, hardfacing is one of the most adopted due to its low-cost and easy handling characteristics [1,2]. Hardfacing enables enhancing the corrosive, abrasive, and heat resistance properties of a metal workpiece's surface, creating a cladding metal layer with improved features [3]. Iron-based hardfacing alloys are the most widely-used thanks to their good wear resistance and low cost. Among these, due to their superior wear resistance, High Chromium Cast Irons (HCCIs) are broadly employed in both abrasive (e.g., grinding media) and erosive (e.g., slurry, gravel, and dredge pumps) applications [2]. Accordingly, HCCIs are widely used in minerals and mining industries, cement plants, paper and pulp industry, thermal power plants, iron and steel industries, etc.

Considering that hardfacing is usually deposited on the substrate by welding techniques, the microstructure of Fe–Cr–C hardfacing alloys resulting from a non-equilibrium solidification process consists of a Fe–Cr solid solution phase and complex carbides, depending on the Cr and C contents of the alloys. Cr-rich cast irons with hypereutectic structure, i.e., primary M_7C_3 carbides surrounded by eutectic austenite and M_7C_3 carbides [2,4–6], show high hardness and superior wear resistance to the hypoeutectic ones. The excellent abrasion resistance of hypereutectic alloys stems from the dispersion of the

hard (1300–1800 HV) M_7C_3 eutectic carbides [7,8]. Despite that, the as-cast condition of hypereutectic HCCIs cannot meet the demand of heavy impact conditions due to the difference in hardness between the matrix and the carbides. Hence, while on the one hand hypoeutectic HCCIs are still used in high demanding environments, on the other hand, efforts are devoted to enhancing the wear resistance of both hypo- and hyper-eutectic alloys [9]. HCCIs may be regarded as composite materials as they show a structure composed of large eutectic M_7C_3 carbides in a softer iron matrix. Hence, a good combination between matrix and carbides' hardness and toughness should be tuned to enhance the overall resistance [10].

Many studies have been focused on the improvement of wear resistance of HCCIs by the addition of strong carbide forming elements such as W [11,12], V [13], Nb [14,15], Ti [16], Mo [17,18], and B. Alloying elements are added to the melt to promote the precipitation of abrasion-resistance MC carbides (M is the metal and C is the carbon), stronger and harder than M_7C_3 ones [19–22]. At the same time, attention has been paid to the size, distribution, and volume fraction of carbide phases that overall affect the wear resistance of the alloy [23].

Moreover, the toughness and the strain hardening behavior of the matrix influence the wear resistance of the hardfacing since it should provide the mechanical support to withstand cracking deformation and spalling [7]. Several attempts have been made to improve the tribological and wear behavior of HCCIs through heat treatments [10,24–26] and mechanical treatments [27]. In the as-cast condition, the matrix is mainly austenite that, upon specific thermal treatments, is transformed into martensite. While the primary carbides formed inside the melt after casting and the eutectic carbides formed at about 1250 °C are not altered by heat treatment, the metastable austenite transforms to martensite through proper destabilization and subcritical treatments. To induce austenite to martensite phase transformations and, in turn, the overall hardness increment, heat treatments comprise heating for 1–6 h in the range of 900–1100 °C are usually applied [28].

In the last few decades, much research has been devoted to explaining the role of microstructural characteristics in the wear behavior of hardfacing alloys through specific wear tests (i.e., pin-on-disk or wheel, slurry erosion test, impact erosion resistance) [29–33]. Renewed attention has been paid to the impact erosion resistance of white cast irons, investigated through solid particle erosion tests [3,9,24,34–36]. Data from several studies have proved that wear resistance is not mainly influenced by the bulk hardness of the material, but it is a complex phenomenon derived from several factors, like type, volume fraction, size, and morphology of eutectic carbides together with their interaction with the matrix [7,37]. Moreover, the microstructural modifications of the matrix resulting from different heat treatments applied to destabilized the austenite are pivotal in the assessment of the wear resistance performance. Finally, to the authors' knowledge, there is no evidence about research on the wear behavior of HCCIs subjected to impact erosion tests with micrometric particles with diameters in the range of 1–10 μm , commonly used in the industrial process but very different from the standard powder used for erosion tests.

In the light of the above, the main objective of the present study is to investigate the microstructural features and wear erosive behavior of a commercially available hypereutectic HCCI. Accordingly, this paper begins with a synopsis of the literature regarding HCCIs and, more specifically Fe–Cr–C hardfacing alloys, to highlight the microstructural features responsible for their tribological behavior. The second section describes the adopted methods to assess the chemical, microstructural and mechanical features of the hardfacing alloy. Moreover, the erosion tests conducted through a dedicated test rig and the effect of a destabilization heat treatment on the microstructure and, in turn, on the erosion resistance, are explained. The third section of the paper describes the microstructural characterization of the hardfacing alloy, of nominal composition Fe–22Cr–4.8C wt.%, brings together the findings of hardness tests, optical microscopy, electron scanning microscopy and X-ray diffraction analyses. Further, considering the role of microstructural features on the wear properties of the alloy, the destabilization of austenite, through a heat treatment at 950 °C

for 3 h + oil quenching conducted to promote martensite formation and secondary carbides precipitation, is presented. The wear behavior of the as-received and heat-treated samples is investigated through a dedicated test rig, by simulating the operating condition of the considered HCCI alloy used in a large-sized centrifugal fan [38]. The observed improved erosion resistance is described and discussed. Lastly, the fourth section summarizes the main findings of the research study. The novelty of the present paper is related to the investigation of the wear-resistant behavior of the hardfacing alloy, before and after heat-treatment, used to overcome the erosion effects due to the impact of micro-sized particles. This latter characteristic has to be considered not only against the carbide hardness but also on the carbide morphology and matrix characteristics. This experimental study does not engage with a comprehensive evaluation of the destabilization temperature and time parameters that could be tuned to improve the erosive wear resistance of the investigated HCCI alloy. Likewise, it is beyond the scope of this preliminary study to examine the role of carbide spacing against the particle size distribution of the erodent powder.

2. Materials and Methods

The hardfaced plate analyzed in this study is a layer-composite wear plate, commercially available as EIPA 550 (Eipa Eisen Palmen GmbH, Aachen, Germany), made by the open-arc welding of a flux-cored wire. The HCCI hardfacing electrodes were deposited on a low carbon steel plate. The nominal thickness of the base steel, as well as of the hardfacing, is 5 mm. The chemical composition of the welded layer and the substrate were determined through the Glow Discharge Optical Emission Spectrometry (GD-OES, Spectruma Analytik GDS 650, Hof, Germany) technique. Table 1 reports the chemical composition of the alloys: note that for the HCCI the composition was analyzed in the cross-section considering both an acquisition area near the resistant side (at about 500 μm far from the top surface), named RS, and an acquisition area near the substrate side (at about 4500 μm far from the top surface), named SS. The HCCI is an Nb- and Mo-rich alloy, with a Cr/C ratio of about 5.

Table 1. Chemical composition (wt.%) of the hardfacing plate.

Site	Composition (wt.)—Fe Balance							
	C	Mn	Si	Cr	Mo	Nb	W	V
HCCI—RS	4.15	0.56	1.08	21.04	2.78	4.09	0.86	0.69
HCCI—SS	3.83	0.59	1.13	18.59	2.59	3.75	0.89	0.65
Carbon steel—Substrate	0.13	0.70	0.19	0.03	0.33	-	-	-

The microstructure of the hardfacing alloy was evaluated by sampling longitudinal sections, named L (parallel to the direction of welding), and cross-sections, named T (perpendicular to the direction of welding), following the basic steps for proper metallographic analysis, i.e., cutting, mounting in resin, grinding, final polishing and etching. The latter was conducted by Kalling's No. 2 reagent (5 g CuCl_2 , 100 mL HCl, 100 mL $\text{C}_2\text{H}_5\text{OH}$) to reveal the microstructure: the samples were immersed in the reagent for 5 s, rinsed with ethanol, and air-dried. Metallographic investigations were conducted through a Leica DMi8A (Leica, Wetzlar, Germany) optical microscope (OM) and a Zeiss EVO MA 15 (Zeiss, Oberkochen, Germany) scanning electron microscope (SEM), equipped with an Oxford X-Max 50 (Oxford Instruments, Abingdon-on-Thames, UK) energy dispersive microprobe for semi-quantitative analyses (EDS). The SEM micrographs were recorded in secondary electron imaging (SEI-SEM) and back-scattered electron (BSE-SEM) modes.

Crystallographic phase identification was performed by X-ray diffractometry (XRD) with a Bruker D8 Advance (Bruker, Billerica, MA, USA) diffractometer, equipped with a Cu filament ($K\alpha$, 1.5406 Å). All patterns were acquired in the 2θ range of 30° to 80° with 0.02° of step-size and 1 s of step time.

Quantitative metallographic analyses, after preliminary post-processing of the optical micrographs, using the MATLAB® Color Thresholder app and then evaluation through

the Leica LAS (Leica Application Suite) V4.9 software, enabled to examine the Carbide Volume Fraction (% CVF). For each sample, the analyzed region comprised a total of 20 micrographs for the SS and the RS, respectively.

Bulk hardness measurements were carried out on the polished cross-sections of the samples to evaluate the variation in hardness from the resistant side of the hardfacing to the steel substrate of the wear plate. The Vickers hardness measurements, under 1000 g test load and 15 s loading time (HV1), were carried out by a Future-Tech FM-110 (Future-Tech Corp., Kawasaki, Japan) Vickers indenter, in agreement with the ASTM E92 standard. Moreover, Vickers microhardness on the T cross-sections of the polished and etched hardfacing alloy was also evaluated on both the matrix (test load of 200 g and 15 s loading time, HV0.2) and on the carbides (test load of 50 g and 15 s loading time, HV0.05). In all cases, the mean Vickers hardness was calculated from five indentations.

Erosion tests were carried out using an on-purpose built test rig inspired by the ASTM G76 standard [39]. Since the present analysis was conceived to explore the erosion behavior due to a micro-sized powder, the feeding systems, as well as the nozzle, were modified with respect to the prescribed ones to ensure a constant feeding rate and avoiding clogging phenomenon during the test. The raw meal powder considered in this investigation was experimentally characterized to define particle morphology, size distribution and physical characteristics. The erosion tests were carried out by a raw meal powder commonly used in a cement factory, able to form several agglomerates due to humidity. Digital and SEI-SEM images of a powder sample in the as-received condition are displayed in Figure 1a,b. The overall average density of the powder was evaluated by an AccuPyc II 1340 (Micromeritics Instrument Corporation, Norcross, GA, USA) pycnometer and it results equal to 2700 kg/m^3 . Moreover, a quantitative analysis of particle diameter distribution is carried out to evaluate the presence of different diameter particles (d_p) within the powder. The particle size distribution is determined by a Mastersizer 3000 laser diffraction analyzer (Malvern Panalytical, Malvern, UK) and it is depicted in Figure 1c, which reports the number, labeled as N, and mass distributions, labeled as M, of the powder. The raw meal powder was characterized by an average diameter of $4.3 \mu\text{m}$ ($d_{90} = 9.7 \mu\text{m}$).

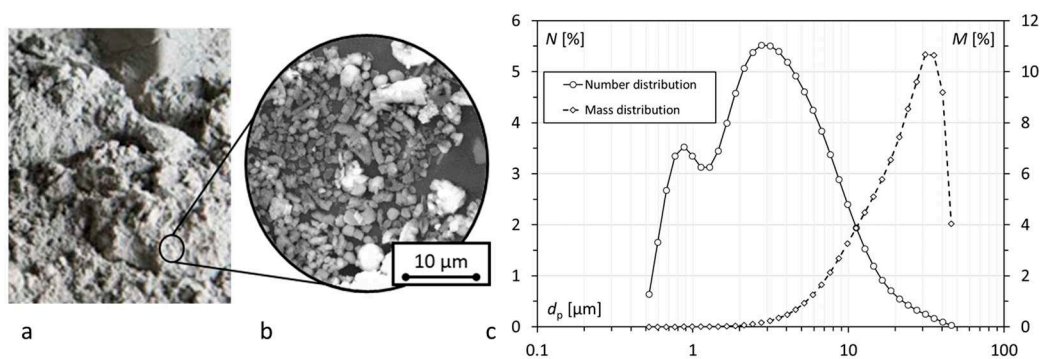


Figure 1. (a) Digital and (b) SEI-SEM images of the powder in the as-received condition, (c) number, N, and mass distributions, M, of the raw meal powder.

The feeding system is comprised of two different systems to guarantee the constant dosing rate and the breaking process of the agglomerates. The first part is composed of a hopper, equipped with a calibrated screw able to dosing the powder in the reservoir connect to a Venturi nozzle. The Venturi nozzle is operated by dried and cleaned shop air in order to suck the powder from the secondary line connected to the throat section. By the shear force, the Venturi nozzle allows the breakup of the agglomerates [40,41] ensuring the repeatability of the erosion tests. After the Venturi, a cylindrical nozzle with an internal diameter of 4 mm and a length equal to 32 mm was mounted. The sample overlook the nozzle at a fixed distance equal to 10 mm according to the standard, as reported in Figure 2a and it is held by a sliding and tiltable table to adjust the relative angle between nozzle and specimen surface

as reported in Figure 2b. Samples with dimensions of 50 mm × 25 mm × 10 mm were cut (by abrasive water-jet process) from the wear plate and their top surface was ground, polished (mirror-like finishing up to 1 μm diamond paste), and ultrasonically cleaned in acetone. The erosion test used a constant powder-feeding rate (10 g/min), impingement angle (90°), and particle impact velocity (100 m/s).

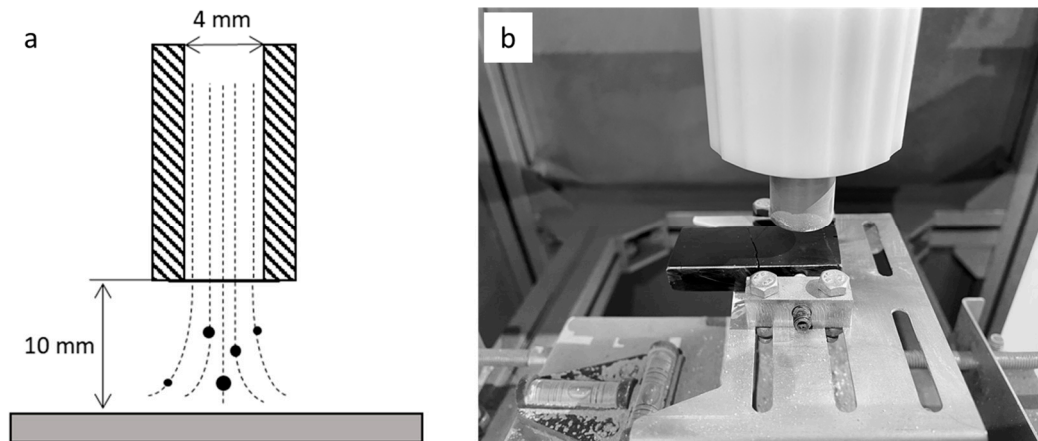


Figure 2. (a) Sample and nozzle setup, (b) image of the erosion sample on the sliding and tiltable table.

Three different erosion times, i.e., 30 min, 60 min, and 90 min, were investigated. For each condition, five samples were tested. After each erosion test, the sample was ultrasonically cleaned in acetone to remove any traces of the erodent powder. The erosion resistance was evaluated from the mass loss, computed by weighing each specimen before and after the erosion test. A Kern ABT 100-5NM (Kern, Balingen, Germany) analytical balance, with an accuracy resolution of 0.01 mg was used.

The worn surfaces were then analyzed by both optical and scanning electron microscopy in an attempt to provide a better understanding of the mechanisms of material removal. The investigations were conducted on the worn top surface and the cross-sectioned surface. The latter was cut in the center of the erosion crater and polished using the above-described standard metallographic technique.

By using an LTF (Lenton Furnaces and Ovens, Hope, UK) tube furnace, the effects of a destabilization heat treatment on the resulting microstructure and, in turn, on the erosion behavior, were evaluated. Similar to the erosion times investigated in the as-received condition, i.e., 30 min, 60 min, and 90 min, also for the heat-treated condition five samples were tested at the same erosion times. To this end, the furnace was heated at 20 °C/min up to 950 °C, and then the samples were held at this temperature for 3 h to promote the destabilization of the austenite phase. The final oil quenching to room temperature enabled to precipitate a fine dispersion of the carbides within the matrix. The overall bulk hardness of the hardfacing, before and after the heat treatment, was evaluated under 30 kg load and 15 s loading time (HV30) by VH Metkon (Metkon Instruments Inc., Bursa, Turkey) Vickers hardness tester. The hardness of the welded layer was determined as the average of five indentations to check the reproducibility of the hardness data. Then, both microstructural investigations and erosion tests were carried out according to the above-described methods. Microstructural (OM, SEM/EDS) and crystallographic (XRD) investigations were performed on the heat-treated samples to evaluate the relationship between microstructural features and erosion resistance.

3. Results and Discussion

3.1. Microstructural Investigations of the As-Received HCCI

Figure 3a displays a digital image of the resistant side of the wear plate in the as-received condition from which the bead pattern, i.e., juxtaposed passes with continuous

overlap, enables to counteract severe wear conditions. Moreover, stress relief cracks, resulting from the relaxation of heat stress in the deposit, develop at right angles to the weld beads and are regularly spaced. To ensure the wear resistance of the hardfacing, these cracks must not be spread to the base metal. Figure 3b shows the 3D isometric optical micrographs of the wear plate in the hardfacing/substrate interface. As can be seen from the cross-section, the crack does not reach the steel substrate, thanks to the buffer layer (the light gray band between the hardfacing and the steel) that acts as a barrier to cracking.

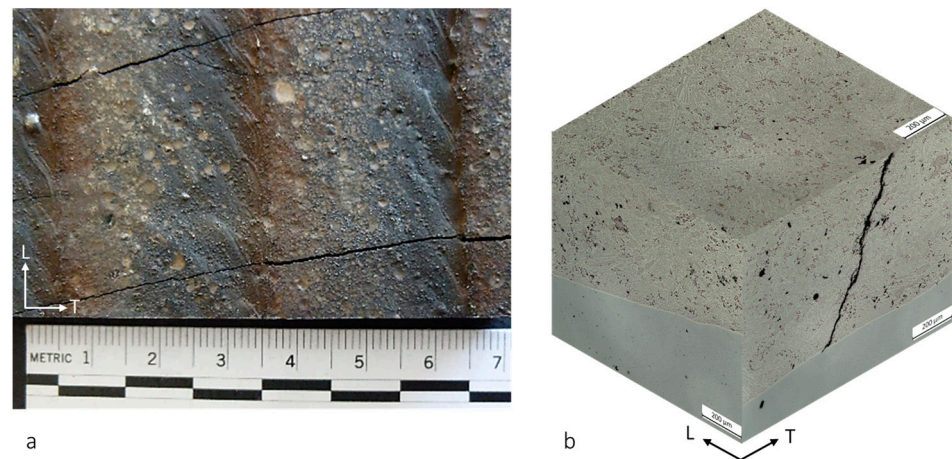


Figure 3. Hardfacing plate: (a) image of the resistant side of the wear plate; (b) 3D isometric optical micrographs of the unetched Fe-Cr-C alloy.

X-ray diffraction pattern of the deposit on the resistant-side layer is shown in Figure 4: the presence of MC ($M = \text{Nb}, \text{Mo}$), M_7C_3 ($M = \text{Cr}, \text{Fe}$), and austenite phases can be detected. Per the liquidus projection of the iron corner of the Fe–Cr–C ternary system [42,43] and according to the evaluated chemical composition (Table 1), the present alloy hardface deposit falls in the hypereutectic range. Considering the presence of Nb in the alloy, the formation of MC ($M = \text{Nb}$) carbides precedes the formation of proeutectic M_7C_3 carbides [44–46]. MC carbides precipitate at a high temperature in the melt before the formation of proeutectic M_7C_3 carbides, acting as heterogeneous nucleation sites and increasing the nucleation rate promoting the formation of finer proeutectic M_7C_3 carbides [44]. As the molten temperature falls to the eutectic point, the residual melt rejects the Cr and C atoms: when the Cr and C concentrations reach the eutectic composition, the $(\gamma + M_7C_3)$ eutectic colonies form [44].

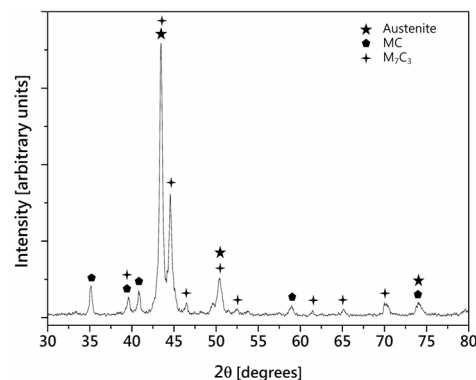


Figure 4. X-ray Diffraction (XRD) patterns of the hardfacing on the resistant-side layer.

The microstructure of the hardfacing, obtained from the polished and etched cross-section samples, is reported in Figure 5. Figure 5a shows the optical micrograph of the T-section of the alloy on the resistant side: in the upper part, i.e., close to the surface, the

hardfacing presents blade-like proeutectic M_7C_3 carbides, with the longer axis perpendicular to the surface and whose orientation is related to the heat flow [47], and the $(\gamma + M_7C_3)$ eutectic mixture.

With the increase of the distance from the resistant side, the carbides become finer, rod-like, and uniformly distributed throughout the matrix. The red arrows in Figure 5a highlight the stress-relief crack propagation path. SEM investigations were also conducted on the T cross-section of the hardfacing, at about half of the hardfacing thickness, and at the boundary between two welding passes. As revealed in the BSE-SEM image of Figure 5b, the different microstructure of the two passes, with coarser primary carbides on the left side of the micrograph and finer ones on the right side, is detectable. The dash-dot yellow line separates the passes with coarser and finer rod-like carbides. The optical micrographs of Figure 5c,d compare the microstructure of the SS (Figure 5c) and the RS (Figure 5d) regions of the L-section. Both reveal the presence of γ dendrites (highlighted by red arrows) adjacent to the proeutectic M_7C_3 carbides, whose content is greater in the RS region (Figure 5d). This finding has also been recently reported and described in [44]. Moreover, the effect of the solidification conditions is detectable: near the surface, the higher thermal gradient results in primary blade-like M_7C_3 carbides that grow along the preferential growth axis [47]. In addition to the high magnification optical micrographs of Figure 5c,d, BSE-SEM analyses were conducted to highlight the microstructural constituents through compositional contrast imaging. Hence, Figure 5e displays the BSE-SEM micrograph of the T-cross section, which provides an overview of the microstructure, while the high magnification micrograph of Figure 5f points out the eutectic carbides network. Consistent with the XRD results (see Figure 4), the BSE-SEM micrographs of the T-section (Figure 5e,f) reveal a microstructure composed of primary M_7C_3 carbides (labeled as 1) surrounded by the eutectic $(\gamma + M_7C_3)$ structure (labeled as 2). The carbides reveal a rhombohedral/hexagonal cross-section [48]. Nb additions enabled the precipitation of Nb-rich MC carbides displayed as polygonal-shaped structures (labeled as 3), as confirmed by the EDS analyses. Nb- and Mo-rich carbides (labeled as 4) and Mo- and Fe-rich carbides (labeled as 5) have also been detected. From the high magnification BSE-SEM micrograph of Figure 5f, traces of martensite (labeled as 6) could also be observed at the periphery of the carbides network [7,49,50].

Considering the influence of the CVF on the microstructural and wear characteristics of the hardfacing [29,31,51], quantitative metallographic image analyses were carried out. Figure 6 displays examples of the representative microstructures analyzed to evaluate the CVF parameter: Figure 6a,b show the L-section in the RS and SS, respectively, while Figure 6c,d show the T-section in the RS and SS, respectively.

As seen, the RS presents larger carbides with a plate-like morphology, while the SS presents smaller primary carbides with a polygonal shape. It is worth noting that, even within the same distance from the surface, the microstructure was quite heterogeneous, as the result of the solidification process. The estimated mean CVF values were 26.25% and 23.45% for the L-section in the RS and SS, respectively, while 25.98% and 24.40% for the T-section in the RS and SS, respectively. Beyond the negligible differences in the number of carbides between L-section and T-section, attempts were made to evaluate the size of the investigated carbides. Hence, Figure 5e displays the Cumulative Distribution Function (CDF) of the carbides' area, A . These distributions reveal that for the L-section (both for the RS, labeled as L_RS, and for the SS, labeled as L_SS) about 90% of the carbides had an area in the range of 4–60 μm^2 while for the T-section (both for RS, labeled as T_RS and for the SS, labeled as T_SS) about 90% of the carbides had an area in the range of 2–40 μm^2 . In all cases, carbides with a larger area (from 100 μm^2 up to 900 μm^2) were much less with respect to the numerous eutectic carbides, the share of these large carbides amounted to about 10% of the total.

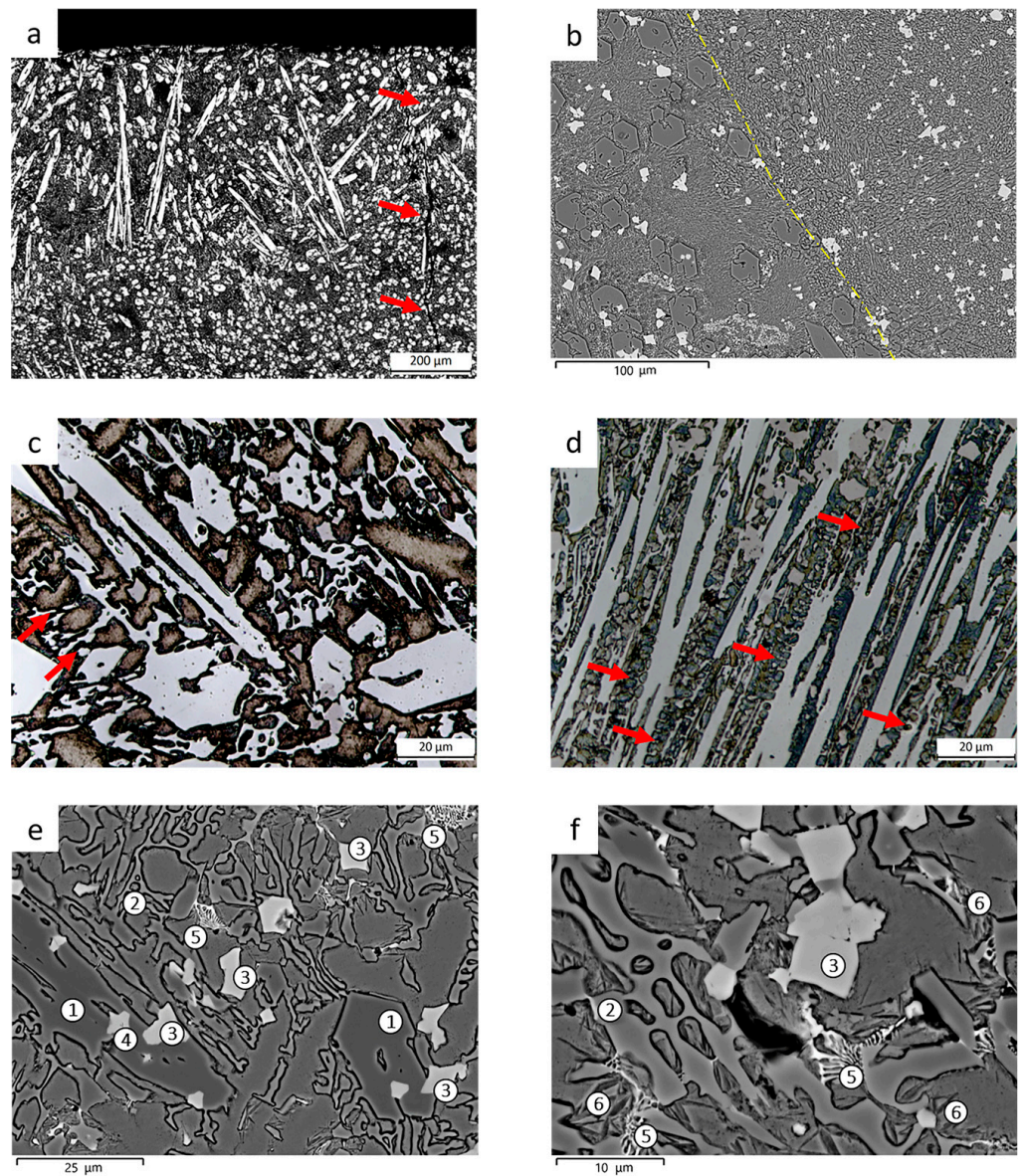


Figure 5. (a) Optical microscope (OM) micrograph of the T-section of the hardfacing captured from the resistant side, red arrows highlight the crack propagation path; (b) BSE-SEM image of the T-section at the boundary between two welding passes: the dash-dot yellow line separates the passes with coarser and finer rod-like carbides; (c,d) OM micrographs of the L-section in the substrate and resistant side, respectively; (e,f) BSE-SEM images of the T-section with primary M_7C_3 carbides (labeled as 1), eutectic ($\gamma + M_7C_3$) structure (labeled as 2), Nb-rich MC carbides (labeled as 3), Nb- and Mo-rich carbides (labeled as 4), Mo- and Fe-rich carbides (labeled as 5) and traces of martensite (labeled as 6).

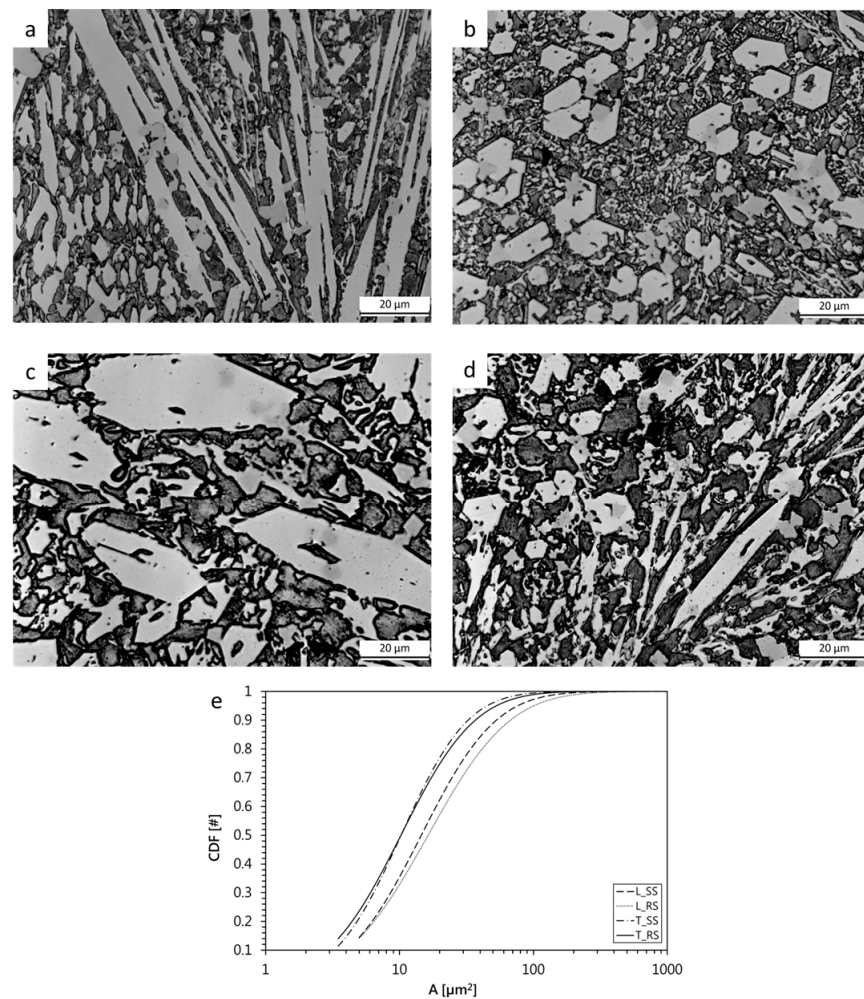


Figure 6. Representative OM micrographs used for the carbide volume fraction (% CVF) evaluation: L-section in the RS (a) and SS (b); T-section in the resistant side (RS) (c) and substrate side (SS) (d). (e) The cumulative distribution function (CDF) of the carbides' area A at different locations.

3.2. Hardness of the As-Received HCCI

The results of hardness measurements, taken on the T cross-section, are reported in Figure 7. Figure 7a shows the Vickers hardness profile measured at increasing distances of 1 mm from the top of the welded hardfacing up to the bottom of the steel substrate. Moreover, the hardness of both the matrix and the primary carbides was evaluated (Figure 7b).

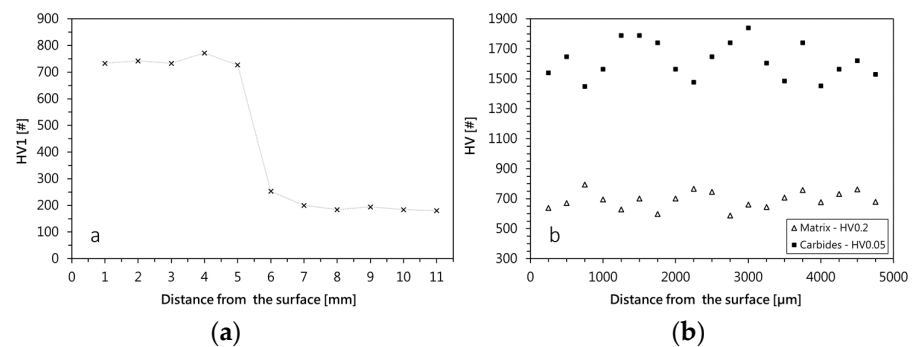


Figure 7. Vickers hardness measurements on the T cross-section: (a) hardness profile across the hardfacing plate from the resistant side up to the steel substrate; (b) microhardness values across the hardfacing for matrix and Cr-based carbides.

3.3. Effect of the Heat Treatment on Microstructure and Erosion Behavior

The erosive resistance of the investigated HCCI was evaluated by erosion tests conducted by comparing the behavior of the alloy in the as-received and heat-treated conditions. Consecutive tests at 30 min, 60 min, and 90 min of erosion were conducted.

Figure 8 represents the BSE-SEM microstructures of the as-received and heat-treated samples, together with the respective XRD spectra. In the as-received state, the high magnification BSE-SEM micrograph (Figure 8a) displays a microstructure mainly consisted of M_7C_3 eutectic carbides, traces of martensite, and MC carbides, in accordance with the identified phases in the respective XRD spectrum (Figure 8c). In the heat-treated condition, the austenite is transformed into martensite, as revealed by the BSE-SEM micrograph (Figure 8b) and by the martensite peak in the XRD spectrum (Figure 8c).

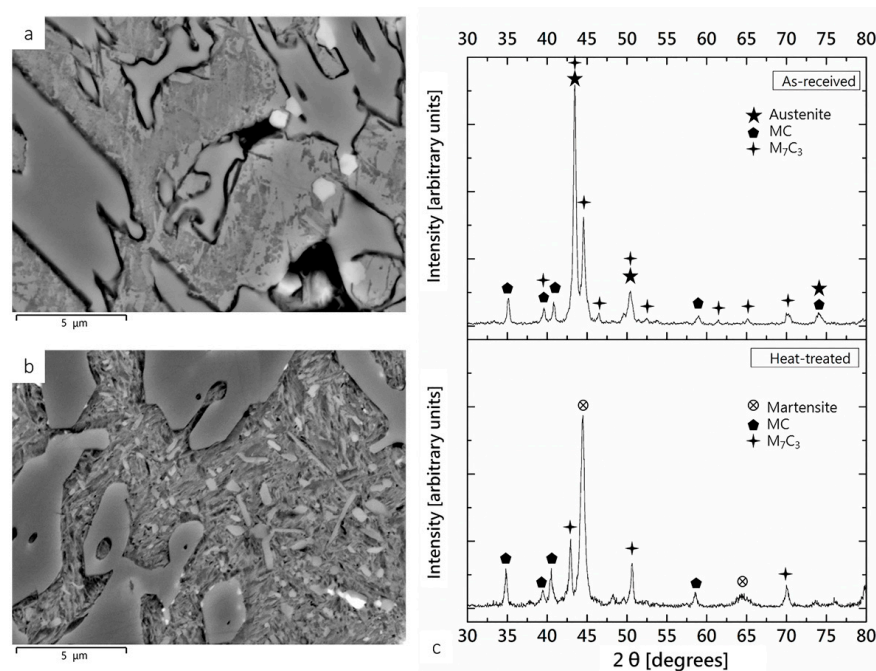


Figure 8. Comparison between as-received and heat-treated conditions. (a,b) BSE-SEM images of the hardfacing microstructure: (a) as-received and (b) heat-treated at 950 °C for 3 h and oil quenched. (c) XRD spectra of the as-received and heat-treated conditions.

After destabilization, the secondary carbides precipitated during the heat treatment appear as fine granular particles distributed in the matrix (Figure 8b) [52]. These carbides are detectable from the BSE-SEM images resulting from the deep-etched samples. Figure 9 reports the comparison between the microstructure of the as-received and the heat-treated samples after etching for 24 h in a solution of 10% HCl in methanol, as suggested by [7]. From the BSE-SEM image of Figure 9b, the small and uniformly distributed secondary carbides are detectable, in the framework of the matrix structure.

Accordingly, the overall bulk hardness is increased by the thermal treatment: the as-received sample shows 793 ± 35 HV30 while the heat-treated sample results in 950 ± 52 HV30. Figure 10 exhibits the appearance of a representative worn top surface of an erosion crater on the as-received sample. From the digital image (Figure 10a) it can be seen the modification of the substrate surface due to the particle impact. The erosion pattern is characterized by a circular spot with two concentric regions (commonly known as a crater). The internal matt-grey region (with a diameter equal to about 5 mm) overlooks the nozzle: in this region, particles impact the substrate for the first time at 90° with the nominal velocity determining the greater erosion damage. The external circular light-grey region (with a diameter equal to about 9 mm) is generated by the secondary impacts characterized by lower impact angle (almost tangential impact) and lower impact velocity. Hence, the

analyzed eroded area of the worn top surface of the sample, as depicted in the BSE-SEM image of Figure 10b, was a circle of about 3 mm diameter in the central region of the erosion crater.

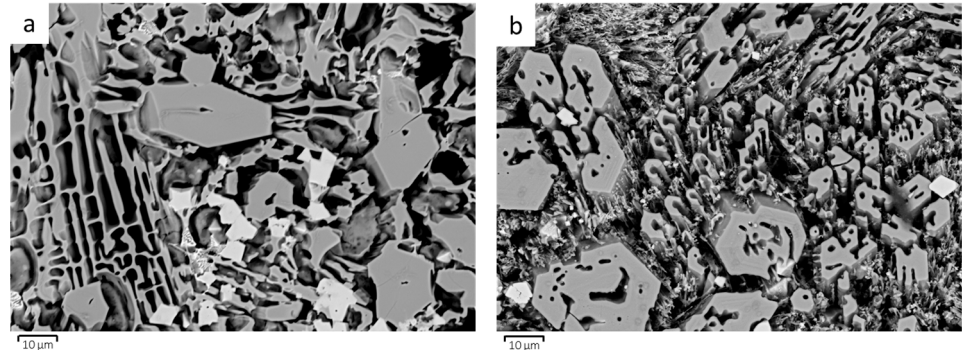


Figure 9. Deep-etched BSE-SEM images of (a) as-received and (b) heat-treated samples.

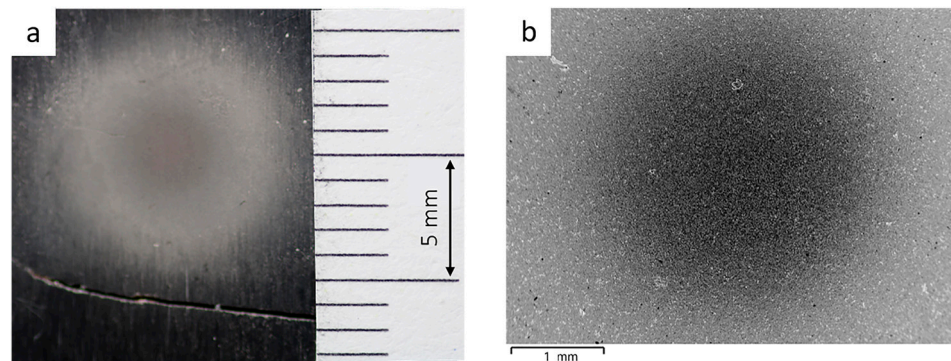


Figure 10. Images of the top surface after erosion: (a) digital image; (b) BSE-SEM image.

The worn surface was analyzed through SEM observation of the top surface after the erosion process. As depicted in Figure 11, which displays the worn surface of an erosion crater on the as-received sample after 30 min of erosion, SEM images revealed both the topography of the worn surface (Figure 11a) and the distribution of the chemical elements, detected by the X-ray elemental maps (Figure 11b,c). Due to the erosion, the surface appears rough, with the Cr-rich carbides protrusions resulting from the selective wear of the matrix [31].

Previous research has established the tricky phenomena associated with the wear behavior of HCCIs, deeply investigating the role of matrix, primary and eutectic carbides on the wear resistance [31]. The cross-section of the erosion crater, in the as-received condition, was thus investigated by SEM: Figure 12 depicts the comparison between 30 min and 60 min of erosion of two different regions of the same sample. As can be seen, the cross-section analysis in the center of the erosion crater does not provide information about the erosion mechanisms that occurred. Time-wise evolution of the erosion and wear phenomena are not detectable only by the cross-section evaluation. After 30 min of erosion, Figure 12a, primary M_7C_3 carbides appear emerging from the surrounding matrix, which results in some damage by the erodent particles. Conversely, after 60 min of erosion, the center of the erosion crater appears uniformly eroded, with no evident carbide protrusions (Figure 12b). Such behaviors rely on the mutual interdependence between microstructural features, of both matrix and carbides (i.e., size, volume fraction, distribution of primary carbide and eutectic carbides), and fracture behavior (i.e., fracture toughness and hardness). It has been reported [31] that hard primary carbides near the surface could be spalled off as they are cracked during the wear process, despite the high hardness. At the same time, the microstructure, mainly composed of eutectic carbides that show a lower hardness because

of the decrease of the volume fraction of the M_7C_3 , reveals a better wear resistance thanks to the uniform distribution of such carbides. Such harder and uniformly distributed carbides ensure an increased wear resistance since abrasives cannot effectively penetrate into the matrix and carbides are not easily separate from it [53,54]. According to the literature, relatively homogeneous wear is observed (Figure 12b).

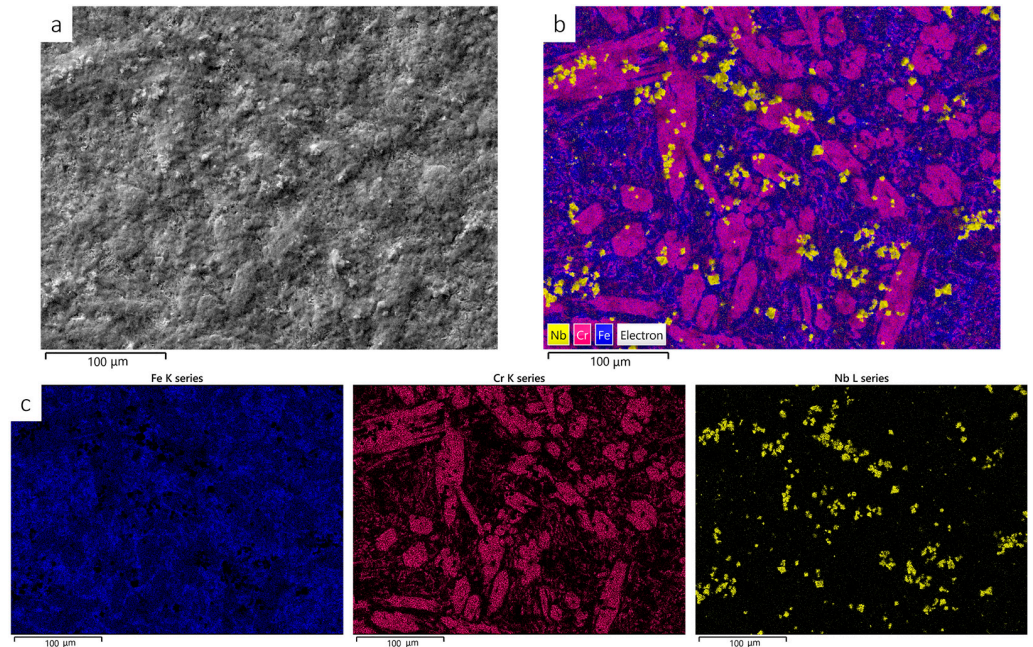


Figure 11. SEM images of the worn surface, center of the crater after 30 min of erosion on an as-received sample: (a) SEI-SEM image, (b) layered image of X-ray maps, and (c) maps of the elemental distribution.

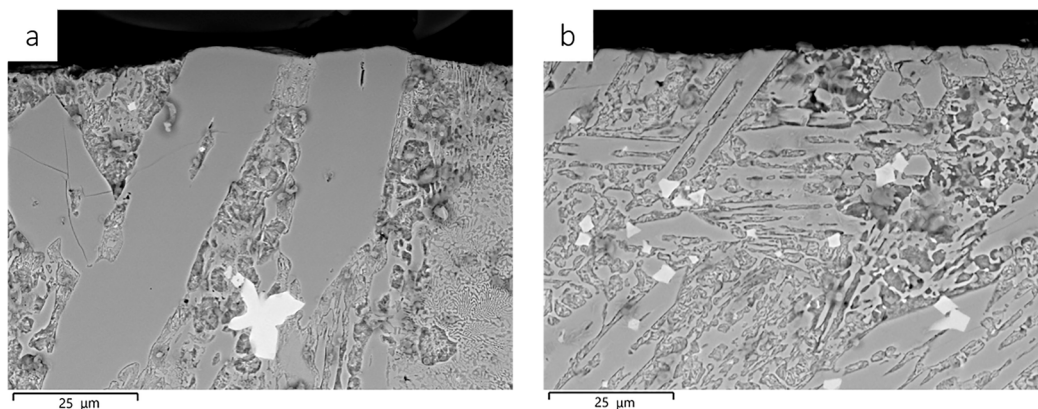


Figure 12. BSE-SEM micrographs of the cross-sectioned erosion crater: (a) 30 min of erosion, (b) 60 min of erosion.

In the light of the above reported microstructural findings, to exclude the influence of the microstructural changes associated with the chemical and solidification conditions, erosion tests were performed on the same area of the sample. The erosion results are reported in Figure 13, as the weight loss against the exposure time: it follows that the wear behavior of the heat-treated samples toward erosion is better than the as-received ones. Regardless of the condition, the weight loss by the sample increases with the erosion time with a slightly lower slope for the heat-treated sample. It is worth noting the weight loss decrease for the heat-treated condition, promoted by the destabilization treatment and, in turn, by the superior erosion resistance of the obtained microstructure. Conversely, the weight loss of the as-received sample increases linearly with erosion time. Note that the

uncertainty band associated with the weight loss measurements has the same size as the markers on the charts (extended uncertainty is ± 0.06 mg).

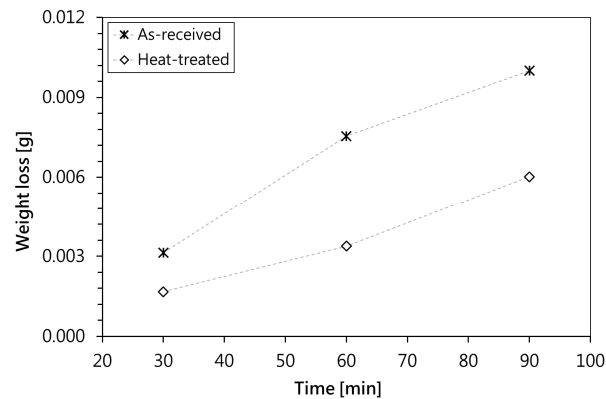


Figure 13. Erosion tests result for the as-received and heat-treated hardfacing samples: weight loss against erosion time.

The microstructural investigations were performed on the top worn surfaces by both OM to evaluate the CVF, and by SEM to study the topographical changes associated with the erosion phenomena. Since the morphologies of carbides, together with the microstructure of the matrix, are the predominant characteristics influencing the hardness and wear behavior of the alloy, it is of high relevance to consider their quantitative analysis. Table 2 summarizes the CVF values and the respective standard deviations in parentheses for the as-received and the heat-treated conditions.

Table 2. CVF values and respective standard deviations (in parenthesis) in the as-received and heat-treated conditions with respect to erosion time. The initial condition before the erosion test is 0 min.

Conditions	CVF			
	Erosion Exposure [min]			
	0	30	60	90
As-received	22.19 (1.31)	11.54 (2.34)	9.92 (2.41)	10.24 (3.99)
Heat-treated	28.84 (0.76)	12.54 (1.95)	14.74 (2.71)	13.86 (2.29)

As for the initial condition, indicated as 0 min, it can be stated that for the as-received and the heat-treated samples the CVF values are comparable. Conversely, from the comparison between the CVF values in the initial condition and after 30 min, 60 min, and 90 min of erosion it appears that, aside from the condition, the CVF is reduced to half its initial value and it seems not significantly affected by the erosion time. These experimental findings shed light on the time-wise evolution of weight loss (see Figure 13).

To further investigate the efficacy of the heat treatment, SEM analyses of the worn top surfaces were conducted. Figure 14 presents the topography in the center of the crater after erosion through both SEI-SEM and BSE-SEM images.

From the comparison between the worn surfaces of the as-received (Figure 14a,b) and the heat-treated (Figure 14c,d) samples after 30 min of erosion, it can be detected the different wear behavior. The surface of the as-received sample shows wide carbide protrusion resulting from the selective wear of the matrix while the heat-treated sample reveals the simultaneous wear of matrix and carbides. Indeed, the reduced hardness difference between matrix and carbides in the heat-treated sample, 850 ± 52 HV0.2, and 1620 ± 122 HV0.05 respectively, compared with the as-received sample, 692 ± 58 HV0.2 and 1477 ± 147 HV0.05 respectively, increases the wear resistance of the alloy.

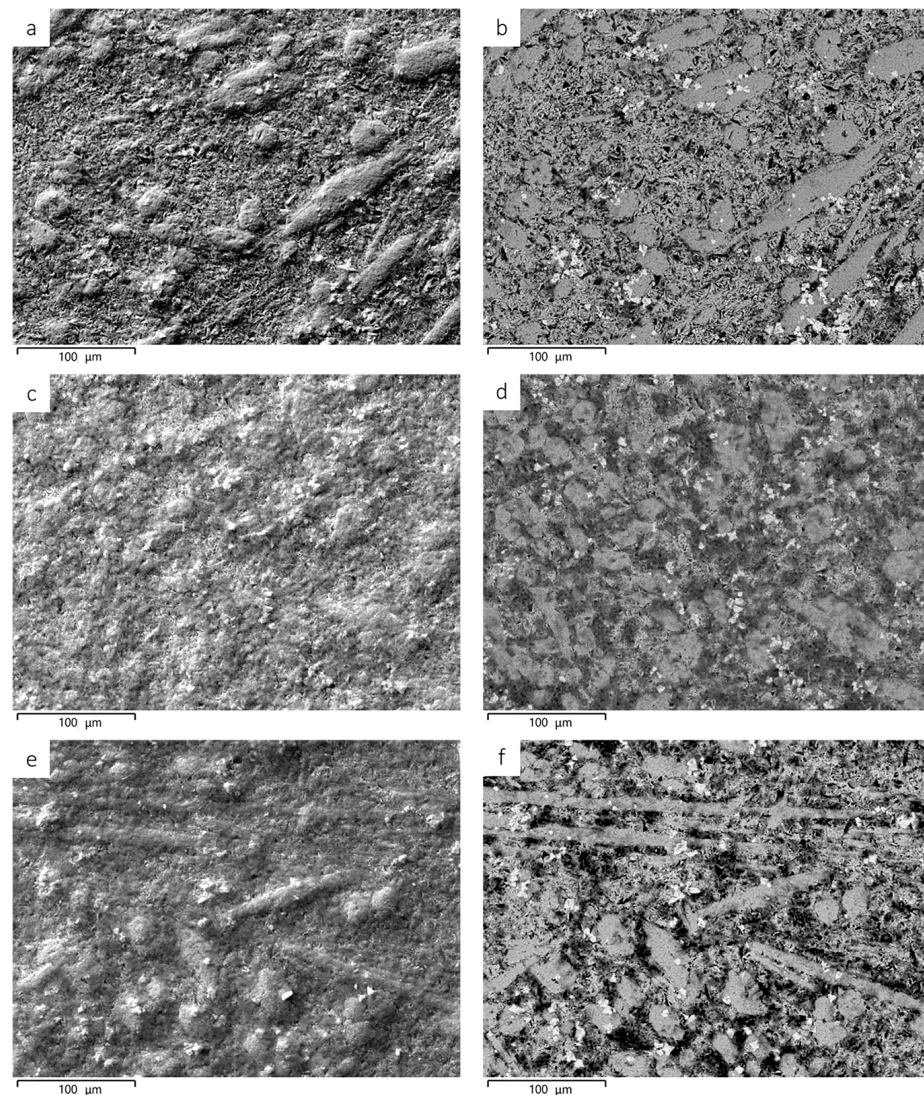


Figure 14. SEI-BSE images of the center of the crater: (a,b) SEI-BSE images of the as-received hardfacing after 30 min of erosion; (c,d) SEI-BSE images of the heat-treated hardfacing after 30 min of erosion; (e,f) SEI-BSE images of the heat-treated hardfacing after 60 min of erosion.

The improved wear resistance of the heat-treated sample is further confirmed by the surface topography appearance after 60 min of erosion (Figure 14e,f), which is somewhat similar to the condition of the as-received sample after 30 min of erosion (Figure 14a,b). Note that the weight loss of these two samples is nearly the same. In the light of that, it can be inferred the increased capability of the higher hardness matrix in providing better support for the carbides, compared with the austenitic one, in agreement with findings in [52].

These findings suggest that the proposed heat treatment is effective in improving the erosion resistance of the investigated HCCI alloy, which is strongly affected by the matrix/carbides hardness difference.

4. Conclusions

The microstructural characteristics and the erosive wear behavior of a hypereutectic HCCI hardfacing alloy were experimentally investigated by considering the effect of a destabilization heat treatment. The experimental findings indicate that:

- according to microstructural and X-ray diffraction analyses, the investigated HCCI consists of a mixture of MC and M_7C_3 carbides dispersed in a metastable austenite

matrix containing a high Cr concentration, with traces of martensite at the carbides' periphery. Nb-rich and Mo-rich carbides were also detected;

- the considered destabilization treatment (950 °C for 3 h + oil quenching) promotes the austenite to martensite phase transformation and the precipitation of secondary carbides;
- the erosion tests, performed at 30 min, 60 min, and 90 min, proved the efficacy of the heat treatment in improving the erosion resistance of the as-received alloy;
- the reduced hardness difference between matrix and carbides in the heat-treated sample has a pivotal role in increasing the wear resistance of the hardfacing.

With the objective of providing a better understanding of the microstructure-property relationships concerning the erosive wear resistance of a Fe–Cr–C hardfacing alloy, the experimental findings of this study give some remarkable hints, useful for optimized exploitation of HCCIs in heavy-duty applications. The key takeaways of the research improve the knowledge of the erosive behavior of hardfacing alloy due to the impact of micro-sized particles and would thus reflect towards the increase of their performance and, in turn, of their application ranges.

Author Contributions: Conceptualization, A.F. and A.S.; Data curation, A.V.; Investigation, A.V.; Methodology, A.F. and A.S.; Supervision, M.M. and M.P.; Writing—original draft, A.F.; Writing—review & editing, A.S. and M.M. All authors have read and agreed to the published version of the manuscript.

Funding: This research received no external funding.

Institutional Review Board Statement: Not applicable.

Informed Consent Statement: Not applicable.

Data Availability Statement: Not applicable.

Acknowledgments: The authors owe thanks to Eng. Paolo Saccenti of Boldrocchi S.r.l. (Biassono, Monza-Brianza, Italy) for the technical support in this research. The authors wish to gratefully acknowledge Luca Marchetti and Matteo Seno for their support in the experimental campaign. Thanks are also due to Iuri Boromei for his contribution to the GD-OES analyses.

Conflicts of Interest: The authors declare no conflict of interest.

References

1. Venkatesh, B.; Sriker, K.; Prabhakar, V.S.V. Wear Characteristics of Hardfacing Alloys: State-of-the-art. *Procedia Mater. Sci.* **2015**, *10*, 527–532. [[CrossRef](#)]
2. Jain, A.-S.; Chang, H.; Tang, X.; Hinckley, B.; Zhang, M.-X. Refinement of primary carbides in hypereutectic high-chromium cast irons: A review. *J. Mater. Sci.* **2021**, *56*, 999–1038. [[CrossRef](#)]
3. Jia, R.; Liu, S.; Luo, Z.; Ning, J.; Wang, H.; Luo, T.; Zhu, Y.; Yuan, X.; Wang, Z. Microstructure and wear resistance of WC and high chromium cast iron hardfacing layers. *Coatings* **2020**, *10*, 852. [[CrossRef](#)]
4. Buytoz, S. Microstructural properties of M₇C₃ eutectic carbides in a Fe-Cr-C alloy. *Mater. Lett.* **2006**, *60*, 605–608. [[CrossRef](#)]
5. Fan, C.; Chen, M.-C.; Chang, C.-M.; Wu, W. Microstructure change caused by (Cr,Fe)₂₃C₆ carbides in high chromium Fe-Cr-C hardfacing alloys. *Surf. Coat. Technol.* **2006**, *201*, 908–912. [[CrossRef](#)]
6. Lin, C.-M.; Chang, C.-M.; Chen, J.-H.; Hsieh, C.-C.; Wu, W. Microstructural evolution of hypoeutectic, near-eutectic, and hypereutectic high-carbon Cr-based hard-facing alloys. *Metall. Mater. Trans. A* **2009**, *40*, 1031–1038. [[CrossRef](#)]
7. Nayak, U.P.; Guitar, M.A.; Mücklich, F. A comparative study on the influence of chromium on the phase fraction and elemental distribution in as-cast high chromium cast irons: Simulation vs. experimentation. *Metals* **2019**, *10*, 30. [[CrossRef](#)]
8. Zhi, X.; Xing, J.; Gao, Y.; Fu, H.; Peng, J.; Xiao, B. Effect of heat treatment on microstructure and mechanical properties of a Ti-bearing hypereutectic high chromium white cast iron. *Mater. Sci. Eng. A* **2008**, *487*, 171–179. [[CrossRef](#)]
9. Gonzalez-Pociño, A.; Alvarez-Antolin, F.; Asensio-Lozano, J. Optimization of thermal processes applied to hypoeutectic white cast iron containing 25% Cr aimed at increasing erosive wear resistance. *Metals* **2020**, *10*, 359. [[CrossRef](#)]
10. Karantzalis, E.; Lekatou, A.; Mavros, H. Microstructure and properties of high chromium cast irons: Effect of heat treatments and alloying additions. *Int. J. Cast Met. Res.* **2009**, *22*, 448–456. [[CrossRef](#)]
11. Cortés-Carrillo, E.; Bedolla-Jacuinde, A.; Mejía, I.; Zepeda, C.M.; Zuno-Silva, J.; Guerra-Lopez, F.V. Effects of tungsten on the microstructure and on the abrasive wear behavior of a high-chromium white iron. *Wear* **2017**, *376–377*, 77–85. [[CrossRef](#)]
12. Lv, Y.; Sun, Y.; Zhao, J.; Yu, G.; Shen, J.; Hu, S. Effect of tungsten on microstructure and properties of high chromium cast iron. *Mater. Des.* **2012**, *39*, 303–308. [[CrossRef](#)]

13. Radulovic, M.; Fiset, M.; Peev, K.; Tomovic, M. The influence of vanadium on fracture toughness and abrasion resistance in high chromium white cast irons. *J. Mater. Sci.* **1994**, *29*, 5085–5094. [[CrossRef](#)]
14. Zhi, X.; Xing, J.; Fu, H.; Xiao, B. Effect of niobium on the as-cast microstructure of hypereutectic high chromium cast iron. *Mater. Lett.* **2008**, *62*, 857–860. [[CrossRef](#)]
15. Filipovic, M.; Kamberovic, Z.; Korac, M.; Gavrilovski, M. Microstructure and mechanical properties of Fe-Cr-C-Nb white cast irons. *Mater. Des.* **2013**, *47*, 41–48. [[CrossRef](#)]
16. Bedolla-Jacuinde, A.; Correa, R.; Quezada, J.G.; Maldonado, C. Effect of titanium on the as-cast microstructure of a 16% chromium white iron. *Mater. Sci. Eng. A* **2005**, *398*, 297–308. [[CrossRef](#)]
17. Scandian, C.; Boher, C.; de Mello, J.D.B.; Rézai-Aria, F. Effect of molybdenum and chromium contents in sliding wear of high-chromium white cast iron: The relationship between microstructure and wear. *Wear* **2009**, *267*, 401–408. [[CrossRef](#)]
18. Imurai, S.; Thanachayanont, C.; Pearce, J.T.H.; Tsuda, K.; Chairuangstri, T. Effects of Mo on microstructure of as-cast 28 wt.% Cr-2.6 wt.% C-(0–10) wt.% Mo irons. *Mater. Charact.* **2014**, *90*, 99–112. [[CrossRef](#)]
19. Chatterjee, S.; Pal, T.K. Weld procedural effect on the performance of iron based hardfacing deposits on cast iron substrate. *J. Mater. Process. Technol.* **2006**, *173*, 61–69. [[CrossRef](#)]
20. Liu, D.; Liu, R.; Wei, Y. Effects of titanium additive on microstructure and wear performance of iron-based slag-free self-shielded flux-cored wire. *Surf. Coat. Technol.* **2012**, *207*, 579–586. [[CrossRef](#)]
21. Hou, Q.Y.; He, Y.Z.; Zhang, Q.A.; Gao, J.S. Influence of molybdenum on the microstructure and wear resistance of nickel-based alloy coating obtained by plasma transferred arc process. *Mater. Des.* **2007**, *28*, 1982–1987. [[CrossRef](#)]
22. Yüksel, N.; Şahin, S. Wear behavior–hardness–microstructure relation of Fe–Cr–C and Fe–Cr–C–B based hardfacing alloys. *Mater. Des.* **2014**, *58*, 491–498. [[CrossRef](#)]
23. Tang, X.H.; Chung, R.; Li, D.Y.; Hinckley, B.; Dolman, K. Variations in microstructure of high chromium cast irons and resultant changes in resistance to wear, corrosion and corrosive wear. *Wear* **2009**, *267*, 116–121. [[CrossRef](#)]
24. Gelfi, M.; Pola, A.; Girelli, L.; Zacco, A.; Masotti, M.; La Vecchia, G.M. Effect of heat treatment on microstructure and erosion resistance of white cast irons for slurry pumping applications. *Wear* **2019**, *428–429*, 438–448. [[CrossRef](#)]
25. Abdel-Aziz, K.; El-Shennawy, M.; Omar, A.A. Microstructural characteristics and mechanical properties of heat treated high-Cr white cast iron alloys. *Int. J. Appl. Eng. Res.* **2017**, *12*, 4675–4686.
26. Guitar, M.A.; Suárez, S.; Prat, O.; Duarte Guigou, M.; Gari, V.; Pereira, G.; Mücklich, F. High chromium cast irons: Destabilized-subcritical secondary carbide precipitation and its effect on hardness and wear properties. *J. Mater. Eng. Perform.* **2018**, *27*, 3877–3885. [[CrossRef](#)]
27. González, J.; Peral, L.B.; Zafra, A.; Fernández-Pariente, I. Influence of shot peening treatment in erosion wear behavior of high chromium white cast iron. *Metals* **2019**, *9*, 933. [[CrossRef](#)]
28. Efremenko, V.; Shimizu, K.; Chabak, Y. Effect of destabilizing heat treatment on solid-state phase transformation in high-chromium cast irons. *Metall. Mater. Trans. A* **2013**, *44*, 5434–5446. [[CrossRef](#)]
29. Sapate, S.; Rama Rao, A. Effect of carbide volume fraction on erosive wear behaviour of hardfacing cast irons. *Wear* **2004**, *256*, 774–786. [[CrossRef](#)]
30. Sapate, S.G.; RamaRao, A.V. Erosive wear behaviour of weld hardfacing high chromium cast irons: Effect of erodent particles. *Tribol. Int.* **2006**, *39*, 206–212. [[CrossRef](#)]
31. Kim, C.K.; Lee, S.; Jung, J.-Y. Effects of heat treatment on wear resistance and fracture toughness of duo-cast materials composed of high-chromium white cast iron and low-chromium steel. *Metall. Mater. Trans. A* **2006**, *37*, 633–643. [[CrossRef](#)]
32. Gasan, H.; Erturk, F. Effects of a destabilization heat treatment on the microstructure and abrasive wear behavior of high-chromium white cast iron investigated using different characterization techniques. *Metall. Mater. Trans. A* **2013**, *44*, 4993–5005. [[CrossRef](#)]
33. Chatterjee, S.; Pal, T.K. Wear behaviour of hardfacing deposits on cast iron. *Wear* **2003**, *255*, 417–425. [[CrossRef](#)]
34. Gonzalez-Pociño, A.; Alvarez-Antolin, F.; Asensio-Lozano, J. Erosive wear resistance regarding different destabilization heat treatments of austenite in high chromium white cast iron, alloyed with Mo. *Metals* **2019**, *9*, 522. [[CrossRef](#)]
35. Gonzalez-Pociño, A.; Alvarez-Antolin, F.; Asensio-Lozano, J. Influence of thermal parameters related to destabilization treatments on erosive wear resistance and microstructural variation of white cast iron containing 18% Cr. Application of Design of Experiments and Rietveld structural analysis. *Materials* **2019**, *12*, 3252. [[CrossRef](#)]
36. Fordyce, I.; Annasamy, M.; Sun, S.D.; Fabijanic, D.; Gallo, S.C.; Leary, M.; Easton, M.; Brandt, M. The effect of heat treatment on the abrasive and erosive wear behaviour of laser metal deposited Fe–28Cr–2.7C alloy. *Wear* **2020**, *458–459*, 203410. [[CrossRef](#)]
37. Chatterjee, S.; Pal, T.K. Solid particle erosion behaviour of hardfacing deposits on cast iron—Influence of deposit microstructure and erodent particles. *Wear* **2006**, *261*, 1069–1079. [[CrossRef](#)]
38. Aldi, N.; Casari, N.; Pinelli, M.; Suman, A.; Vulpio, A.; Saccenti, P.; Beretta, R.; Fortini, A.; Merlin, M. Erosion behavior on a large-sized centrifugal fan. In Proceedings of the 13th European Turbomachinery Conference on Turbomachinery Fluid Dynamics and Thermodynamics, ETC 2019, Lausanne, Switzerland, 8–12 April 2019.
39. ASTM G76. *Standard Test Method for Conducting Erosion Tests by Solid Particle Impingement Using Gas Jets*; ASTM International: West Conshohocken, PA, USA, 2012.
40. Calvert, G.; Ghadiri, M.; Tweedie, R. Aerodynamic dispersion of cohesive powders: A review of understanding and technology. *Adv. Powder Technol.* **2009**, *20*, 4–16. [[CrossRef](#)]

41. Suman, A.; Vulpio, A.; Fortini, A.; Fabbri, E.; Casari, N.; Merlin, M.; Pinelli, M. Experimental analysis of micro-sized particles time-wise adhesion: The influence of impact velocity and surface roughness. *Int. J. Heat Mass Transf.* **2021**, *165*, 120632. [[CrossRef](#)]
42. Lin, C.-M.; Chang, C.-M.; Chen, J.-H.; Wu, W. The effects of additive elements on the microstructure characteristics and mechanical properties of Cr-Fe-C hard-facing alloys. *J. Alloys Compd.* **2010**, *498*, 30–36. [[CrossRef](#)]
43. Raynor, G.V.; Rivlin, V.G. *Phase Equilibria in Iron Ternary Alloys: A Critical Assessment of the Experimental Literature*; CRC Press: Boca Raton, FL, USA, 1988; ISBN 978-0901462343.
44. Jilleh, A.; Kishore Babu, N.; Thota, V.; Anis, A.L.; Harun, M.K.; Talari, M.K. Microstructural and wear investigation of high chromium white cast iron hardfacing alloys deposited on carbon steel. *J. Alloys Compd.* **2021**, *857*, 157472. [[CrossRef](#)]
45. Berns, H.; Fischer, A. Microstructure of Fe-Cr-C hardfacing alloys with additions of Nb, Ti and, B. *Mater. Charact.* **1997**, *39*, 499–527. [[CrossRef](#)]
46. Wang, X.; Han, F.; Liu, X.; Qu, S.; Zou, Z. Microstructure and wear properties of the Fe-Ti-V-Mo-C hardfacing alloy. *Wear* **2008**, *265*, 583–589. [[CrossRef](#)]
47. Leško, A.; Navara, E. Microstructural characterization of high-carbon ferrochromium. *Mater. Charact.* **1996**, *36*, 349–356. [[CrossRef](#)]
48. Liu, S.; Zhou, Y.; Xing, X.; Wang, J.; Ren, X.; Yang, Q. Growth characteristics of primary M_7C_3 carbide in hypereutectic Fe-Cr-C alloy. *Sci. Rep.* **2016**, *6*, 32941. [[CrossRef](#)] [[PubMed](#)]
49. Guitar, M.A.; Scheid, A.; Suárez, S.; Britz, D.; Guigou, M.D.; Mücklich, F. Secondary carbides in high chromium cast irons: An alternative approach to their morphological and spatial distribution characterization. *Mater. Charact.* **2018**, *144*, 621–630. [[CrossRef](#)]
50. Doğan, Ö.N.; Hawk, J.A. Effect of carbide orientation on abrasion of high Cr white cast iron. *Wear* **1995**, *189*, 136–142. [[CrossRef](#)]
51. Chotěborský, R.; Hrabě, P.; Müller, M.; Válek, R.; Savková, J.; Jirka, M. Effect of carbide size in hardfacing on abrasive wear. *Res. Agric. Eng.* **2009**, *55*, 149–158. [[CrossRef](#)]
52. Lai, J.P.; Pan, Q.L.; Wang, Z.B.; Cui, H.R.; Wang, X.D.; Gao, Z.Z. Effects of destabilization temperature on the microstructure and mechanical properties of high chromium cast iron. *J. Mater. Eng. Perform.* **2017**, *26*, 4667–4675. [[CrossRef](#)]
53. Pawar, S.; Jha, A.K.; Mukhopadhyay, G. Effect of different carbides on the wear resistance of Fe-based hardfacing alloys. *Int. J. Refract. Met. Hard Mater.* **2019**, *78*, 288–295. [[CrossRef](#)]
54. Gucwa, M.; Winczek, J.; Parzych, S.; Kukuryk, M. The effect of the hardfacing processes parameters on the carbide volume fraction. In *Lecture Notes in Mechanical Engineering*; Springer: Lutsck, Ukraine, 2019; pp. 410–417. [[CrossRef](#)]

MDPI
St. Alban-Anlage 66
4052 Basel
Switzerland
Tel. +41 61 683 77 34
Fax +41 61 302 89 18
www.mdpi.com

Coatings Editorial Office
E-mail: coatings@mdpi.com
www.mdpi.com/journal/coatings



MDPI
St. Alban-Anlage 66
4052 Basel
Switzerland

Tel: +41 61 683 77 34
Fax: +41 61 302 89 18

www.mdpi.com



ISBN 978-3-0365-1803-9